Well Models for Mimetic Finite Difference Methods and Improved Representation of Wells in Multiscale Methods

by

Ingeborg Skjelkvåle Ligaarden

THESIS

for the degree of

MASTER OF SCIENCE

in

Computational Science and Engineering

Department of Mathematics
Faculty of Mathematics and Natural Sciences
University of Oslo

May 2008

Det matematisk- naturvitenskapelige fakultet
Universitetet i Oslo

Abstract

In reservoir simulation, the modeling and the representation of wells are critical factors. The standard approach for well modeling is to couple the well to the reservoir through the use of a well index, which relates the well pressure and flow rate to grid cell quantities. Well models for the recent mimetic finite difference methods (FDMs) are an unexplored field, but are necessary in order to use these methods for reservoir simulations.

In this thesis, we develop numerical well indices for mimetic FDMs by extending the well-known Peaceman radial-flow well model. The performance of the new well indices is tested on both homogeneous and heterogeneous 2D reservoir models with uniform Cartesian grids. The results are compared against a two-point flux approximation using Peaceman's well index and a reference solution obtained on a near-well radial grid. The tests show that it is critical to use specially adapted well indices for mimetic FDMs.

Furthermore, we consider improvements in the representation of wells in the also recently developed multiscale mixed finite element method (MsMFEM). This method uses a coarse partition of an underlying fine subgrid for simulations, while subscale heterogeneities and wells are incorporated through the use of locally defined basis functions. These basis functions are computed by solving a number of local flow problems on the fine grid by a subgrid solver. Mimetic FDMs have been shown to be particularly versatile as subgrid solvers.

In MsMFEM the wells are represented by well basis functions and the well model in the subgrid solver. The modeling of the flow near the wells is of great importance in order to produce an accurate global flow scenario. In this thesis, we show that the accuracy of MsMFEM can be improved by an overlap technique that extends the support of the well basis functions. Tests performed on both homogeneous and heterogeneous 2D reservoir models with uniform, square, coarse grids show that the most efficient way of representing a well in MsMFEM is to make a coarse grid partition that places the well in the center of the coarse well-block. In cases where this is not possible, the overlap technique is shown to be a successful remedy.

Acknowledgments

> Don't search for all the answers at once. A path is formed by laying one stone at a time.
>
> — *The Giant, Twin Peaks*

I have always liked mathematics. First because it was easy; later because it was challenging and beautiful; and after five years as a math student, because it turned out to be useful.

The latest discovery I partly owe to my excellent supervisors at the Department of Applied Mathematics in SINTEF ICT: Stein Krogstad and Knut-Andreas Lie, who have guided me trough the process of writing this thesis. I would like to use this opportunity to thank you both. *Stein Krogstad*: for always being available, for his ability to describe difficult subjects in an understandable way, and for his patience. *Knut-Andreas Lie*: for contributing with his experience and expertise within the field of reservoir simulation, and for all the red pens he has sacrificed to improve the readability of this thesis.

Working with this thesis has been a much more enjoyable experience thanks to all the nice people I have gotten to know at the Department of Applied Mathematics in SINTEF ICT. I would like to thank you all for including me in the group. In particular, my thanks goes to Sigurd Segtnan for valuable feedback on chapters of this thesis, and to Bård Skaflestad for help on mimetic and multiscale issues.

My friends and family have been very supportive throughout this entire process. I would like to express my gratitude to my brother *Olav*: for help, support, and inspiration; for breakfast and dinner company at SINTEF; and for reading drafts of this thesis. *Nicolaas*: for not breaking up with me, on the contrary being very supportive, even though I have spent more time with this thesis than with him during the past half year.

Last, but not least, *Mom and Dad*: for all your love and support. In more than one way would I not be here if it were not for you.

Ingeborg Skjelkvåle Ligaarden, May 2008

Contents

Part I

Introduction

Chapter 1

Introduction

In this thesis we are interested in improving the modeling and the representation of wells in reservoir simulation.

During the past decades there has been a growing demand for more accurate simulation of flow and transport in petroleum reservoirs. Even so, the industry is conservative and the two-point flux approximation (TPFA) method [7] is, and has been, the predominant method for reservoir simulation the last 30 years. TPFA is the preferred method in commercial simulators despite the fact that it has several known weaknesses. The main shortcoming of TPFA is lack of convergence on general grids with general permeability tensors. There exists, however, alternative methods that do converge in these cases. In this thesis, we focus on mimetic finite difference methods (FDMs) [9, 10], which are a new and promising class of numerical methods for flow in porous media. The mimetic FDMs are convergent on very general grids with general permeability tensors. Additionally, compared to other alternative methods, mimetic FDMs possess the advantageous property of easy implementation on general polyhedral grids. The polyhedral grid topology is very well suited to describe reservoirs, which makes the class of mimetic FDMs an attractive approach for reservoir simulation.

Accurate modeling of wells is critical in reservoir simulation. Well models are necessary because the numerically calculated pressure in a well-block deviates greatly from the pressure in the well. A well is seldom modeled explicitly, but instead through a well index, which relates the well pressure and flow rate to grid cell quantities. The first systematical study of well models was done by Peaceman [24] for TPFA. Due to the position of TPFA in reservoir simulation, the majority of later research on well models have been done for TPFA. Currently, there exists many well models for TPFA derived under different assumptions, but Peaceman's well model is still used in the majority of commercial simulators.

Now that mimetic FDMs are becoming mature for reservoir simulation, the need of well models for these methods is arising. In this thesis, we consider a numerical extension of Peaceman's well model for 2D single-phase flow to mimetic FDMs. In particular we develop well models for the lowest order Raviart-Thomas

(RT_0) mixed finite element method (FEM) and for a mimetic FDM. The RT_0-mixed FEM is chosen because it is equal to a mimetic method on Cartesian grids. Further, we perform tests of the new well models on both homogeneous and heterogeneous reservoir models. The heterogeneous permeability fields are from Dataset 2 from the 10th SPE Comparative Solution Project [14]. For simplicity, only Cartesian grids are considered. Finally, based on the results from the tests, we give guidelines for the use of the new well models.

The development of new methods in reservoir simulation is also driven by the development of technology that describes the geology of reservoirs. Todays detailed geomodels have opened new possibilities for accurate simulation of reservoirs. However, reservoir simulators have not been able to keep pace with the development within geomodeling, and the current situation is that geomodels describe the reservoir in more detail than what industry simulators are able to utilize. The standard approach for reservoir simulation with direct methods like TPFA cannot use detailed geomodels in an efficient way, nor are these methods designed to handle the additional challenges, such as high aspect ratios, faults, degenerate cells etc. that are posed by current high-end geomodels.

The traditional approach to overcome these challenges is upscaling techniques [13, 14], which reduces the level of detail in the geomodel by a type of averaging procedure in order to design a coarser grid model. These methods aim to capture the large scale flow behavior and much of the fine-scale details are lost in the process. In the later years, there has been increased focus on the impact of fine scale details on the large scale flow-pattern. Researchers have therefore been searching for a robust alternative to upscaling that can utilize the detailed geomodels in an accurate and efficient way. One of the results is the multiscale mixed finite element method (MsMFEM) [3, 4, 11, 20]. This method attempts to bridge the gap between the often conflicting demands of accuracy and efficiency in reservoir simulation, by the use of a fine subgrid that utilizes the detailed geomodel, and a coarse partition of the subgrid for efficient simulations. The effects of subscale heterogeneities and wells in MsMFEM are incorporated through the use of locally defined basis functions. These basis functions are computed by solving a number of local flow problems on the fine grid by a subgrid solver. In particular, the aforementioned mimetic FDMs have been shown to be versatile as subgrid solvers.

The two-grid approach enables MsMFEM to compute fine scale flow fields in fast and accurate simulations. The results for MsMFEM are so far very promising, see e.g. [4], but since MsMFEM is a relatively recent method, there are many possibilities for further improvements. Some of these possibilities represent challenges that must be overcome before MsMFEM can be used in industry simulators. One of the challenges is accurate representation of wells, which depends on the well basis functions and the accuracy of the well model in the subgrid solver.

In this thesis we present an improved approach for representing wells in MsMFEM that increases the accuracy of the simulations. The technique we use is called overlap because it extends the support of the well basis functions that control the flow from the wells. Moreover, we test the overlap technique on the same cases

as discussed above for the new well models. The focus of the tests done herein is on the accuracy of the method, and issues concerning computational time and memory use have not been emphasized.

1.1 Outline of the Thesis

This thesis is partitioned into *four* parts with a total of *nine* chapters. The outline of the thesis is as follows:

Part I: Introduction

Chapter 1 gives an introduction to the workings of the thesis.

Chapter 2 provides a short introduction to reservoir simulation and the governing equations for single-phase flow.

Part II: Well Models for Mimetic Finite Difference Methods

Chapter 3 presents the numerical methods used in Part II of the thesis. These methods include the two-point flux approximation method, the mixed finite element method, and the mimetic finite difference method. The chapter also provides information on how wells are implemented in the numerical methods.

Chapter 4 contains an introduction to wells and well modeling. The Peaceman well model is introduced and we discuss extensions and improvements.

Chapter 5 is where we extend Peaceman's well model to the lowest order Raviart-Thomas mixed FEM and mimetic FDMs.

Chapter 6 concerns testing of the new well models developed in Chapter 5. The chapter includes results from simulations on both homogeneous and heterogeneous reservoir models. We discuss the results from the tests and develop guidelines for the use of the new well models.

Part III: Improved Representation of Wells in the Multiscale Mixed Finite Element Method

Chapter 7 is an introduction to the multiscale mixed finite element method. The problems regarding the representation of wells in MsMFEM are discussed, and the overlap technique is introduced as a possible solution to these problems.

Chapter 8 presents results from simulations with the use of overlap in MsMFEM. The results are analyzed and we give recommendations for the use of overlap in MsMFEM.

Part IV: Conclusions and Further Work

Chapter 9 summarizes the conclusions made in the chapters of the thesis. We also point out interesting directions for further development and investigations.

Appendix A concerns the notation used in the thesis. Readers unfamiliar with standard notation are encouraged to review this appendix.

Chapter 2

Reservoir Modeling

This chapter gives an introduction to the theory behind reservoir simulation and the equations used. First, a presentation of reservoir properties is given, and subsequently the simplified equations for flow and transport in porous media are derived.

2.1 Reservoir Properties

A reservoir rock must be able to both contain and transmit a fluid, in other words the rock must have pores and the pores must be interconnected. The first property concerns the *porosity* of the rock, where the *total porosity* is defined as the percentage of pore volume or void space in the rock. In connection with reservoirs, isolated pores that cannot contribute to flow are not interesting. Therefore, we consider the *effective porosity*, that is the percentage of interconnected pore volume of the rock. We denote the effective porosity by ϕ, and will hereafter drop the term effective and refer to it as the porosity. If the rock is homogeneous, ϕ is a constant, while in the case of heterogeneous rock $\phi = \phi(\vec{x})$, where $\vec{x}$ is the position in the medium. Moreover, if the rock is compressible, ϕ will also depend on time, $\phi = \phi(\vec{x}, t)$, but in this thesis incompressible rock is assumed.

As mentioned, the reservoir rock must also be able to transmit the fluid. The rock's ability to transmit a fluid is called the *permeability*. Rocks with many and large well-connected pores are called *permeable*. Sandstones are examples of such rocks. On the other hand, rocks with few, smaller or less interconnected pores that are not able to transmit fluids are called *impermeable*. Such rocks include shales and siltstones. Furthermore, the permeability can be isotropic: the same in all directions, or anisotropic: vary with the direction of flow. Many reservoirs are made of sedimentary rocks with great variation in the vertical layers, and will thus have vertical to horizontal permeability anisotropy. In general, the permeability is described by a 3×3 tensor $\mathbf{K}$. An example of such a general permeability tensor

is

$$\mathbf{K} = \begin{pmatrix} K_{xx} & K_{xy} & K_{xz} \\ K_{yx} & K_{yy} & K_{yz} \\ K_{zx} & K_{zy} & K_{zz} \end{pmatrix}. \tag{2.1}$$

Onsager's principle [15] states that a pressure drop in the j-direction must give equal flow in the i-direction as a pressure drop in the i-direction would give in the j-direction. The elements K_{ij} and K_{ji} must therefore be equal. Thus, if $\mathbf{K}$ is represented as a matrix in an orthogonal coordinate system, $\mathbf{K}$ will be symmetric and positive definite. In the case of an isotropic reservoir, the permeability tensor can be simplified to $\mathbf{K} = k\mathbf{I}$, where k now describes the permeability in all directions. Another simplification can be made if the layers of the rock are parallel to the xy-plane. Given this property we may assume only vertical to horizontal permeability anisotropy. Thus, the permeability tensor simplifies to a diagonal tensor where $K_{xx} = K_{yy} = K_h$ describes the permeability in the horizontal direction, and $K_{zz} = K_v$ describes the permeability in the vertical direction. In addition, the permeability will typically vary with location in the formation, that is, $\mathbf{K} = \mathbf{K}(x, y, z)$. A formation with this property is said to be heterogeneous, while the opposite case, i.e. $\mathbf{K}$ is constant, is a homogeneous formation.

2.2 The Governing Equations for Single-Phase Flow

The governing equations for modeling the filtration of a single-phase fluid through a porous medium Ω are given by conservation of mass and Darcy's law.

Conservation of mass is ensured by the continuity equation,

$$\frac{\partial(\phi\rho)}{\partial t} + \nabla \cdot (\rho\vec{v}) = -q, \tag{2.2}$$

where ρ is the density of the fluid and $\vec{v}$ is the volumetric flow density. For simplicity, $\vec{v}$ will be referred to as the velocity throughout this thesis. The term q models sources and sinks, and the sign of q is chosen to be consistent with the later use of q as the well rate.

Darcy's law is an empirical law that relates the flow velocity to the pressure p. To formulate the law, we denote by z the depth and by g the gravity acceleration. Darcy's law states

$$\vec{v} = -\frac{\mathbf{K}}{\mu}(\nabla p + \rho g \nabla z). \tag{2.3}$$

Here, $\mathbf{K}$ is the permeability of the porous medium and μ is the viscosity of the fluid. In the following we assume stationary incompressible flow, meaning that ϕ and ρ are constants, so that $\frac{\partial(\phi\rho)}{\partial t} = 0$. Further, the fluid is assumed to be Newtonian, so μ is also constant. Lastly, if we look at horizontal flow in 2D, the gravitational term in (2.3) vanishes. Thus, under the assumptions stated above, the resulting system

of equations for $\vec{v}$ and p is

$$\nabla \cdot \vec{v} = f, \tag{2.4}$$

$$\vec{v} = -\frac{\mathbf{K}}{\mu}\nabla p, \tag{2.5}$$

where $f = \frac{-q}{\rho}$. This system is called the mixed formulation or the first order formulation. The model can also be formulated as one equation for the pressure by substituting (2.5) into (2.4),

$$-\nabla \cdot \left(\frac{\mathbf{K}}{\mu}\nabla p\right) = f. \tag{2.6}$$

Finally, to close the system, boundary conditions are needed. The two types of boundary conditions considered herein are:

flow (Neumann): $\vec{v} \cdot \vec{n}$ is specified at the boundaries.

pressure (Dirichlet): p is specified at the boundaries.

The Neumann no-flow boundary condition $\vec{v} \cdot \vec{n}|_{\partial\Omega} = 0$ is a very common boundary condition in reservoir simulation. No-flow boundary conditions are used to describe a reservoir as a closed system, where fluid cannot flow over the boundaries. In some cases, boundary conditions are given as a combination of Neumann and Dirichlet boundary conditions. We will discuss boundary conditions further in Chapters 3 and 5.

Part II

Well Models for Mimetic Finite Difference Methods

Chapter 3

Conservative Numerical Methods

In this chapter we introduce the numerical methods considered in Part II of the thesis. These methods include the two-point flux approximation method, the mixed finite element method, and the mimetic finite difference method. For motivational purposes, the two-point flux approximation method and the mixed finite element method will be presented first. The mimetic finite difference method will then be presented motivated from the derivation of the two-point flux approximation and the mixed finite element method.

3.1 Introduction

Partial differential equations (PDEs) can be used to describe a vast number of phenomena in nature. However, these PDEs are often hard or impossible to solve analytically, and thus a number of numerical solution techniques for PDEs have evolved. One of these methods is the finite element method (FEM), where a PDE is solved numerically by approximating the real solution in finite dimensional subspaces of the solution space. The main idea is to multiply the equations by test functions and then do partial integration. This results in what is called the *weak formulation* of the problem, which can be looked at as inner products over the approximation spaces. A more physical approach is the finite volume method (FVM), where the solution to a PDE is approximated by demanding that the integrated PDE holds over a control volume. Finite difference methods (FDMs), on the other hand, is a direct approach on the differential operators of the problem. The main idea in these methods is to approximate the continuous differential operators by discrete operators in order to compute a numerical solution. Simple finite difference approximations, such as forward difference

$$\frac{d}{dx}u(x_i) \approx \frac{u(x_{i+1}) - u(x_i)}{\Delta t}, \tag{3.1}$$

are well known. These simple FDMs are often intuitive, but numerical schemes based on these approximations are not flexible with respect to geometrically com-

plicated domains. However, in the later years there has been focus on developing new high quality FDMs. In these methods, the discrete operators preserve or "mime" certain critical properties of the original operators, and consequently they are called mimetic FDMs, [9, 10]. The preserved properties include conservation laws, solution symmetries, and the fundamental identities and theorems of vector and tensor calculus.

3.2 Preliminaries

We first present some mathematical machinery for deriving the numerical methods. Let $\Omega \subset \mathbb{R}^d$, $d \in \{2, 3\}$ be an open bounded set with Lipschitz continuous boundary $\partial\Omega$. In the derivations in this chapter we will use $d = 2$, but the results easily extend to $d = 3$. Assume that the outward unit normal $\vec{n}$ on Ω is defined at almost all boundary points as illustrated in Figure 3.1. Further, let $\Omega_h = \{E\}$ be a partition of the domain Ω into cells and let $\partial E = \cup_i^{k_E} e_i$ be the edges (faces in 3D) of a cell E. We denote by $\partial\Omega_h$ the collection of edges e in Ω. Moreover, let $|E|$ be the area (volume in 3D) of cell E, and let $|e|$ be the length (area in 3D) of e. Lastly, denote by $\vec{n}_e$ the unit outward normal on e. If the context is clear, the subscript of the unit outward normal is dropped.

For the presentation of the numerical methods, we simplify the system (2.4) and (2.5) and impose the Neumann no-flow boundary condition to obtain a prototype flow problem,

$$-\mathbf{K}\nabla p = \vec{v} \quad \text{in } \Omega, \tag{3.2}$$

$$\nabla \cdot \vec{v} = f \quad \text{in } \Omega, \tag{3.3}$$

$$\vec{v} \cdot \vec{n} = 0 \quad \text{on } \partial\Omega. \tag{3.4}$$

With this setup, the pressure is only determined up to a constant. The system can be closed by demanding that, e.g. $\int_\Omega p \, d\vec{x} = 0$, or $p(x_0) = p_0$.

A common assumption in reservoir simulation is that $\mathbf{K}$ is constant on each cell, and we will employ this assumption throughout the thesis. In addition, many numerical methods compute the flux over the edges instead of the velocity. Therefore, define by

$$F_e = \int_e \vec{v} \cdot \vec{n}_e \, ds \tag{3.5}$$

the *flux* over edge e.

Sobolev spaces

Sobolev spaces are fundamental in PDE theory, and we therefore give a short introduction to the concept here. For a more comprehensive introduction, the reader is referred to [16, Chapter 5]. The connection between Sobolev spaces and PDEs is that the solutions of PDEs naturally lie in Sobolev spaces. The theory of Sobolev

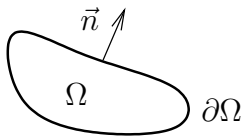

Figure 3.1: The domain Ω.

spaces is built on the introduction of weak derivatives, which extends the solution space to include solutions that are not in the classical spaces of continuous functions. Many of these solutions are interesting for applications, as we shall see in the following. For the solution of the system (3.2)–(3.4) we define the following Sobolev spaces:

$$H^{div}(E) = \{\vec{v} \in L^2(E)^d : \nabla \cdot \vec{v} \in L^2(E)\}, \tag{3.6}$$

$$H_0^{div}(\Omega_h) = \{\vec{v} \in H^{div}(\cup_{E\in\Omega_h} E) : \vec{v} \cdot \vec{n} = 0 \text{ on } \partial\Omega\}, \tag{3.7}$$

$$H_0^{div}(\Omega) = \{\vec{v} \in H^{div}(\Omega) : \vec{v} \cdot \vec{n} = 0 \text{ on } \partial\Omega\}. \tag{3.8}$$

3.3 The Two-Point Flux Approximation Method

We start by presenting the two-point flux approximation (TPFA). The TPFA is a finite volume method that can be used to solve the system (3.2)–(3.4).

3.3.1 Derivation of the TPFA

The main idea in the TPFA method is to approximate the flux over an edge by the difference of the cell centered pressures in the neighboring cells sharing the edge. The finite volume method is a physically motivated approach with the requirement that the integrated conservation law, in this case the integral of (3.3), holds over a control volume CV. This requirement ensures that mass is conserved in an average sense. We let the control volume be denoted by CV and its surface by SV. The finite volume requirement gives

$$\int_{CV} \nabla \cdot \vec{v}\, d\vec{x} = \int_{CV} f\, d\vec{x}. \tag{3.9}$$

Applying the divergence theorem results in

$$\int_{SV} \vec{v} \cdot \vec{n}\, ds = \int_{CV} f\, d\vec{x}. \tag{3.10}$$

Next, let each cell $E \in \Omega_h$ act as a control volume. Replacing CV by E and SV by ∂E gives

$$\int_{\partial E} \vec{v} \cdot \vec{n}\, ds = \sum_{l=1}^{k_E} \int_{e_l} \vec{v} \cdot \vec{n}\, ds = \int_E f\, d\vec{x}, \quad \forall E \in \Omega_h. \tag{3.11}$$

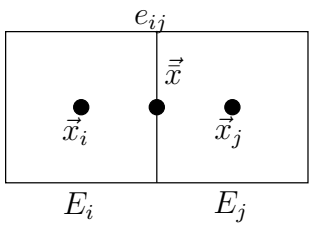

Figure 3.2: TPFA setup.

Using the definition of flux in (3.2) we get

$$\sum_{l=1}^{k_E} F_{e_l} = \int_E f \, d\vec{x}, \quad \forall E \in \Omega_h. \tag{3.12}$$

Observe that $F_{e_l} = 0$ for all boundary edges due to the boundary condition (3.4). Hence, the boundary condition is naturally incorporated by summing over only non-boundary edges. Further, we will assume that f is constant on each cell or a point source, so $f_i := \int_{E_i} f \, d\vec{x}$ can easily be computed. By substituting (3.2) for $\vec{v}$ in the definition of the flux over an edge, we get an equation including the pressure,

$$F_e = -\int_e \mathbf{K} \nabla p \cdot \vec{n} \, ds. \tag{3.13}$$

This equation can be used to express the flux in terms of a pressure difference. To derive an expression for the flux, we look at a cell E_i with neighbor E_j, sharing the edge e_{ij} as shown in Figure 3.2. Let $\vec{x}_i$ and $\vec{x}_j$ be the cell centers (centroids) and let p_i and p_j be the values of the pressure at the cell centers. Further, let $\vec{\bar{x}}$ be the midpoint on e_{ij} and $\vec{n}$ be the unit normal from E_i to E_j. Assume now that $\mathbf{K}$ is constant on each cell and that the cell edge e_{ij} is a straight line. We denote by $\mathbf{K}_i$ and $\mathbf{K}_j$ the value of $\mathbf{K}$ on the cells E_i and E_j. Observe that the integrand in (3.13) is the gradient of p in the direction of $\mathbf{K}\vec{n}$. Thus, if $\mathbf{K}\vec{n}$ is parallel to the path from $\vec{x}_i$ to $\vec{x}_j$ through $\vec{\bar{x}}$, we can make a linear approximation to p and replace ∇p by a pressure difference between the pressures at the cell center and at $\vec{\bar{x}}$. Since this can be done for both E_i and E_j, we get

$$p_i - p(\vec{\bar{x}}) = \frac{F_{e_{ij}}}{|e_{ij}|} \frac{\|\vec{x}_i - \vec{\bar{x}}\|}{\|\mathbf{K}_i \vec{n}\|}, \tag{3.14}$$

$$p(\vec{\bar{x}}) - p_j = \frac{F_{e_{ij}}}{|e_{ij}|} \frac{\|\vec{x}_j - \vec{\bar{x}}\|}{\|\mathbf{K}_j \vec{n}\|}. \tag{3.15}$$

Now, $F_{e_{ij}}$ must be equal in (3.14) and (3.15) to obtain continuity in the flux over an edge. Thus, we can add the equations with the result that $p(\vec{\bar{x}})$ is eliminated, and obtain

$$p_i - p_j = \frac{F_{e_{ij}}}{|e_{ij}|} \left(\frac{\|\vec{x}_i - \vec{\bar{x}}\|}{\|\mathbf{K}_i \vec{n}\|} + \frac{\|\vec{x}_j - \vec{\bar{x}}\|}{\|\mathbf{K}_j \vec{n}\|} \right). \tag{3.16}$$

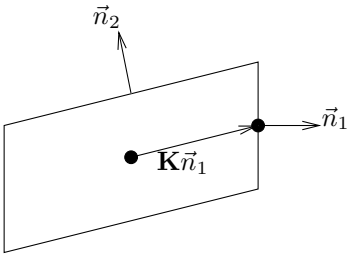

Figure 3.3: Parallelogram cell with normal vectors.

The term two-point flux approximation stems from the approximation of the flux over an edge by the use of the pressure in two points. Equation (3.16) is usually written as

$$F_{e_{ij}} = t_{e_{ij}}(p_i - p_j), \tag{3.17}$$

where

$$t_{e_{ij}} = |e_{ij}| \left(\frac{\|\vec{x}_i - \vec{\bar{x}}\|}{\|\mathbf{K}_i \vec{n}\|} + \frac{\|\vec{x}_j - \vec{\bar{x}}\|}{\|\mathbf{K}_j \vec{n}\|} \right)^{-1}, \tag{3.18}$$

is the *transmissibility* over e_{ij}. Finally, the finite volume requirement was that (3.12) was fulfilled. Hence we must sum (3.17) over all non-boundary edges $e_{ij} \in \partial E_i$ corresponding to neighboring cells E_j,

$$\sum_j t_{e_{ij}}(p_i - p_j) = \int_{E_i} f \, d\vec{x}. \tag{3.19}$$

Given a global numbering of the cells, we get a linear system for the pressure, $\mathbf{Ap} = \mathbf{b}$ given by $\mathbf{A} = [a_{ik}]$ where

$$a_{ik} = \begin{cases} \sum_j t_{ij} & \text{if } i = j, \\ -t_{ik} & \text{if } i \neq k, \end{cases} \qquad b_i = \int_{E_i} f d\vec{x} = f_i.$$

This system is symmetric, but the solution is only determined up to an arbitrary constant and is hence not unique. By forcing e.g. $p_1 = 0$, see Section 3.2, uniqueness is obtained and the system also becomes positive definite.

3.3.2 Properties of TPFA

The first-order approximation done in (3.16) is only valid if the points $\vec{x}_i, \vec{\bar{x}}$, and $\vec{x}_j$ are connected by lines parallel to $\mathbf{K}\vec{n}$. A grid satisfying this requirement is said to be $\mathbf{K}$-orthogonal.

We will give some examples of grids satisfying this requirement. As before, assume that $\mathbf{K}$ is constant on each cell. An orthogonal grid will be $\mathbf{K}$-orthogonal if the directions in $\mathbf{K}$ are parallel to the grid lines. For an orthogonal grid with grid lines aligned with the coordinate axes, this requirement means that the permeability

tensor must be diagonal. Using the TPFA method on such a grid when $\mathbf{K}$ is a full permeability tensor corresponds to neglecting the off-diagonal elements in $\mathbf{K}$. A grid with parallelogram cells, as shown in Figure 3.3, is $\mathbf{K}$-orthogonal if the following requirement is satisfied for all cells:

$$\vec{n}_2 \cdot \mathbf{K}\vec{n}_1 = 0. \tag{3.20}$$

This requirement ensures that $\mathbf{K}\vec{n}_i$ mets edge e_i in the midpoint $\vec{\bar{x}}$ for all i, and hence the approximation done in (3.16) is valid.

If the TPFA method is used on a non-$\mathbf{K}$-orthogonal grid, the approximation will not converge to the correct solution. Unfortunately, many grids in reservoir simulations are not $\mathbf{K}$-orthogonal. In spite of this major shortcoming, the TPFA is still the predominant method in industry simulators because of its simplicity and speed. We mention that the multi-point flux approximation (MPFA) is a generalization of TPFA that is constructed to amend the shortcomings of TPFA on non-$\mathbf{K}$-orthogonal grids. For further reading on MPFA, the reader is referred to [5].

3.4 The Mixed Finite Element Method

Another approach for solving numerically (3.2)–(3.4) is the mixed finite element method (FEM). The term mixed stems from the fact that we solve for $(\vec{v}, p)$ simultaneously and approximate $\vec{v}$ and p in different spaces. This solution strategy is different from the approach in Section 3.3 and in standard finite element methods, where the flux is computed from the pressure.

3.4.1 Derivation of the mixed FEMs

The formulation of the system in (3.2)–(3.4) is called the strong formulation and is strict in the demands of continuity of the solution. In the mixed FEMs we instead look at the *weak formulation* of the system. This formulation is motivated as follows: let $\vec{u} \in C_0^\infty(\Omega)^2$ be a test function. Observe that $\vec{u}$ satisfies the boundary condition on $\vec{v}$, $\vec{u}|_{\partial\Omega} = \vec{v}|_{\partial\Omega}$. We multiply (3.2) by $\vec{u}$ and integrate over Ω to obtain

$$\int_\Omega (\vec{u} \cdot \mathbf{K}^{-1}\vec{v} + \nabla p \cdot \vec{u})\, d\vec{x} = 0. \tag{3.21}$$

The next step is to use Green's theorem to do partial integration. This results in

$$\int_\Omega (\vec{u} \cdot \mathbf{K}^{-1}\vec{v} - p\nabla \cdot \vec{u})\, d\vec{x} = 0, \tag{3.22}$$

where the boundary term has vanished due to the compact support of the test function. The same procedure can be applied to (3.3) for a test function $q \in C_0^\infty(\Omega)$, resulting in

$$\int_\Omega q(\nabla \cdot \vec{v} - f)\, d\vec{x} = 0. \tag{3.23}$$

Now, we make some observations. First, since the test functions were arbitrary, (3.22) and (3.23) must hold for all $\vec{u} \in C_0^\infty(\Omega)^2$ and $q \in C_0^\infty(\Omega)$, respectively. Second, if (3.22) and (3.23) should be valid, we must demand $\vec{v} \in L^2(\Omega)^2$ with $\nabla \cdot \vec{v} \in L^2(\Omega)$ and that $p \in L^2(\Omega)$. Therefore, the right solution space for $(\vec{v}, p)$ is $H_0^{div}(\Omega) \times L^2(\Omega)$. And third, the demand that the test functions should be smooth is too strict. In fact, the test functions should be chosen from the solution space, meaning that $(\vec{u}, q) \in H_0^{div}(\Omega) \times L^2(\Omega)$. The resulting weak formulation of the problem in (3.2)–(3.4) is: find $(\vec{v}, p) \in H_0^{div}(\Omega) \times L^2(\Omega)$ so that

$$\int_\Omega (\vec{u} \cdot \mathbf{K}^{-1}\vec{v} - p\nabla \cdot \vec{u})\, d\vec{x} = 0, \quad \forall \vec{u} \in H_0^{div}(\Omega), \tag{3.24}$$

$$\int_\Omega q(\nabla \cdot \vec{v} - f)\, d\vec{x} = 0, \quad \forall q \in L^2(\Omega). \tag{3.25}$$

Given a partition Ω_h of Ω we develop a discretization of (3.24) and (3.25). Following the notation in [4], we define the bilinear forms

$$a(\cdot,\cdot) : H_0^{div}(\Omega_h) \times H_0^{div}(\Omega_h) \to \mathbb{R},$$

$$a(\vec{u}, \vec{v}) = \sum_{E \in \Omega_h} \int_E \vec{u} \cdot \mathbf{K}^{-1}\vec{v}\, d\vec{x}, \tag{3.26}$$

$$b(\cdot,\cdot) : H_0^{div}(\Omega_h) \times L^2(\Omega) \to \mathbb{R},$$

$$b(\vec{v}, p) = \sum_{E \in \Omega_h} \int_E p\nabla \cdot \vec{v}\, d\vec{x}, \tag{3.27}$$

$$(\cdot,\cdot) : L^2(\Omega) \times L^2(\Omega) \to \mathbb{R},$$

$$(p, q) = \int_\Omega pq\, d\vec{x}. \tag{3.28}$$

Solving the system (3.24) and (3.25) is now equivalent to finding $(\vec{v}, p) \in H_0^{div}(\Omega) \times L^2(\Omega)$ satisfying

$$\begin{aligned} a(\vec{u}, \vec{v}) - b(\vec{u}, p) &= 0, && \forall \vec{u} \in H_0^{div}(\Omega), \\ b(\vec{v}, q) &= (f, q), && \forall q \in L^2(\Omega). \end{aligned} \tag{3.29}$$

However, in practice we cannot find $(\vec{v}, p) \in H_0^{div}(\Omega) \times L^2(\Omega)$ since these are infinite dimensional spaces. Therefore, the solution to the system (3.29) must be approximated using finite dimensional subspaces $\mathbf{V} \subset H_0^{div}(\Omega)$ and $Q \subset L^2(\Omega)$. In this setting, the problem of solving system (3.29) is reformulated as: find $(\vec{v}_h, p_h) \in \mathbf{V} \times Q$ so that

$$\begin{aligned} a(\vec{u}_h, \vec{v}_h) - b(\vec{u}_h, p_h) &= 0, && \forall \vec{u}_h \in \mathbf{V}, \\ b(\vec{v}_h, q_h) &= (f, q_h), && \forall q_h \in Q. \end{aligned} \tag{3.30}$$

An example of subspaces $\mathbf{V}$ and Q, which will be frequently used in this thesis, is given below.

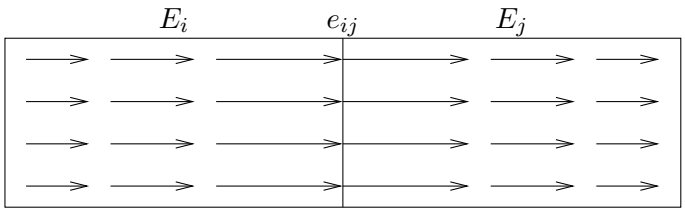

Figure 3.4: Basis function in $\mathbf{V}$ for an edge e_{ij}.

The lowest order Raviart-Thomas elements

We now present a classical pair of approximation subspaces $\mathbf{V}$, Q called the lowest order Raviart-Thomas elements, (RT_0) [27]. Following Aavatsmark [5], the presentation of RT_0 is done for triangular and parallelogram cells. Define the subspaces $\mathbf{V}, Q$ by

$$\begin{aligned}\mathbf{V} := \{\vec{u} \in L^\infty(\Omega)^2 : &\vec{u}|_E \text{ is linear } \forall E \in \Omega_h, \\ &\vec{u}\cdot\vec{n}_E|_e \text{ is constant on } e \in \partial E, \\ &\text{and } \vec{u}\cdot\vec{n}_E \text{ is continuous on } \Omega\}\end{aligned} \tag{3.31}$$

$$Q := \{q \in L^\infty(\Omega) : \ q|_E \text{ is constant } \ \forall E \in \Omega\} \tag{3.32}$$

In 1D, $\mathbf{V}$ consists of the hat-functions that are common in finite element discretizations. A visualization of a velocity basis function in 2D is shown in Figure 3.4.

3.4.2 Formulation of the linear system

Let $\mathbf{V}, Q$ be the function space for the solution $(\vec{v}_h, p_h)$ of (3.30). We choose the basis functions $\vec{\psi}_e \in \mathbf{V}$ and $\phi_E \in Q$ so that $\vec{\psi}_e$ has support on the cells sharing the edge e and $\phi_E \in Q$ has support on E. Thus, the basis functions are nearly orthogonal, which means that we can recover the values of $\vec{v}$ on each edge and the values of p in each cell by defining

$$\begin{aligned}\vec{v}_h &= \sum_{e\in\partial\Omega_h} v_e\vec{\psi}_e, \quad \vec{\psi}_e \in \mathbf{V}, \\ p_h &= \sum_{E\in\Omega_h} p_E\phi_E, \quad \phi_E \in Q.\end{aligned} \tag{3.33}$$

Assume that the cells and edges are numbered globally, with l the number of edges and m the number of cells in Ω_h. The system (3.30) can now be written as a linear system in the unknowns $\mathbf{v} = (v_1, v_2, \ldots, v_l)^T$ and $\mathbf{p} = (p_1, p_2, \ldots, p_m)^T$,

$$\begin{pmatrix}\mathbf{A} & \mathbf{B}^T \\ \mathbf{B} & \mathbf{0}\end{pmatrix}\begin{pmatrix}\mathbf{v} \\ -\mathbf{p}\end{pmatrix} = \begin{pmatrix}\mathbf{0} \\ \mathbf{f}\end{pmatrix}, \tag{3.34}$$

where $A_{ij} = \int_{E_i\cup E_j} \vec{\psi}_i^T\mathbf{K}^{-1}\vec{\psi}_j \, d\vec{x}$. Unfortunately, this system will be indefinite, which is unwanted from a computational point of view because it is harder to solve

than a positive definite system. The indefinite property can easily be seen if we recognize the solution of (3.29) as a saddle point of the Lagrange functional

$$L(\vec{v}, p) = \frac{1}{2}a(\vec{v}, \vec{v}) - b(\vec{v}, p) + (p, f). \tag{3.35}$$

A saddle point is recognized by

$$L(\vec{v}, q) \leq L(\vec{v}, p) \leq L(\vec{u}, p), \quad \forall (\vec{u}, q) \in \mathbf{V} \times Q. \tag{3.36}$$

The linear system arising from a saddle point problem, such as (3.34), will have both positive and negative eigenvalues and hence be indefinite. The reader is referred to [8, page 17] for the derivation of the system (3.2) and (3.3) as a saddle point of (3.35). In the next section we present a solution to the problem of indefiniteness: a hybrid mixed discretization that leads to a positive definite system.

3.4.3 Hybrid mixed FEM

We want the linear system for the discrete solution to be positive definite because this simplifies the solution process. A positive definite system can be obtained by a hybrid mixed FEM discretization [8], where the pressure on the edges is introduced as an extra variable. To do this, we define the bilinear form on Ω_h

$$\begin{aligned} c(\cdot,\cdot) : H_0^{div}(\Omega_h) \times H^{\frac{1}{2}}(\partial\Omega_h) &\to \mathbb{R}, \\ c(\vec{v}, \lambda) &= \sum_{E \in \Omega_h} \int_{\partial E} \lambda \vec{v} \cdot \vec{n}_E \, ds. \end{aligned} \tag{3.37}$$

Here, λ corresponds to the pressure at the cell edges and $H^{\frac{1}{2}}(\partial\Omega_h)$ is spanned by the traces on $\partial\Omega_h$ in $H^1(\Omega_h)$. A trace is the Sobolev space equivalent of a boundary, see [16] for more information on traces. The hybrid formulation of (3.2)–(3.4) is

$$a(\vec{u}, \vec{v}) - b(\vec{u}, p) + c(\vec{u}, \lambda) = 0, \qquad \forall \vec{u} \in H_0^{div}(\Omega_h), \tag{3.38}$$

$$b(\vec{v}, q) = (f, q), \qquad \forall q \in L^2(\Omega), \tag{3.39}$$

$$c(\vec{v}, \pi) = 0, \qquad \forall \pi \in H^{\frac{1}{2}}(\partial\Omega_h \backslash \partial\Omega). \tag{3.40}$$

This is discretized by seeking $(\vec{v}_h, p_h, \lambda_h) \in \tilde{\mathbf{V}} \times Q \times \Pi$, where $\tilde{\mathbf{V}} \subset H_0^{div}(\Omega_h)$, $Q \subset L^2(\Omega)$, and $\Pi \subset H^{\frac{1}{2}}(\partial\Omega_h)$. The definition of p_h in unchanged, while $\vec{v}_h$ and λ_h are defined as

$$\begin{aligned} \vec{v}_h &= \sum_{e \in \partial E, E \in \Omega_h} v_e \vec{\psi}_e, \quad \vec{\psi}_e \in \tilde{\mathbf{V}}, \\ \lambda_h &= \sum_{e \in \partial\Omega_h} \lambda_e \gamma_e, \quad \gamma_e \in \Pi. \end{aligned} \tag{3.41}$$

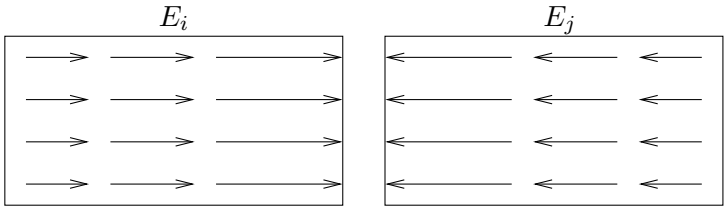

Figure 3.5: Basis functions in $\tilde{\mathbf{V}}$ for an edge e_{ij}.

Observe that we have departed from the constraint that $\tilde{\mathbf{V}} \subset H^{div}(\Omega)$ by introducing $c(\cdot, \cdot)$ in (3.38), but that continuity in the velocity component is reintroduced by (3.40). Therefore, $(\vec{v}_h, p_h, \lambda_h)$ is still a solution to (3.2)–(3.4). A proof of this property and further details on hybrid discretization are found in [8, pages 177–183]. The number of basis functions in $\tilde{\mathbf{V}}$ is equal to the number of cell-wise numbered edges in Ω_h, which means that all internal edges in the domain have two velocity basis functions. This is illustrated in Figure 3.5 for the RT_0-basis.

Let now $\mathbf{v} = (v_1, v_2, \ldots, v_n)^T$, where n is the number of cell-wise numbered edges in Ω_h. Further, let $\boldsymbol{\lambda} = (\lambda_1, \lambda_2, \ldots, \lambda_l)^T$, where l is the number of edges in Ω_h. The hybrid linear system arising from (3.38)–(3.40) is

$$\begin{pmatrix} \mathbf{A} & \mathbf{B}^T & \mathbf{C}^T \\ \mathbf{B} & \mathbf{0} & \mathbf{0} \\ \mathbf{C} & \mathbf{0} & \mathbf{0} \end{pmatrix} \begin{pmatrix} \mathbf{v} \\ -\mathbf{p} \\ \boldsymbol{\lambda} \end{pmatrix} = \begin{pmatrix} \mathbf{0} \\ \mathbf{f} \\ \mathbf{0} \end{pmatrix}. \tag{3.42}$$

Note that $\mathbf{A}$ is block diagonal when the basis functions are numbered cell-wise. We can therefore eliminate $\mathbf{v}$ at cell level by a Schur-complement reduction with respect to $\mathbf{A}$ to obtain a positive definite system for $(\mathbf{p}, \boldsymbol{\lambda})$,

$$\begin{pmatrix} \mathbf{D} & -\mathbf{F}^T \\ \mathbf{F} & -\mathbf{C}\mathbf{A}^{-1}\mathbf{C}^T \end{pmatrix} \begin{pmatrix} \mathbf{p} \\ \boldsymbol{\lambda} \end{pmatrix} = \begin{pmatrix} \mathbf{f} \\ \mathbf{0} \end{pmatrix}. \tag{3.43}$$

Here, $\mathbf{D} = \mathbf{B}\mathbf{A}^{-1}\mathbf{B}^T$ and $\mathbf{F} = \mathbf{C}\mathbf{A}^{-1}\mathbf{B}^T$. The basis functions $\phi_E \in Q$ are usually chosen as piecewise constants, as we saw for RT_0. Therefore we can choose

$$\phi_E(\vec{x}) = \begin{cases} 1 & \text{if } \vec{x} \in E \\ 0 & \text{otherwise}, \end{cases} \tag{3.44}$$

meaning that $\mathbf{D}$ will be a diagonal matrix. We can then again perform an elimination at cell level, this time eliminating $\mathbf{p}$ to obtain the following positive definite system for $\boldsymbol{\lambda}$

$$\mathbf{H}\boldsymbol{\lambda} = \mathbf{b}. \tag{3.45}$$

Here, $\mathbf{H} = \mathbf{C}\mathbf{A}^{-1}\mathbf{C}^T - \mathbf{F}\mathbf{D}^{-1}\mathbf{F}^T$ and $\mathbf{b} = \mathbf{F}\mathbf{D}^{-1}\mathbf{f}$. This system is solved for $\boldsymbol{\lambda}$, and then $\mathbf{p}$ and $\mathbf{v}$ are computed by solving a diagonal and a block-diagonal system, respectively.

3.4.4 Properties of the mixed FEM

The major drawback of mixed FEM is difficult implementation on general polygonal and polyhedral grids. This includes the important case of corner-point grids [26], which is an industry standard in reservoir simulation. A corner-point grid consists of a set of hexahedral cells that are aligned in a logical Cartesian fashion. The cells are shaped according to the geology of the reservoir, which makes this approach very suitable for describing the geological structures in a reservoir. However, the flexibility of corner-point grid can results in deformed and degenerated hexahedral cells. If mixed FEM is to be implemented for such general cells, mappings to reference elements would be required to enable assembly of the linear system. This means that we would need a reference element for each possible cell geometry, which would be impractical and in some cases not possible to achieve.

3.5 The Mimetic Finite Difference Method

One method that has been developed quite recently is the mimetic finite difference method (FDM) [9]. The mimetic FDM can be seen as the finite difference counterpart to mixed FEM. This method has many qualities superior to the mixed FEM and TPFA, but it is not yet widely used. Two of the strengths of the mimetic FDM are easy implementation on general polyhedral grids and good convergence properties [9]. Tetrahedral grids have long been dominant in engineering simulations, and methods such as the mixed FEM are well suited for these types of grids. However, in reservoir simulation, polyhedral grids are more interesting. An already mentioned example is the important case of corner-point grid that makes it possible to model complex geological features of the reservoir.

3.5.1 Motivation

In the following we introduce the mimetic FDM motivated by the TPFA method presented in Section 3.3. To simplify the notation we look at one grid cell E, as displayed in Figure 3.6, and hence no subscript is needed to specify the cell. Let F_e be the flux over edge e as defined in (3.2), so that the vector of fluxes for E is

$$\mathbf{F} = (F_1, F_2, \ldots, F_{k_E})^T. \tag{3.46}$$

Accordingly, the pressure related to the edges of the cell is denoted by

$$\boldsymbol{\lambda} = (\lambda_1, \lambda_2, \ldots, \lambda_{k_E})^T. \tag{3.47}$$

Further, let p_E be the pressure in the center of the cell.

The main idea is to express the flux $\mathbf{F}$ by a transmissibility factor $\mathbf{T}$ and the difference between the pressure in the center of the cell and the pressure at the edges of the cell,

$$\mathbf{F} = -\mathbf{T}(\boldsymbol{\lambda} - p_E). \tag{3.48}$$

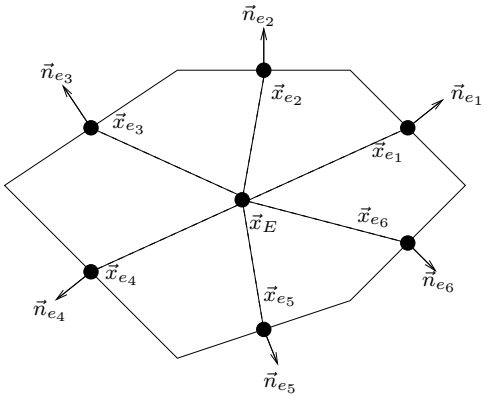

Figure 3.6: Example of a grid cell E with center x_E and $k_E = 6$.

Notice that if $\mathbf{T}$ is a diagonal tensor, we can eliminate the pressure at the edges of the cell to obtain a TPFA as in Section 3.3.

In the following we derive an expression for $\mathbf{T}$. As in the derivation of the TPFA we begin with the assumption that the pressure is linear in each cell. Thus, the pressure in a cell is given by

$$p(\vec{x}) = \mathbf{a} \cdot \vec{x} + c \quad \text{for } \mathbf{a} \in \mathbb{R}^2, c \in \mathbb{R}. \tag{3.49}$$

This is equivalent to demanding that the method is exact for a linear pressure field. From the mixed formulation of the PDE, (3.2)–(3.4), we have the relation between the velocity and the pressure,

$$\vec{v} = -\mathbf{K}\nabla p. \tag{3.50}$$

We insert the gradient of the pressure obtained from (3.49) and get

$$\vec{v} = -\mathbf{K}\mathbf{a}. \tag{3.51}$$

Consider now all faces of E, and define for $i = 1, \ldots, k_e$: $\mathbf{N}(i,:) = |e_i|\vec{n}_{e_i}^T$ and $\mathbf{C}_T(i,:) = (\vec{x}_{e_i} - \vec{x}_E)^T$. If we now assume that $\mathbf{K}$ is constant on each edge e, the resulting expression for the flux over e is given by

$$F_e = -\int_e \mathbf{K}\mathbf{a} \cdot \vec{n}_e \, ds = -|e|\mathbf{K}\mathbf{a} \cdot \vec{n}_e. \tag{3.52}$$

Since this holds for all edges e, we obtain an expression for the vector of fluxes

$$\mathbf{F} = -\mathbf{N}\mathbf{K}\mathbf{a}. \tag{3.53}$$

Furthermore, we can reformulate (3.48) by observing that the difference between the pressure at the midpoint of an edge e and the center can be written as

$$\lambda_e - p_E = (\vec{x}_e - \vec{x}_E) \cdot \mathbf{a}. \tag{3.54}$$

When (3.54) is inserted in (3.48), we get

$$\mathbf{F} = -\mathbf{T}(\boldsymbol{\lambda} - p_E) = -\mathbf{T}\mathbf{C}_T \cdot \mathbf{a}. \tag{3.55}$$

Since (3.53) and (3.55) must be equal, we get a requirement on $\mathbf{T}$ given by

$$\mathbf{T}\mathbf{C}_T = \mathbf{N}\mathbf{K}. \tag{3.56}$$

Note that $\mathbf{T} = \mathbf{T}_E$ depends on the cell, but that the subscript was dropped as we only looked at one cell. From now on we use the subscript to avoid confusion when considering all $E \in \Omega_h$. Many different matrices $\mathbf{T}_E$ fulfill requirement (3.56), but before we go into detail on how $\mathbf{T}_E$ should be constructed, we give an introduction to the theoretical basis of mimetic FDMs. In the next section we show that $\mathbf{T}_E$ is related to the inverse of an inner product matrix $\mathbf{M}_E$. Readers that are interested in the practical approach can skip directly to Section 3.5.3 where we give criteria for constructing a valid $\mathbf{T}_E$.

3.5.2 The theoretical basis of mimetic FDMs

The motivation for mimetic FDMs in the previous section does not explain how the expression for the flux in (3.48) is obtained, meaning the theoretical foundation of the method. We now give a short presentation of the theory behind mimetic FDMs. This theoretical basis is taken from [10], but will be adapted for the use of flux as an unknown instead of velocity.

Let Ω_h be a a non-overlapping conformal partition of Ω into simply-connected polygonal (polyhedral in 3D) cells with flat edges (faces in 3D). The main idea is to make discrete versions of the operators div and ∇ (grad). We use the notation $\mathrm{div}\,\vec{v} = \nabla \cdot \vec{v}$. The model problem

$$\mathrm{div}\,\vec{v} = f, \tag{3.57}$$

$$\vec{v} = -\mathbf{K}\nabla p, \tag{3.58}$$

is in mimetic FDMs formulated as the discrete problem

$$\mathcal{DIV}_h\,\mathbf{v}_h = \mathbf{f}_m, \tag{3.59}$$

$$\mathbf{v}_h = \mathcal{G}_h\,\mathbf{p}_h, \tag{3.60}$$

where $\mathcal{DIV}_h$ and $\mathcal{G}_h$ are discrete versions of div and $-\mathbf{K}\nabla$ $(\mathbf{K}\mathrm{grad})$, and $\mathbf{f}_m$ is the vector of mean values of the source function f. To define these operators, we must first define the solution spaces and inner products over these spaces.

We start with considering the velocity $\vec{v}$ and the pressure p as unknowns following [10], and we adapt the theory for flux subsequently. Let Q_h be the space of discrete pressures that are constant on each cell E. Denote by q_E the value of $\mathbf{q} \in Q_h$ on cell E. Let X_h be the space of discrete velocities that associates each edge e in a cell E to a a velocity v_e^E. We use the notation v_e to mean the velocity over a specified edge e, while v_e^E is the velocity over $e \in \partial E$, and lastly $\mathbf{v}_E = (v_{e_1}, v_{e_2}, \ldots, v_{e_{k_E}})$ is the vector of velocities in cell E.

Inner products

The foundation of the mimetic FDM is the formulation of discrete inner products over the approximation spaces Q_h and X_h. These inner products are defined below.

Definition 3.1. *The inner product in Q_h is defined to be*

$$[\mathbf{p}, \mathbf{q}]_{Q_h} = \sum_{E \in \Omega_h} p_E q_E |E|. \tag{3.61}$$

Definition 3.2. *The inner product in X_h is defined to be*

$$[\mathbf{v}, \mathbf{u}]_{X_h} = \sum_{E \in \Omega_h} [\mathbf{v}, \mathbf{u}]_E, \tag{3.62}$$

where $[\mathbf{v}, \mathbf{u}]_E$ is an inner product on cell E.

The inner product $[\mathbf{v}, \mathbf{u}]_E$ can be written as

$$[\mathbf{v}, \mathbf{u}]_E = \mathbf{u}_E^T \mathbf{M}_E \mathbf{v}_E, \tag{3.63}$$

where $\mathbf{M}_E$ is a symmetric and positive definite $k_E \times k_E$ matrix. Note that only the velocities over the edges are used to calculate the inner product. Because many different matrices can satisfy the requirements made on $\mathbf{M}_E$, the inner product in (3.62) is not unique. I order to get a convergent method, $\mathbf{M}_E$ must have some properties that will be discussed in Section 3.5.3.

The next step is the construction of the discrete divergence operator as a discrete version of the divergence theorem.

Definition 3.3. *The discrete divergence operator $\mathcal{DIV}_h$ is defined for each $\mathbf{u} \in X_h$ as*

$$(\mathcal{DIV}_h \mathbf{u})_E := \frac{1}{|E|} \sum_{i=1}^{k_E} u_{e_i}^E |e_i|. \tag{3.64}$$

To find the discrete version of ∇, we use the Gauss-Green formula

$$\int_E \vec{v}(\nabla p)\, d\vec{x} + \int_E p \operatorname{div} \vec{v}\, d\vec{x} = \int_{\partial E} p\vec{v} \cdot \vec{n}_E\, ds. \tag{3.65}$$

If the boundary term vanishes due to boundary conditions, we see that $-\nabla$ is the adjoint of div

$$-\nabla = \operatorname{div}^*. \tag{3.66}$$

It is therefore natural to demand that the discrete versions of $-\mathbf{K}\nabla$ and div are adjoint,

$$\mathcal{G}_h = \mathcal{DIV}_h^*, \tag{3.67}$$

with respect to the inner products (3.61) and (3.62). We get the following definition for the discrete gradient:

Definition 3.4. *The discrete gradient operator $\mathcal{G}_h$ is defined as the adjoint to the discrete divergence operator $\mathcal{DIV}_h$ with respect to the scalar products* (3.61) *and* (3.62)*, so that*

$$[\mathbf{v}, \mathcal{G}_h \mathbf{p}]_{X_h} = [\mathbf{p}, \mathcal{DIV}_h \mathbf{v}]_{Q_h} \quad \forall \mathbf{p} \in Q_h \text{ and } \forall \mathbf{v} \in X_h. \tag{3.68}$$

As a result, $\mathcal{G}_h$ completely depends on the definition of the inner product matrix $\mathbf{M}_E$ in (3.63). Thus, the particular discretization of (3.60) depends on how $\mathbf{M}_E$ is chosen, meaning that different inner products give different mimetic FDMs.

Implementation

We start by discretizing (3.59) by considering the discrete divergence $\mathcal{DIV}_h$ defined in (3.64). Let $\mathbf{v}_E = (v_1^E, v_2^E, \ldots, v_{k_E}^E)^T$, and let $\mathbf{f}_E = |E|(\mathbf{f}_m)_E$. The equation for each cell E is

$$\sum_{i=1}^{k_E} v_{e_i}^E |e_i| = \mathbf{f}_E, \tag{3.69}$$

or equivalently for fluxes: $F_{e_i}^E = v_{e_i}^E |e_i|$:

$$\sum_{i=1}^{k_E} F_{e_i}^E = \mathbf{f}_E. \tag{3.70}$$

It is not as straight forward to discretize (3.60), since the discrete gradient $\mathcal{G}_h$ is only defined as the adjoint to $\mathcal{DIV}_h$. The trick is to exploit (3.68) to do a "discrete partial integration". First, observe that a weak formulation of (3.60) is given by

$$[\mathbf{v}_h, \mathbf{u}]_{X_h} = [\mathcal{G}_h \mathbf{p}_h, \mathbf{u}]_{X_h}, \quad \forall \mathbf{u} \in X_h. \tag{3.71}$$

We now use (3.68), resulting in

$$[\mathbf{v}_h, \mathbf{u}]_{X_h} = [\mathbf{p}_h, \mathcal{DIV}_h \mathbf{u}]_{X_h}, \quad \forall \mathbf{u} \in X_h, \tag{3.72}$$

which is used to discretize (3.60).

Let $\mathbf{D}$ be a diagonal matrix containing $|e_i|$ for $e_i \in \partial E$. After a hybridization, see Section 3.4.3, (3.72) yields the following expression for the flux in a cell E.

$$\mathbf{F}_E = -\mathbf{D}\mathbf{M}_E^{-1}\mathbf{D}(\boldsymbol{\lambda}_E - p_E). \tag{3.73}$$

Then we can do a Schur-complement reduction, as was done for the hybrid mixed FEM in Section 3.4.3, with the result that only $\mathbf{W}_E := \mathbf{M}_E^{-1}$ is needed for the implementation. We therefore refer to $\mathbf{W}_E$ as the mimetic inner product in the following. Observe that (3.73) corresponds to (3.48) with

$$\mathbf{T}_E = \mathbf{D}\mathbf{W}_E\mathbf{D}. \tag{3.74}$$

In the next section we will give criteria on $\mathbf{W}_E$ that gives stable, convergent methods on general polyhedral grids.

3.5.3 Inner products for Mimetic FDMs

Different choices of the mimetic inner product $\mathbf{W}_E$ give different mimetic FDMs. In fact, both the TPFA method and the RT_0-mixed FEM can be created by special choices of $\mathbf{W}_E$ for Cartesian grids. The mimetic inner product for RT_0-mixed FEM is found in [4], while TPFA is created by $\mathbf{T}_E$ equal to the transmissibility matrix defined in (3.18). But as we have already seen, the TPFA is not convergent on general grids, and the RT_0-mixed FEM is hard to implement on general grids. However, by demanding two conditions on $\mathbf{W}_E$ to be satisfied [9], we can obtain mimetic FDMs that are convergent on unstructured polygonal and polyhedral grids. We list the conditions here, and refer the reader to [9] for the derivation of the conditions and proofs of convergence. The two conditions concern consistency and stability of the method. We present the consistency condition first, and discuss the stability condition at the end of the section. Define the $k_E \times d$ matrices $\mathbf{R}$ and $\mathbf{N}_W$ as

$$\mathbf{R}(i,:) = \int_{e_i} (\vec{x} - \vec{x}_E), \quad \mathbf{N}_W(i,:) = (\vec{n}_{e_i}^E)^T. \tag{3.75}$$

The consistency condition on $\mathbf{W}_E$ stems from the discrete version of the Gauss-Green formula and is given by

$$\mathbf{W}_E\mathbf{R} = \mathbf{N}_W\mathbf{K}. \tag{3.76}$$

Observe that (3.76) is equivalent to the requirement derived for $\mathbf{T}_E$ in (3.56). The following theorem gives a family of matrices that satisfies the consistency condition.

Theorem 3.5 (A family of valid $\mathbf{W}_E$)**.** *Let $\mathbf{Z}$ be a $k_E \times (k_E - d)$ matrix whose image spans the null space of $\mathbf{R}^T$, $\mathrm{span}(\mathbf{Z}) = \ker(\mathbf{R}^T)$, and let $\mathbf{U}$ be an arbitrary symmetric positive definite $(k_E - d) \times (k_E - d)$ matrix. Then the matrix*

$$\mathbf{W}_E := \frac{1}{|E|}\mathbf{N}_W\mathbf{K}\mathbf{N}_W^T + \mathbf{Z}\mathbf{U}\mathbf{Z}^T, \tag{3.77}$$

is symmetric and positive definite and satisfies $\mathbf{W}_E\mathbf{R} = \mathbf{N}_W\mathbf{K}$.

We refer the reader to [10] for the proof of this theorem. The equivalent theorem for $\mathbf{T}_E$ is obtained by using $\mathbf{T}_E = \mathbf{D}\mathbf{W}_E\mathbf{D}$.

Theorem 3.6 (A family of valid $\mathbf{T}_E$)**.** *Let $\mathbf{Z}$ and $\mathbf{U}$ be as defined in Theorem 3.5. Then the matrix*

$$\mathbf{T}_E := \frac{1}{|E|}\mathbf{N}\mathbf{K}\mathbf{N}^T + \mathbf{D}\mathbf{Z}\mathbf{U}\mathbf{Z}^T\mathbf{D}, \tag{3.78}$$

is symmetric and positive definite and satisfies the requirement made on $\mathbf{T}_E$ in (3.56)*, $\mathbf{T}_E\mathbf{C}_T = \mathbf{N}\mathbf{K}$.*

Proof. We have that $\mathbf{T}_E = \mathbf{D}\mathbf{W}_E\mathbf{D}$ and $\mathbf{T}_E$ is thus symmetric and positive definite by Theorem 3.5. Moreover, Theorem 3.5 gives $\mathbf{W}_E\mathbf{R} = \mathbf{N}_W\mathbf{K}$. Furthermore, observe that $\mathbf{D}\mathbf{C}_T = \mathbf{R}$ and $\mathbf{D}\mathbf{N}_W = \mathbf{N}$. Now

$$\mathbf{T}_E\mathbf{C}_T = \mathbf{D}\mathbf{W}_E\mathbf{D}\mathbf{C}_T = \mathbf{D}\mathbf{W}_E\mathbf{R} = \mathbf{D}\mathbf{N}_W\mathbf{K} = \mathbf{N}\mathbf{K}, \tag{3.79}$$

which completes the proof. □

We will give an example of a family of matrices satisfying Theorem 3.6.

Corollary 3.7 (The α-inner product)**.** *Let* $\mathbf{Z}$ *be a orthogonal basis for* $\ker(\mathbf{R}^T)$*, then*

$$\mathbf{T}_E = \frac{1}{|E|}\Big(\mathbf{N}\mathbf{K}\mathbf{N}^T + \alpha\,\mathrm{tr}(\mathbf{K})\mathbf{D}\mathbf{Z}\mathbf{Z}^T\mathbf{D}\Big) \tag{3.80}$$

satisfies Theorem 3.6 with $\mathbf{U} = \frac{1}{|E|}\alpha\,\mathrm{tr}(\mathbf{K})\mathbf{I}$.

The stability condition on $\mathbf{W}_E$ given in [9] implies that $\mathbf{U}$ should be constructed such that the extreme eigenvalues of $\mathbf{U}$ are within those of $\mathbf{K}$. To improve the material properties of $\mathbf{M}_E$, Brezzi et al. [10] recommends to multiply $\mathbf{U}$ by a characteristic value of $\mathbf{K}$ such as the trace of $\mathbf{K}$. This requirement is made with the velocity $\vec{v}$ as the unknown flow variable. It is shown in [4] that the inner product defined in (3.80) satisfies a similar stability condition for flux when $\mathbf{K}$ is isotropic and $\alpha = 2$. In this case, the resulting mimetic method is equivalent to RT_0-mixed FEM on Cartesian grids. The mimetic methods defined by (3.80) will be used for simulations in Chapters 5 and 6.

3.5.4 Constructing the linear system

Now that $\mathbf{T}_E$ is defined, we can use (3.70) and (3.73) to construct a linear system for determining the flux and the pressure. The continuity of the flux must be forced by an extra set of equations since (3.73) is hybridized. Thus, if e is a shared edge of cell E_1 and E_2, we must demand that $F_e^{E_1} = -F_e^{E_2}$. Lastly, the boundary conditions must be incorporated.

Consider now all cells $E \in \Omega_h$, where the cells and edges are numbered globally and locally in a logical Cartesian manner. Further, let m be the number of cells, with l the number of edges after a global numbering, and finally, let n be the number of edges after a local (cell-wise) numbering. We define:

- $\mathbf{F}$: vector of fluxes, indexed locally for each cell, $\mathbf{F} = (\mathbf{F}_{E_1}, \mathbf{F}_{E_2}, \ldots, \mathbf{F}_{E_n})^T$, where $\mathbf{F}_E = (F^E_{e_1}, F^E_{e_2}, \ldots, F^E_{e_{k_E}})^T$. Observe that internal or non-boundary edges will appear twice in the vector, so the vector is of size n.
- $\mathbf{p}$: vector of pressures in center of each cell $\mathbf{p} = (p_1, p_2, \ldots, p_m)^T$ indexed as the cells.
- $\boldsymbol{\lambda}$: pressure on the edges, $\boldsymbol{\lambda} = (\lambda_1, \lambda_2, \ldots, \lambda_l)^T$. This vector is indexed globally so that all edges appear only once.

- $\mathbf{f}$: represents the source function, $\mathbf{f} = |E| f_E$.

The resulting linear system is given by,

$$\begin{pmatrix} \mathbf{A} & \mathbf{B}^T & \mathbf{C}^T \\ \mathbf{B} & \mathbf{0} & \mathbf{0} \\ \mathbf{C} & \mathbf{0} & \mathbf{0} \end{pmatrix} \begin{pmatrix} \mathbf{F} \\ -\mathbf{p} \\ \boldsymbol{\lambda} \end{pmatrix} = \begin{pmatrix} \mathbf{0} \\ \mathbf{f} \\ \mathbf{0} \end{pmatrix}, \tag{3.81}$$

where the matrix $\mathbf{A}$ has the following form

$$\mathbf{A} = \begin{pmatrix} \mathbf{T}_{E_1}^{-1} & 0 & \dots & 0 \\ 0 & \mathbf{T}_{E_2}^{-1} & 0 & 0 \\ 0 & 0 & \ddots & 0 \\ 0 & \dots & 0 & \mathbf{T}_{E_N}^{-1} \end{pmatrix}. \tag{3.82}$$

Further, $\mathbf{C}^T$ gives a relationship between the global indexing of the pressure at the edges and the local index of the cell. The conservation of mass, (3.3), is ensured through $\mathbf{BF} = \mathbf{f}$. Lastly, $\mathbf{CF} = \mathbf{0}$ ensures continuity in the flux for internal edges and incorporates the no-flow boundary condition (3.4) for boundary edges.

Notice that the linear system (3.81) is on the same form as the hybrid mixed FEM system (3.42). The differences are that the unknown for flow is flux $\mathbf{F}$ instead of the velocity $\vec{v}$, and that the mass matrix $\mathbf{A}$ is obtained differently. The mass matrix in mixed FEM is also obtained from an inner product, but for mixed FEM the inner product is continuous. As we have already mentioned, we can construct a mimetic inner product that is equal to RT_0-mixed MFEM on Cartesian grids. This will be used in Chapters 5 and 6.

3.6 Implementation of Boundary Conditions and Wells

A general linear system from a hybrid discretization of (3.2)–(3.4) is given as

$$\begin{pmatrix} \mathbf{A} & \mathbf{B}^T & \mathbf{C}^T \\ \mathbf{B} & \mathbf{0} & \mathbf{0} \\ \mathbf{C} & \mathbf{0} & \mathbf{0} \end{pmatrix} \begin{pmatrix} \mathbf{F} \\ -\mathbf{p} \\ \boldsymbol{\lambda} \end{pmatrix} = \begin{pmatrix} \mathbf{a} \\ \mathbf{b} \\ \mathbf{c} \end{pmatrix}, \tag{3.83}$$

where $\mathbf{b}$ is the source vector previously called $\mathbf{f}$. We have seen that the Neumann no-flow boundary conditions used in the derivation of mixed FEM and mimetic FDM results in $\mathbf{a} = \mathbf{0}$ and $\mathbf{c} = \mathbf{0}$. Assume therefore $\mathbf{a} = \mathbf{0}$ and $\mathbf{c} = \mathbf{0}$, when we now explain how general boundary conditions and wells are incorporated in the system. The number of boundary conditions needed in the hybrid discretization presented here is equal to the number of boundary edges if we use Dirichlet or a combination of Dirichlet and Neumann boundary conditions. If only Neumann boundary conditions are applied, we must have an additional condition on the pressure as discussed in the beginning of this chapter. It is important not to apply more boundary conditions than what is needed, as too many boundary conditions can result in an overdetermined system.

3.6.1 Boundary conditions

Assume that e is a boundary edge with corresponding global index j and local index k.

Flux boundary

Let $F_e = f_0$ be the flux over edge e. We have

$$\mathbf{C}(j,l) = \begin{cases} 1 & \text{for } l = k, \\ 0 & \text{for } l \neq k. \end{cases} \tag{3.84}$$

To put the flux boundary condition on e into the system we set $\mathbf{c}(j) = f_0$. This process is repeated for every boundary edge that is to be assigned flux boundary conditions.

Pressure boundary

Let $\lambda_e = p_{\text{BC}}$ be the pressure on edge e. To insert this boundary condition into the linear system, we first move the contribution from λ_e to the right hand side of the system,

$$\mathbf{a}(k) = -p_{\text{BC}}. \tag{3.85}$$

Second, we reduce the system by removing λ_e from the unknowns in $\boldsymbol{\lambda}$. In the third step, the matrix $\mathbf{C}$ and the vector $\mathbf{c}$ must also be reduced accordingly. In Matlab notation this yields

$$\mathbf{C}(j,:) = [\,], \quad \mathbf{c}(:,j) = [\,].$$

By reducing $\mathbf{C}$ and $\mathbf{c}$ we remove the flux boundary condition on e, so that the edge has only one boundary condition as required.

In a general case with pressure boundary conditions on a set of edges $\boldsymbol{\lambda}_{\text{BC}}$, the system before reduction can be displayed as

$$\begin{pmatrix} \mathbf{A} & \mathbf{B}^T & \tilde{\mathbf{C}}^T & \mathbf{C}_{\text{BC}}^T \\ \mathbf{B} & \mathbf{0} & \mathbf{0} & \mathbf{0} \\ \tilde{\mathbf{C}} & \mathbf{0} & \mathbf{0} & \mathbf{0} \\ \mathbf{C}_{\text{BC}} & \mathbf{0} & \mathbf{0} & \mathbf{0} \end{pmatrix} \begin{pmatrix} \mathbf{F} \\ -\mathbf{p} \\ \tilde{\boldsymbol{\lambda}} \\ \boldsymbol{\lambda}_{\text{BC}} \end{pmatrix} = \begin{pmatrix} \mathbf{a} \\ \mathbf{b} \\ \tilde{\mathbf{c}} \\ \mathbf{c}_{\text{BC}} \end{pmatrix}, \tag{3.86}$$

where the symbol "$\sim$" marks the reduced matrices and vectors. The reduction is done by moving $\mathbf{C}_{BC}^T \boldsymbol{\lambda}_{BC}$ to the right hand side of the system, and removing the vectors and the matrices associated with the boundary conditions to obtain the reduced system:

$$\begin{pmatrix} \mathbf{A} & \mathbf{B}^T & \tilde{\mathbf{C}}^T \\ \mathbf{B} & \mathbf{0} & \mathbf{0} \\ \tilde{\mathbf{C}} & \mathbf{0} & \mathbf{0} \end{pmatrix} \begin{pmatrix} \mathbf{F} \\ -\mathbf{p} \\ \tilde{\boldsymbol{\lambda}} \end{pmatrix} = \begin{pmatrix} \mathbf{a} \\ \mathbf{b} \\ \tilde{\mathbf{c}} \end{pmatrix}. \tag{3.87}$$

Here, $\mathbf{a}$ has been updated to $\mathbf{a} = -\mathbf{C}_{BC}^T \boldsymbol{\lambda}_{BC}$. Moreover, observe that the entries in the vector $\tilde{\boldsymbol{\lambda}}$ no longer correspond to the global numbering of the edges since

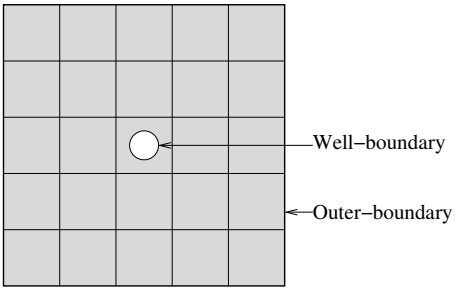

Figure 3.7: Boundaries in the system.

the entries in $\boldsymbol{\lambda}_{BC}$ are removed. However, this has no practical consequences as we can construct $\boldsymbol{\lambda}$ when the system is solved from $\boldsymbol{\lambda}_{BC}$ and $\tilde{\boldsymbol{\lambda}}$.

3.6.2 Wells as a boundary condition

We will later see in Chapter 4 that the following well index relation holds in a well-block

$$q = \text{WI}(p_0 - p_{wf}). \tag{3.88}$$

Here, WI is the well index, q is the well rate, p_0 is the numerically calculated pressure in the well-block, and p_{wf} is the well pressure (pressure at well radius). We use this relation, and the fact that the well can be seen as a boundary edge of the grid, to include the wells in the linear system (3.83). Figure 3.7 shows a gridded domain containing a well with the outer boundary and the well boundary indicated. If we view the well as an edge in the grid, then the pressure on the well-edge is p_{wf} and the flux over the well-edge is q. Assume that the well is in cell i. Equation (3.88) then gives

$$\text{WI}_i^{-1} q_i - p_i + p_{wf,i} = 0. \tag{3.89}$$

We insert this equation into (3.83) and obtain a new linear system including the well

$$\begin{pmatrix} \mathbf{A} & \mathbf{0} & \mathbf{B}^T & \mathbf{C}^T & \mathbf{0} \\ \mathbf{0} & A_w & B_w^T & \mathbf{0} & C_w^T \\ \mathbf{B} & B_w & \mathbf{0} & \mathbf{0} & \mathbf{0} \\ \mathbf{C} & \mathbf{0} & \mathbf{0} & \mathbf{0} & \mathbf{0} \\ \mathbf{0} & C_w & \mathbf{0} & \mathbf{0} & \mathbf{0} \end{pmatrix} \begin{pmatrix} \mathbf{F} \\ q_i \\ -\mathbf{p} \\ \boldsymbol{\lambda} \\ p_{wf,i} \end{pmatrix} = \begin{pmatrix} \mathbf{a} \\ 0 \\ \mathbf{b} \\ \mathbf{c} \\ c_w \end{pmatrix}. \tag{3.90}$$

Here $A_w = \text{WI}_i^{-1}$, $B_w^T(j) = 1$ for $j = i$ and zero otherwise, and $C_w^T = 1$. Even though B_w is a vector, it is not printed in bold to emphasize that the contribution is from one well only. This becomes clear when (3.90) is compared to the final system for all wells which will be presented in (3.91).

The next step depends on which of $p_{wf,i}$ and q_i that is known. If $p_{wf,i}$ is known, we move $a_w = C_w^T p_{wf,i}$ to the right hand side of (3.90), and remove the

last column and row of (3.90). This is equivalent to what was done above for pressure boundary conditions. On the other hand, if q_i is known, the only change done to the system (3.90) is $c_w = q_i$. This process is repeated for all wells in the domain to obtain the final system. Let m be the number of cells. Further let n be the total number of wells, where n_p is the number of wells controlled by pressure (p_{wf} is known) and n_q is the number of wells controlled by rate (q is known). The resulting linear system is

$$\begin{pmatrix} \mathbf{A} & \mathbf{0} & \mathbf{B}^T & \mathbf{C}^T & \mathbf{0} \\ \mathbf{0} & \mathbf{A}_w & \mathbf{B}_w^T & \mathbf{0} & \mathbf{C}_w^T \\ \mathbf{B} & \mathbf{B}_w & \mathbf{0} & \mathbf{0} & \mathbf{0} \\ \mathbf{C} & \mathbf{0} & \mathbf{0} & \mathbf{0} & \mathbf{0} \\ \mathbf{0} & \mathbf{C}_w & \mathbf{0} & \mathbf{0} & \mathbf{0} \end{pmatrix} \begin{pmatrix} \mathbf{F} \\ \mathbf{q} \\ -\mathbf{p} \\ \boldsymbol{\lambda} \\ \mathbf{p}_{wf} \end{pmatrix} = \begin{pmatrix} \mathbf{a} \\ \mathbf{a}_w \\ \mathbf{b} \\ \mathbf{c} \\ \mathbf{c}_w \end{pmatrix}, \tag{3.91}$$

where $\mathbf{A}_w$ is $(n \times n)$, $\mathbf{B}_w$ is $(n \times m)$, $\mathbf{C}_w$ is $(n \times n_q)$, $\mathbf{a}_w$ is $(n \times 1)$, and $\mathbf{p}_{wf}$ and $\mathbf{c}_w$ is $(n_q \times 1)$. Note that $\mathbf{a}_w$ only has n_p non-zero entries.

The method shown above is restricted to 2D. In the following, only 2D wells will be considered, but we show an example of how to implement a well in 3D. Wells in 3D can penetrate several cells and (3.89) will then hold for each cell. If a well for instance penetrates three cells (i, j, k) the contribution from this well is given by

$$A_w = \begin{pmatrix} \mathrm{WI}_i^{-1} & 0 & 0 \\ 0 & \mathrm{WI}_j^{-1} & 0 \\ 0 & 0 & \mathrm{WI}_k^{-1} \end{pmatrix}, \quad q = \begin{pmatrix} q_i \\ q_j \\ q_k \end{pmatrix}, \tag{3.92}$$

and B_w^T is a $3 \times m$ matrix with ones at the entries $(1, i), (2, j), (3, k)$ and zeroes elsewhere, while $C_w = (1, 1, 1)$. For an injection well, the total rate $q = q_1 + q_2 + q_3$ is known, while for a production well the pressure p_{wf} is known.

Chapter 4

Well Modeling

The purpose of this chapter is to introduce the reader to the theory behind well modeling. To set the scene, note that a reservoir simulation results in one pressure value in each grid block. For blocks away from the well, this pressure value is a good approximation to the pressure in the entire block. However, in a well-block, the large pressure variations within the block results in a great deviation between the calculated pressure for the block and the pressure at well radius. The major task in well modeling is to accurately compute the pressure at well radius when the injection or production rate is known, or to accurately compute the rate when the pressure at well radius is known. The corresponding challenges are the large pressure variation within the well-block and that the radius of the well is small compared to the horizontal dimensions of the grid blocks. Peaceman was one of the first to address this problem in [24] and [25]. He introduced the *equivalent radius* r_0 that relates the well block pressure to the pressure at well radius. Peaceman's results are presented in Section 4.2. Moreover, we discuss improvements and extensions of Peaceman's well model. We begin with a short introduction to wells.

4.1 Wells

4.1.1 Introduction

The well has radius r_w, and the pressure at this radius is denoted p_{wf}. In 3D, p_{wf} is denoted the *flowing bottom hole pressure*, but we shall restrict the presentation to 2D and therefore name it the *well pressure*. Furthermore, a grid block perforated by a well is called a *well-block*, and the numerically calculated pressure in the well-block is called the *well-block pressure* (WBP) and is denoted p_0. The radius of a well is typically between 1/100 to 1/1000 of the horizontal length of a grid block [21]. Due to the fact that the greatest percentage of pressure drop occurs close to the well, p_{wf} will deviate greatly from the well-block pressure p_0. This

deviation is modeled by the *well index* relation, defined for single-phase flow as

$$\text{WI} = \frac{q}{(p_0 - p_{wf})}. \tag{4.1}$$

The *well index*, WI, gives a relationship between the well pressure p_{wf}, the well rate q, and the well-block pressure p_0. The definition of WI is based on a straight line inflow performance relation, which can be used to model undersaturated oils [18]. In the following we define a *well model* to be a model used to determine the well index.

The wells in an oil reservoir are used for either production or injection. The production well produces fluids, normally a combination of oil, water, and gas. In the injection well, fluids, normally water, are injected to maintain reservoir pressure and push oil towards the production well. Wells can be constrained by pressure, flow rate, or a combination of these. One typical situation is that p_{wf} is constrained in production wells, and that q is constrained in injection wells. In this case, if WI is known, then (4.1) gives an expression for calculating either q or p_{wf}, depending on whether the well is constrained by rate or pressure. In Section 4.2 we present Peaceman's WI, which is derived under certain assumptions that are presented below.

4.1.2 Assumptions

In well modeling it is common to assume *ideal wells*. The following definition is from [18]:

Definition 4.1. *An ideal well is one that drains a rock with uniform permeability (in all directions), completely penetrated and open to the producing interval through a radial wellbore. Flow is only in the radial direction and the outer boundary is circular.*

The definition above refers to radial flow, another common assumption. Even if several different flow geometries can be expected when fluids flow toward a vertical wellbore, two-dimensional radial flow is considered to be the most representative for the majority of producing vertical oil and gas wells [18]. Most literature on wells concerns vertical wells since the technology for drilling wells has not allowed horizontal wells before the last 10-20 years. The vertical wells are therefore often called *conventional wells*. Now, *non-conventional wells*, which includes horizontal and multilateral wells, are becoming increasingly common. The well index (4.1) can also be used to model horizontal wells if we for instance have a well parallel to the y-axis and assume radial flow in the xz-plane. However, there are usually very high anisotropy ratios between the horizontal and vertical dimension of the well-block, which complicates the well modeling. We shall therefore restrict the discussion to conventional wells in this thesis. A radial flow model of a vertical well is displayed in Figure 4.1.

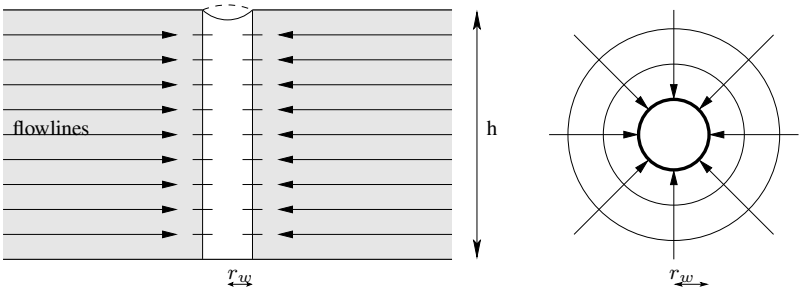

(a) Horizontal view of well (b) Seen from above

Figure 4.1: Radial flow

For the following derivation we assume steady-state, single-phase, horizontal flow in two-dimensions in a homogeneous and isotropic reservoir. In addition, we assume ideal wells, and that the flow is radial near the well. Under these assumptions, there exists an analytical flow model near the well given by

$$p(r) = \frac{q\mu}{2\pi kh} \ln\Big(\frac{r}{r_w}\Big) + p_{wf}. \tag{4.2}$$

Here, r is the distance from the well and h is the reservoir thickness. A derivation of this equation can be found in for instance [23, pages 150-153]. Equation (4.2) will be used to develop an expression for the well index in the following.

4.1.3 The repeated five-spot pattern problem

To derive analytical well models, we must also make simplifications and additional assumptions on the reservoir. A typical real-life reservoir has complicated geometry and boundaries, and there exists no analytical solution for the flow and pressure throughout the reservoir. However, there are some theoretical reservoir problems where an analytical solution is known. These problems are practical for testing and developing new models and can be used in our case of well modeling. One such theoretical reservoir problem is the *repeated five-spot pattern*. This problem is described as a thin, infinitely large, horizontal reservoir with a pattern of injection and production wells as shown in the section given in Figure 4.2. The name comes from the fact that each injection well is surrounded by four production wells and vice versa, hence creating a five spot. Moreover, due to the symmetry of the problem, it is common to only consider the *quarter five spot*, marked by dashed lines in the figure, when solving the problem. Among the analytical results for this problem is Muskat's equation [23] for the pressure drop between injection and producing wells, given by

$$\Delta p = \frac{q\mu}{\pi kh}\Big(\ln\big(\frac{d}{r_w}\big) - B\Big). \tag{4.3}$$

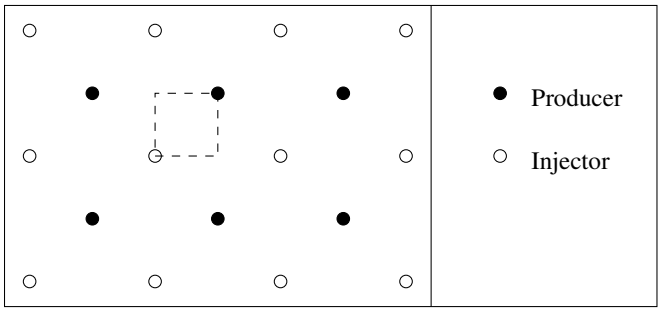

Figure 4.2: Section of repeated five-spot pattern. The quarter five-spot is marked by dashed lines

Here, d is the diagonal distance between the wells, and B is given by an expression including an infinite series. Muskat [23] originally used $B = 0.6190$, but a more accurate value,

$$B = 0.61738575, \tag{4.4}$$

was derived by Peaceman in [25] and will be used in the following. Muskat's equation will be used in the next section to calculate Peaceman's equivalent radius, r_0.

4.2 The Peaceman Well Model

The first to derive an expression for the well index was Peaceman in [24]. The idea is as follows. If the numerically calculated well-block pressure p_0 is equal to the analytical pressure at a known radius r_0 and (4.2) holds near the well, we get the following expression for the well index

$$\text{WI} = \frac{2\pi kh}{\mu \ln(r_0/r_w)}. \tag{4.5}$$

The problem of finding the well index now consists of finding r_0.

In [24], Peaceman showed that under the assumptions stated in the introduction, the numerically calculated well-block pressure from the TPFA method (see Section 3.3), is equal to the actual flowing pressure at radius r_0. Peaceman used the five-spot pattern problem to derive both numerical and analytical expressions for r_0. For a grid with square grid blocks, $\Delta x = \Delta y$, he showed that r_0 can be calculated by

$$r_0 = 0.2\Delta x, \tag{4.6}$$

where 0.2 is a rounded mean from the different derivations. The radius r_0 is called the *equivalent radius*, or the *effective well-block radius*. The former will be adapted in this thesis. Note that the use of the equality sign in (4.6) is a slight abuse of

notation since the constant 0.2 is an approximated quantity. Nevertheless, we will continue to use this notation, following tradition.

Grid blocks in reservoir simulation are seldom square, but to the contrary they often have large horizontal dimensions compared to the vertical dimension. Well models for non-square grid blocks, $\Delta x \neq \Delta y$, are therefore important. In [25], Peaceman derived an expression for the equivalent radius for non-square grid blocks given by

$$r_0 = 0.14(\Delta x^2 + \Delta y^2)^{\frac{1}{2}}. \tag{4.7}$$

Observe that (4.7) simplifies to (4.6) when $\Delta x = \Delta y$ if we round to two significant digits in the answer. We remark that the accuracy is improved in [25] compared to [24], so we will use the results from the former in the the following. Moreover, in [25] the results were also extended to hold for anisotropic permeability, in cases where the principal axes of the permeability tensor are parallel to the x- and y-axes. The expression for r_0 in this case is

$$r_0 = 0.28\frac{((k_y/k_x)^{\frac{1}{2}}\Delta x^2 + (k_x/k_y)^{\frac{1}{2}}\Delta y^2)^{\frac{1}{2}}}{(k_y/k_x)^{\frac{1}{4}} + (k_x/k_y)^{\frac{1}{4}}}. \tag{4.8}$$

This expression simplifies to (4.7) when $k_x = k_y$.

We now show how r_0 can be derived numerically for isotropic permeability. The reader is referred to [24, 25] for details on the analytical derivation. Consider now a quarter five-spot of size $n \times m$ cells, where Δx and Δy denotes the grid spacing in the x- and y-directions, respectively. Further, denote by Δp the numerically calculated pressure drop between the injector and producer well-blocks, $\Delta p = p_{n,m} - p_{0,0}$. Then r_w can be replaced by r_0 in (4.3) to yield the following formula for r_0:

$$r_0 = \sqrt{2}n\Delta x \exp\Big(-B - \frac{\pi kh}{q\mu}(p_{n,m} - p_{0,0})\Big). \tag{4.9}$$

This formula will be used in Chapter 5 to generalize Peaceman's well model to mimetic FDMs.

4.3 Extensions of Peaceman's Well Model

More than 20 years have gone by since Peaceman published the results presented above, and much has happened in that time. The well drilling technology has developed to allow among other slanted and curved wells, and techniques for more accurate reservoir simulation have also been developed. The need for more complex well models has thus emerged. As a result, there are currently many methods for computing well indices based on different assumptions and well configurations. We will not make an attempt to list all these methods here, but mention some examples. An extension of Peaceman's WI for deviated wells, hereafter called the

projection method, was developed by Holmes [28] and is implemented in a pre-processor for the Eclipse simulator. Further, a semi-numerical WI for slanted and curved wells was developed by Klausen and Aavatsmark in [6]. Moreover, a general semi-analytical WI for non-conventional wells was derived by Wolfsteiner et al. [31], by the use of Green's functions as a reference single-phase flow solution.

Shu performed a comparison study of the projection method and the semi-analytical method against Peaceman's method in [29]. The study included horizontal, vertical 2D and 3D slanted wells in a homogeneous reservoir with uniform Cartesian grids. Both isotropic and anisotropic reservoirs were tested. The results revealed that Peaceman's well model can lead to significant errors in the cases of slanted wells, interference from other wells or boundaries, and spherical near-well flow. In addition, the projection method was also shown to be vulnerable to spherical flow and boundary effects. The semi-analytical WI, on the other hand, computed accurate well indices for all the tested cases. From this we conclude that Peaceman's well model must be used with caution in the cases listed above. However, despite the known weaknesses in Peaceman's well model, it is still the default well model in most commercial simulators [30].

One common feature of all the mentioned methods for computing well indices is that they are developed for the TPFA or equivalent cell centered finite difference schemes. The TPFA is the predominant method in reservoir simulation, despite the fact that the method has several shortcomings, as shown in Section 3.3. Thus, in some cases it is favorable to use other methods than TPFA for reservoir simulation, such as mimetic FDMs. Different numerical methods give different well-block pressures. Therefore, the use of other methods than TPFA creates a need for the development of corresponding well indices. Some simple extensions of Peaceman's method have been done for FEM and mixed FEM, see for instance [12] or [17], but to the best of the author's knowledge there are no results for mimetic FDMs. Another problem is that even though the majority of well indices are derived under the assumption of homogeneous reservoirs, they are often used for heterogeneous reservoirs.

In this thesis we will address both these issues. In Chapter 5 we extend the Peaceman well model to mixed FEM and mimetic FDMs. Extension of Peaceman's well model to mimetic methods is a starting point and will create a foundation for further work on more complex well models for mimetic FDMs. Second, in Chapter 6 we test the performance of the new well indices on both homogeneous and heterogeneous reservoirs to examine the validity of the extended well models in different cases.

The extension of Peaceman's well model is done by calculating the numerical well index for mimetic FDMs. We remark that the results for TPFA in (4.6) and (4.7) are derived both numerically and analytically, but for mimetic FDMs it is not straight forward to obtain analytical results. However, the results from the different derivations of (4.7) give the same result when rounded to the fourth significant digit (0.140365 vs 0.1403649). Therefore, we conclude that it is sufficient to derive the results in the extension numerically.

Chapter 5

Development of Well Models for Mimetic Methods

In this chapter we reproduce Peaceman's results for the equivalent radius presented in (4.6) and (4.7). As mentioned in the previous chapter, Peaceman's well model was developed for the two-point flux approximation method, a method which does not converge on general grids with general permeability tensors. Thus, it would be beneficial to extend Peaceman's results to more flexible numerical methods. In particular, we consider the well-known lowest order Raviart-Thomas mixed FEM and a mimetic FDM, and derive expressions for the equivalent radius for these methods. Furthermore, we investigate the connection between the inner product in mimetic FDMs and the equivalent radius by looking at one-parameter family of mimetic FDMs. Finally, the chapter is completed by a verification of the obtained results.

5.1 Setup for Numerical Simulations

In Chapter 4 we saw that the numerical equivalent radius for a given method is found by solving the five-spot pattern problem and inserting the results for the pressure drop $\Delta p = (p_{\text{injector}} - p_{\text{producer}})$ in the formula

$$r_{0,c} = \sqrt{2} n \Delta x \exp\Big(-B - \frac{\pi k h}{q\mu} \Delta p\Big). \tag{5.1}$$

This formula stems from Muskat's equation (4.3) for the pressure drop between injection and producing wells in a repeated five-spot pattern. Solving the repeated five-spot pattern problem means solving for an infinite reservoir. In computational science, an infinite system is usually modeled by a finite simulation cell or grid subject to periodic boundary conditions. Due to the symmetry of the repeated five-spot pattern, we can employ this technique here. To be able to use periodic boundary conditions, the simulation cell must be chosen as a five-spot where the grid is staggered with half a cell in each direction compared to a grid used to

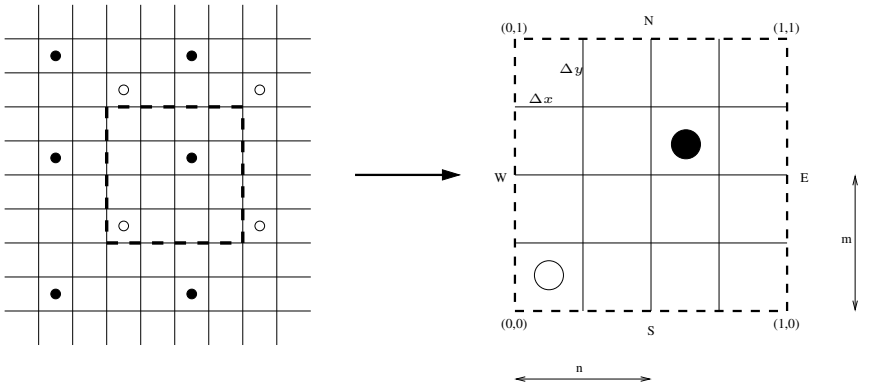

Figure 5.1: The simulation cell (right) is a section of the infinite five-spot pattern (left).

simulate a quarter five-spot. This setup is shown in Figure 5.1. Observe that the simulation cell has twice the number of grid cells in each direction compared to the quarter five-spot. For the notation to be consistent with the one used in [24,25], where a quarter five-spot of size $n \times m$ was used, we use a simulation cell of size $2n \times 2m$ grid cells. Moreover, the simulation cell is scaled to the unit cell for simplicity.

We denoted the boundary edges by *South, East, West, and North*. In the continuous case, the periodic boundary conditions for the problem are

$$\mathbf{v}(1, y) = \mathbf{v}(0, y), \quad \forall y \in [0, 1], \tag{5.2}$$
$$\mathbf{v}(x, 1) = \mathbf{v}(x, 0), \quad \forall x \in [0, 1]. \tag{5.3}$$

In the discrete case, the flow is not measured as the velocity in each point, but instead as the flux $\mathbf{F}_e$ over each edge e, as defined in (3.2). Thus, the boundary conditions on a Cartesian grid become

$$\mathbf{F}(e_{\text{east}}) = \mathbf{F}(e_{\text{west}}), \tag{5.4}$$
$$\mathbf{F}(e_{\text{north}}) = \mathbf{F}(e_{\text{south}}), \tag{5.5}$$

for all boundary edges. Here e_{east} and e_{west} are opposite boundary edges with equal y-coordinates, while e_{north} and e_{south} are opposite boundary edges with equal x-coordinates.

The prototype flow problem (3.2)–(3.4) is solved by a mimetic simulator [4] developed at the Dept. of Applied Mathematics in SINTEF ICT. This simulator has support for different mimetic inner products. As explained in Chapter 3, both TPFA and RT_0-mixed FEM can be created by mimetic inner products. Thus, by changing the inner product, the same code can be used to simulate TPFA, RT_0-mixed FEM, and different mimetic FDMs.

In the simulations we calculate the numerical equivalent radius, $r_{0,c}$, using (5.1). The assumptions of a homogeneous and isotropic reservoir means that the permeability is given by $\mathbf{K} = k\mathbf{I}$, where $\mathbf{I}$ is the identity matrix. For simplicity we set $k =$ and $h = 1$. Furthermore, to simplify the notation and the presentation of the results, we define the *aspect ratio* of the grid cells

$$\beta = \Delta x/\Delta y,$$

and the *well constants*

$$\gamma = r_0/\Delta x,$$
$$\xi = r_0/(\Delta x^2 + \Delta y^2)^{\frac{1}{2}}.$$

In the following we will refer to a grid with square cells, $\beta = 1$, as a square grid, while a grid with non-square cells is referred to as a non-square grid. Observe that $\xi = \gamma/\sqrt{2}$ for square grids. As already mentioned, the grids in the simulations will be of size $2n \times 2m$. For square grids, we specify n and let $m = n$, while for non-square grids m is specified and $n = \beta m$.

5.2 Reproduction of Peaceman's Results

We did numerical simulations to reproduce the results in (4.6) and (4.7) using the setup described in the previous section. For square grids, the smallest grid had $n = 1$, and n was successively doubled up to $n = 256$. The results for square grids are displayed in Table 5.1(a). As we can see in the table, γ is converging to the limit ≈ 0.1985 which agrees with Peaceman's result in [25] to the fourth significant digit. The value of γ for $n = 1$ and $n = 2$ deviates strongly from the other values, which is not surprising since the simulation grids are very coarse in these cases.

For non-square grids, the tested cases are $m = \{2, 8, 32\}$ and $n = \beta m$, starting with $\beta = 2$ and successively doubling β up to $\beta = 128$. The results displayed in Table 5.1(b) show that ξ converges to 0.140. Observe that the results for the finest grid resolution for $\beta = \{32, 64, 128\}$ are equal, which means that the solution has converged and there is no need to test for higher β. The results in the table are in good agreement with the results in [25], where Peaceman extrapolated values for $m = 16$ and $m = 32$ to find $\xi = 0.140365$. For each aspect ratio in the table, ξ for the finest grid agrees with Peaceman's extrapolated value down to the fourth significant digit. The values of ξ for the grids with $m = 2$ deviate strongly from the finest grids, as we also saw for square grids, which is not surprising considering the low resolution of the grids.

5.3 Equivalent Radius for MFEM and MFDM

Now that we have verified our setup for finding the equivalent radius, the results can be extended to other numerical methods. In particular, we consider the RT_0-mixed

Table 5.1: Reproduction of Peaceman's results for TPFA

(a) Square grids.

n	γ
1	0.158562
2	0.187860
4	0.195908
8	0.197858
16	0.198344
32	0.198465
64	0.198496
128	0.198503
256	0.198505

(b) Non-square grids.

β	m	ξ
2	2	0.135598
2	8	0.140078
2	32	0.140347
4	2	0.136230
4	8	0.140120
4	32	0.140350
8	2	0.136384
8	8	0.140131
8	32	0.140350
16	2	0.136423
16	8	0.140134
16	32	0.140350
32	2	0.136432
32	8	0.140134
32	32	0.140351
64	2	0.136435
64	8	0.140134
64	32	0.140351
128	2	0.136435
128	8	0.140135
128	32	0.140351

Table 5.2: Results from simulations with MFEM and MFDM on square grids.

	MFEM	MFDM
n	γ	γ
1	0.451847	0.267668
2	0.434177	0.283467
4	0.419246	0.284817
8	0.415182	0.284907
16	0.414169	0.284913
32	0.413915	0.284913
64	0.413852	0.284913
128	0.413836	0.284913
256	0.413832	0.284913

FEM and the mimetic FDM defined by the α-inner product (3.80) with $\alpha = 1$. These methods are hereafter referred to as MFEM and MFDM, respectively.

New numerical simulations were done by solving the flow and pressure system with MFEM and MFDM instead of TPFA. For square grids, n was successively doubled, while for non-square grids $m = \{2, 8, 32\}$ and $n = \beta m$, starting with $\beta = 2$ and successively doubling β up to $\beta = 64$. The results from the simulations are shown in Table 5.2 for square grids and in Table 5.3 for non-square grids. We observe from the tables that the well constant of MFDM converges faster than the well constant for MFEM. Moreover, the results for square grids suggest that the equivalent radius for MFEM is given by

$$r_0 = 0.4138\Delta x, \tag{5.6}$$

and that the equivalent radius for MFDM is given by

$$r_0 = 0.2849\Delta x. \tag{5.7}$$

These formulas are on the same form as Peaceman's result for the TPFA method for square grids shown in (4.6), and only differing in the value of the constant γ.

Turning to non-square grids, Peaceman's results do not generalize that easily. Remembering Peaceman's result for non-square grids in (4.7), we look for an approximation to r_0 for MFEM and MFDM on the form

$$r_0 = \xi(\Delta x^2 + \Delta y^2)^{\frac{1}{2}}. \tag{5.8}$$

The results from simulations using non-square grids are shown in Table 5.3. As seen in the table, the constant ξ changes for each aspect ratio β for both MFEM and MFDM. These results are in contrast to the results obtained for TPFA, where ξ is the same for all β. A plot of the variation in ξ for MFEM is shown in Figure 5.2, where the results for ξ from the finest grid resolution for each β is plotted against β. There is no apparent connection between ξ and β to be drawn from the

Table 5.3: Results from simulations with MFEM and MFDM on non-square grids

β	m	MFEM ξ	MFDM ξ
2	2	0.286178	0.195305
2	8	0.278546	0.195853
2	32	0.278015	0.195855
4	2	0.257622	0.185081
4	8	0.251998	0.185574
4	32	0.251590	0.185576
8	2	0.236703	0.177135
8	8	0.231819	0.177605
8	32	0.231461	0.177607
16	2	0.224514	0.172402
16	8	0.219946	0.172859
16	32	0.219611	0.172861
32	2	0.218001	0.169848
32	8	0.213582	0.170298
32	32	0.213257	0.170300
64	2	0.214644	0.168526
64	8	0.210296	0.168972
64	32	0.209976	0.168974

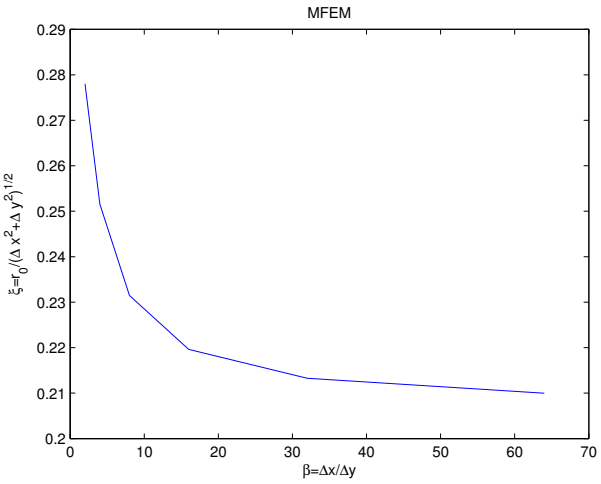

Figure 5.2: Variation in equivalent radius-factor ξ for different aspect ratios for MFEM.

Table 5.4: Well constants for MFEM and MFDM. The odd numbered aspect ratios are provided for the simulations in Chapter 6.

	MFEM	MFDM
β	ξ	ξ
1	0.293	0.201
2	0.278	0.196
3	0.262	0.190
4	0.252	0.186
5	0.244	0.183
8	0.231	0.178
9	0.229	0.177
16	0.220	0.173
17	0.219	0.173
32	0.213	0.170
33	0.213	0.170
64	0.210	0.169
65	0.210	0.169

figure, except that ξ seems to be converging as $\beta \to \infty$. Polynomial and various exponential fitting of the data were tried without success. There might still be a relationship between ξ and β, but not in a simple form.

We sum up the results so far with the following rule for computing the equivalent radius.

Rule 5.3.1. *The approximate equivalent radius for a numerical method $M \in \{$TPFA, MFEM, MFDM$\}$ on a grid with aspect ratio $\beta = \Delta x/\Delta y$ is given by*

$$r_{0,c}(M, \beta) = \xi(M, \beta)(\Delta x^2 + \Delta y^2)^{\frac{1}{2}}, \tag{5.9}$$

where $\xi($MFEM$, \beta)$ and $\xi($MFDM$, \beta)$ is given in Table 5.4, and $\xi($TPFA$, \beta) = 0.14$.

We remark that the well constants in Table 5.4 are rounded to three significant digits, because this corresponds to the accuracy from using $\xi = 0.140 = 0.14$ for Peaceman's equivalent radius. The results can easily be extended to hold for anisotropic permeability through (4.8), but this extension will not be considered here.

5.4 Equivalent Radius for a General Mimetic Method

The results so far show that the equivalent radius must be computed for each numerical method. Mimetic FDMs is a large class of methods, and it would be practical to find a general connection between the inner product and the equivalent radius of a method. In an attempt to do so, we consider a one-parameter family of mimetic

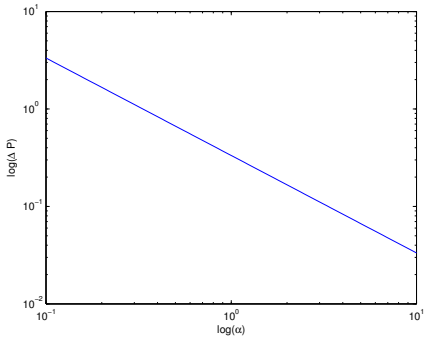

Figure 5.3: Logarithmic plot of Δp against α for $n = 1$.

FDMs, named here the QR-MFDM, and try to find a relationship between the one degree of freedom and the corresponding equivalent radius.

Assume we have an isotropic and homogeneous reservoir where $\mathbf{K} = \mathbf{I}$. Furthermore, assume that the grid is Cartesian with square cells. Under these assumptions, the α-inner product in Corollary 3.7 simplifies to

$$\mathbf{T}_E = \frac{1}{|E|}\mathbf{N}\mathbf{N}^T + 3\alpha(\mathbf{I} - \mathbf{Q}\mathbf{Q}^T), \tag{5.10}$$

where $\mathbf{Q}$ is an orthogonal basis for the matrix $\mathbf{R}$. Thus, $\mathbf{I} - \mathbf{Q}\mathbf{Q}^T = \mathbf{Z}\mathbf{Z}^T$, where $\mathbf{Z}$ is an orthogonal basis for $\ker(\mathbf{R}^T)$. The matrix $\mathbf{Q}$ can for instance be obtained by a QR-factorization of $\mathbf{R}$. The family of mimetic FDMs given by (5.10) is simple and has one degree of freedom, which makes it suitable for testing purposes. When $\alpha = 1$, the QR-MFDM is equivalent to the MFDM used in the previous section for Cartesian square grids. The equivalent radius for $\alpha = 1$ is therefore given in (5.7).

We would like to investigate whether there is a relationship between r_0 and α. Changing α results in a new linear system (3.81) because $\mathbf{A}^{-1}$ is a block diagonal matrix where the blocks are $\mathbf{T}_E$. One way to detect changes in a matrix is to look at the eigenvalues of the matrix. We therefore look for a relationship between the eigenvalues of $\mathbf{A}^{-1}$, denoted $\boldsymbol{\sigma}(\mathbf{A}^{-1})$, and α. In fact, since $\mathbf{A}^{-1} = \{\mathbf{T}_E\}$, we have $\boldsymbol{\sigma}(\mathbf{A}^{-1}) = \boldsymbol{\sigma}(\mathbf{T}_E)$. Furthermore, observe from the numerical formula for r_0 in (5.1) that for a grid of constant size $n \times n$ the only variable is Δp. Thus,

$$r_0 = r_0(\alpha) = r_0(\Delta p(\alpha)), \tag{5.11}$$

so the variation in r_0 only depends on the variation of Δp by α.

A logarithmic plot of Δp against α for $n = 1$ is shown in Figure 5.3. The graph is a straight line, so

$$\log_{10}(\Delta p) = a \log_{10}(\alpha) + b. \tag{5.12}$$

A linear polynomial approximation gives $a = -1$ and $b = -\log_{10}(3)$. The resulting expression for r_0 is

$$r_0 = \sqrt{2}\Delta x \exp(-B - \frac{\pi}{3\alpha}). \tag{5.13}$$

However, we recall from the results for MFEM and MFDM that the value for $n = 1$ deviated strongly from the limit when $n \to \infty$. Hence, simulations for larger n must be done to get a general result. The results in Section 5.3 show that r_0 is sufficiently converged for $n = 10$. We therefore use $n = 10$ in the following. Figure 5.4(a) displays a logarithmic plot of Δp against α for $n = 10$. Observe that there is no longer a linear relationship between the variables. The regular plot in Figure 5.4(b) is more informative. Here we see that the graph changes behavior around $\alpha = \frac{2}{3}$. This point corresponds to the breakpoints in the graphs of the minimum and maximum eigenvalues of $\mathbf{T}_E$, as shown in Figure 5.4(c). In fact, $\boldsymbol{\sigma}(\mathbf{T}_E) = \{3\alpha, 2\}$. This is shown in the eigenvalue decomposition of $\mathbf{T}_E$ in Appendix B. Hence, at $\alpha = \frac{2}{3}$, $\boldsymbol{\sigma}(\mathbf{T}_E) = \{2\}$.

The graphs indicate a relationship between Δp and $\min(\boldsymbol{\sigma})$ and $\max(\boldsymbol{\sigma})$, where the relationship between Δp and the minimum eigenvalue is most evident. Motivated by this observation we perform a least-square fit, denoted LS-fit 1, to find the coefficients of

$$\Delta p(\alpha) \approx a \min(\boldsymbol{\sigma}(\alpha)) + b, \tag{5.14}$$

and another least-square fit, denoted LS-fit 2, to find the coefficients of

$$\Delta p(\alpha) \approx c \min(\boldsymbol{\sigma}(\alpha)) + d \max(\boldsymbol{\sigma}) + e. \tag{5.15}$$

The resulting lines are plotted against Δp in Figure 5.5(a). The figure shows that LS-fit 1 is a bad approximation as α increases, but that LS-fit 2 is better. Figure 5.5(b) shows r_0 calculated from (5.1) when LS-fit 1 and LS-fit 2 are used to calculate $\Delta p(\alpha)$. The errors we saw in the previous plot are amplified by the exponential function in the formula for r_0, and the result is not good. Even though Δp seems to depend on the eigenvalues of $\mathbf{T}_e$, it is clear from the figure that a linear least square fit does not describe the relationship properly.

Conclusion

The results for QR-MFEM give no definite answer on how to calculate the equivalent radius for a general mimetic FDM. We have seen that the equivalent radius of a numerical method depends on how the method approximates the pressure in the well-block. Finding a general expression for the equivalent radius for a one parameter family of inner products is therefore not a simple task, and would require a more thorough study than done here. However, we have shown that there is a connection between the eigenvalues of $\mathbf{T}_E$ and the pressure drop calculated by the method. This pressure drop is used in the numerical formula for calculating r_0. Hence, the results imply a connection between the eigenvalues of $\mathbf{T}_E$ and r_0. The

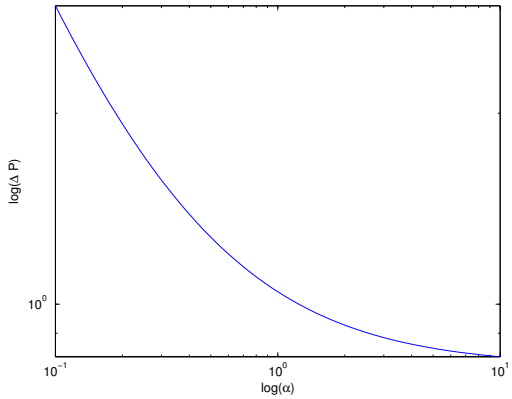

(a) Logarithmic plot of Δp against α.

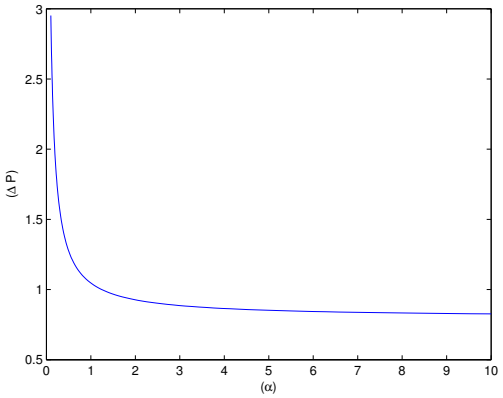

(b) Plot of Δp against α.

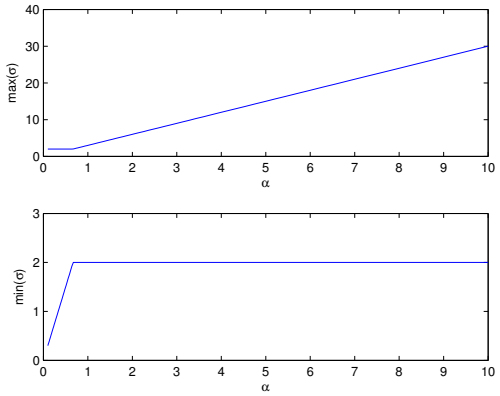

(c) Plot of max($\boldsymbol{\sigma}$) and min($\boldsymbol{\sigma}$) of $\mathbf{T}_E$ against α.

Figure 5.4: Comparing properties of α against r_0 for $n = 10$.

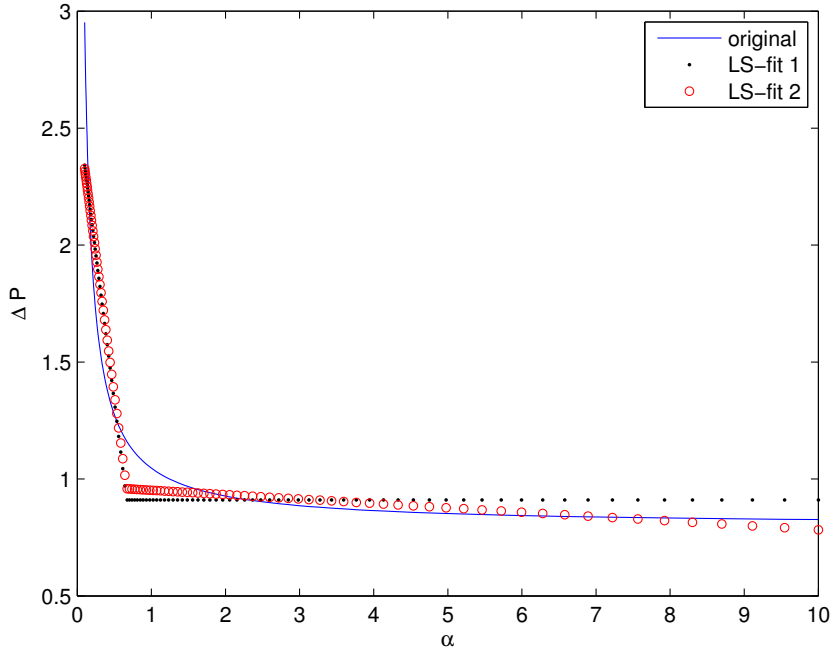

(a) Plot of LS-fit 1, LS-fit 2, and the original Δp against α

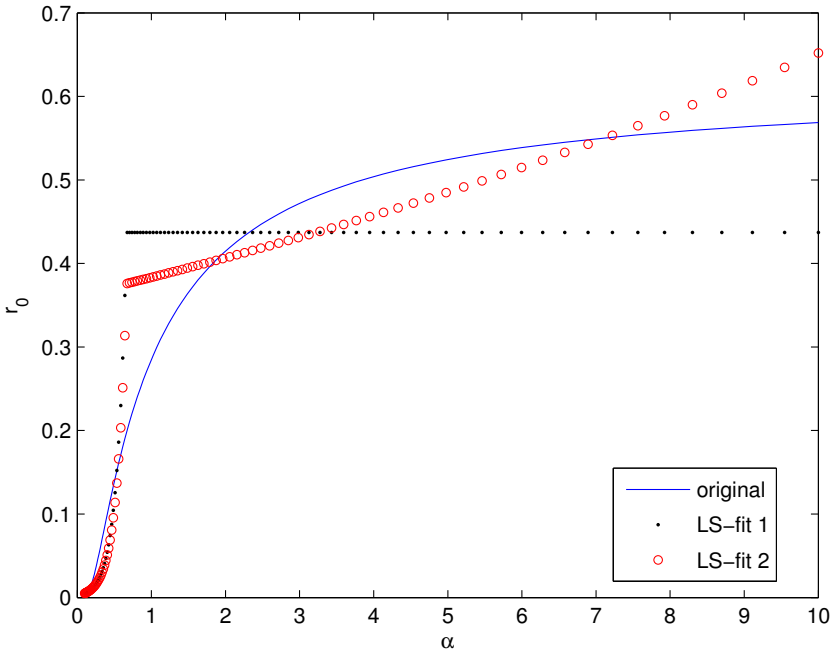

(b) Resulting r_0 when LS-fit1 and LS-fit 2 are used to calculate Δp.

Figure 5.5: Least square fitting of the relationship between r_0 and the max and min eigenvalues of $\mathbf{T}_E(\alpha)$.

approximation methods used here are simple and do not describe this relationship properly. However, we may conclude that r_0 depends on the inner product used, and until an expression for this relationship is found, r_0 must be calculated by the procedure in Section 5.3 for each inner product.

5.5 Verification of New Equivalent Radii

The equivalent radius can also be calculated by a simulation of an infinite reservoir with one well and radial flow. To verify the accuracy of the new equivalent radii for MFEM and MFDM given in (5.9), we calculate r_0 by this alternative procedure and compare the results.

The radial flow simulation is done by forcing appropriate flux boundary conditions. Consider a section of the reservoir containing a well as displayed in Figure 5.6. The flux over each boundary edge is calculated by

$$F_i = \frac{-q\theta_i}{2\pi}, \tag{5.16}$$

where θ is the angle of the circle sector belonging to the boundary edge. We put flux boundary conditions on the system according to (5.16), forcing radial flow from the well. Thus, when the system is solved for pressure and flow, we can use Muskat's equation (4.3) to compute a numerical equivalent radius $r_{0,a}$ from the pressure values in the well-block and on one edge.

For each of the methods $M \in \{\text{TPFA, MFEM, MFDM}\}$ we compute $r_{0,a}$ and the numerical well constant

$$\xi_a(M) = r_{0,a}(M)/(\Delta x^2 + \Delta y^2)^{\frac{1}{2}}. \tag{5.17}$$

Subsequently the values of $\xi_a(M)$ are compared to the values of $\xi_c(M)$ given in Table 5.4 for MFEM and MFDM and to $\xi_c(\text{TPFA}) = 0.14$. The error is measured by looking at $|\xi_a - \xi_c|$. The simulations are done on a Cartesian grid of the unit square, $[0,1]\times[0,1]$, with $2n \times 2n$ cells for square grids and $2n \times 2m$ cells for non-square grids. Furthermore, homogeneous permeability is used for all simulations. We use $m = \{5, 10, 25\}$, $\beta = \{2, 4, 8, 16, 32, 64\}$, and $n = \beta m$.

Table 5.5(a) shows the results for square grids, and Table 5.5(b) shows the results for non-square grids. We see from the tables that $|\xi_a - \xi_c|$ is small for all methods for both square and non-square grids. The well constants $\xi_c(\text{TPFA})$, $\xi_c(\text{MFEM})$, and $\xi_c(\text{MFDM})$ are all rounded to the third significant digit, which corresponds to an error of order 10^{-4}. This error fits good with the errors reported in the table. We see that the error is 10^{-3} for the lowest grid resolution for TPFA and MFEM, because the grid is to coarse to give sufficient convergence of ξ_a. Convergence of the well constant on a coarse grid is not a problem for MFDM, because the well constant here converges faster than for TPFA and MFEM, as we also saw in Section 5.3.

Table 5.5: Comparison of new well constants ξ_c to numerical well constant ξ_a.

(a) Square grid cells.

	TPFA	MFEM	MFDM
n	$\lvert\xi_a - \xi_c\rvert$	$\lvert\xi_a - \xi_c\rvert$	$\lvert\xi_a - \xi_c\rvert$
5	$1.7{\cdot}10^{-3}$	$2.1{\cdot}10^{-3}$	$7.6{\cdot}10^{-4}$
10	$7.2{\cdot}10^{-4}$	$8.7{\cdot}10^{-4}$	$5.4{\cdot}10^{-4}$
25	$4.2{\cdot}10^{-4}$	$4.6{\cdot}10^{-4}$	$4.8{\cdot}10^{-4}$
50	$3.8{\cdot}10^{-4}$	$4.0{\cdot}10^{-4}$	$4.7{\cdot}10^{-4}$
100	$3.7{\cdot}10^{-4}$	$3.8{\cdot}10^{-4}$	$4.7{\cdot}10^{-4}$
200	$3.7{\cdot}10^{-4}$	$3.8{\cdot}10^{-4}$	$4.6{\cdot}10^{-4}$

(b) Non-square grid cells.

		TPFA	MFEM	MFDM
β	m	$\lvert\xi_a - \xi_c\rvert$	$\lvert\xi_a - \xi_c\rvert$	$\lvert\xi_a - \xi_c\rvert$
2	5	$1.6{\cdot}10^{-3}$	$1.6{\cdot}10^{-3}$	$1.3{\cdot}10^{-4}$
2	10	$6.8{\cdot}10^{-4}$	$4.5{\cdot}10^{-4}$	$8.1{\cdot}10^{-5}$
2	25	$4.2{\cdot}10^{-4}$	$9.3{\cdot}10^{-5}$	$1.3{\cdot}10^{-4}$
4	5	$1.6{\cdot}10^{-3}$	$1.9{\cdot}10^{-3}$	$1.7{\cdot}10^{-4}$
4	10	$6.7{\cdot}10^{-4}$	$8.2{\cdot}10^{-4}$	$3.7{\cdot}10^{-4}$
4	25	$4.1{\cdot}10^{-4}$	$5.0{\cdot}10^{-4}$	$4.2{\cdot}10^{-4}$
8	5	$1.7{\cdot}10^{-3}$	$9.1{\cdot}10^{-4}$	$1.5{\cdot}10^{-4}$
8	10	$6.7{\cdot}10^{-4}$	$7.9{\cdot}10^{-5}$	$3.4{\cdot}10^{-4}$
8	25	$4.1{\cdot}10^{-4}$	$3.8{\cdot}10^{-4}$	$3.8{\cdot}10^{-4}$
16	5	$1.7{\cdot}10^{-3}$	$1.7{\cdot}10^{-3}$	$1.0{\cdot}10^{-4}$
16	10	$6.7{\cdot}10^{-4}$	$7.5{\cdot}10^{-4}$	$8.5{\cdot}10^{-5}$
16	25	$4.1{\cdot}10^{-4}$	$4.7{\cdot}10^{-4}$	$1.3{\cdot}10^{-4}$
32	5	$1.7{\cdot}10^{-3}$	$1.0{\cdot}10^{-3}$	$5.4{\cdot}10^{-4}$
32	10	$6.8{\cdot}10^{-4}$	$9.7{\cdot}10^{-5}$	$3.5{\cdot}10^{-4}$
32	25	$4.1{\cdot}10^{-4}$	$1.8{\cdot}10^{-4}$	$3.1{\cdot}10^{-4}$
64	5	$1.7{\cdot}10^{-3}$	$1.3{\cdot}10^{-3}$	$2.1{\cdot}10^{-4}$
64	10	$6.8{\cdot}10^{-4}$	$3.7{\cdot}10^{-4}$	$2.7{\cdot}10^{-5}$
64	25	$4.1{\cdot}10^{-4}$	$9.8{\cdot}10^{-5}$	$1.8{\cdot}10^{-5}$

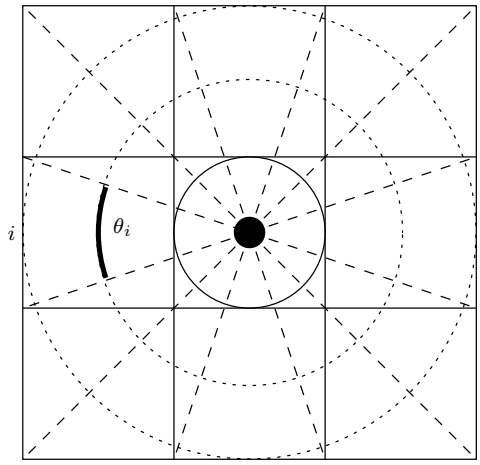

Figure 5.6: Section of infinite reservoir with well and radial flow.

The presented results verify that $r_{0,c}(\text{MFEM}, \beta)$ and $r_{0,c}(\text{MFDM}, \beta)$ are good approximations to the equivalent radius for MFEM and MFDM, respectively. We therefore expect that the new well models for MFEM and MFDM have the same performance as Peaceman's well model for TPFA. This hypothesis will be tested in Chapter 6.

5.6 Chapter Conclusions

We have developed expressions for the equivalent radius for MFEM and MFDM based on Peaceman's well model for TPFA. The accuracy of these equivalent radii has been verified by a simulation of radial flow from a well in an infinite reservoir. The attempts to develop a general expression for the equivalent radius for a family of mimetic inner products did not succeed. The results, however, indicate that there is a connection between the eigenvalues of mimetic inner product matrix $\mathbf{T}_E$ and the equivalent radius r_0. Until an expression for this relationship is found, r_0 must be calculated by the procedure in Section 5.3 for each inner product.

Chapter 6

Test of New Well Models

In this chapter we test the new well models developed in Chapter 5 on both homogeneous and heterogeneous reservoirs.

6.1 Presentation of New Well Models

We repeat the definition of the well index from (4.1),

$$\text{WI} = \frac{q}{p_0 - p_{wf}}. \tag{6.1}$$

The well index for radial near-well flow was given in (4.5) as

$$\text{WI} = \frac{2\pi kh}{\mu \ln(r_0/r_w)}, \tag{6.2}$$

where r_0 is the equivalent radius of the well-block. In the following we will refer to (6.2) as the radial-flow well model. In Chapter 4 we presented Peaceman's equivalent radius for TPFA that is given by

$$r_{0,p} = 0.14(\Delta x^2 + \Delta y^2)^{\frac{1}{2}}. \tag{6.3}$$

Further, in Chapter 5 we showed that Peaceman's approach for finding (6.3) could be extended to other numerical methods, and that the resulting equivalent radii were unique for the tested methods. The methods considered were the mixed FEM with RT_0-basis functions and the mimetic FDM defined by the inner product (3.80) with $\alpha = 1$. For easier notation, we will henceforth refer to these methods as MFEM and MFDM, respectively. However, it is important to note that the equivalent radii developed in Chapter 5 do not hold in general for the family of mixed FEMs or the family of mimetic FDMs, despite the notation. This is because the equivalent radii depend on the set of basis functions or inner product used, as shown in Section 5.4. The key result from Chapter 5 was: the equivalent radius for a numerical method

$M \in \{\text{TPFA, MFEM, MFDM}\}$ on a grid with aspect ratio $\beta = \Delta x/\Delta y$ is given by

$$r_{0,c}(M,\beta) = \xi(M,\beta)(\Delta x^2 + \Delta y^2)^{\frac{1}{2}}, \tag{6.4}$$

where $\xi(\text{MFEM},\beta)$ and $\xi(\text{MFDM},\beta)$ are given in Table 5.4, and $\xi(\text{TPFA},\beta) = 0.14$. Thus, we have three different well indices:

$$\text{Peaceman:} \quad \text{WI-P} = \frac{2\pi kh}{\mu \ln(r_{0,p}/r_w)}, \tag{6.5}$$

$$\text{MFEM:} \quad \text{WI-MFEM} = \frac{2\pi kh}{\mu \ln(r_{0,c}(\text{MFEM},\beta)/r_w)}, \tag{6.6}$$

$$\text{MFDM:} \quad \text{WI-MFDM} = \frac{2\pi kh}{\mu \ln(r_{0,c}(\text{MFDM},\beta)/r_w)}. \tag{6.7}$$

We will refer to these well indices as the correct well index for TPFA, MFEM, and MFDM, respectively (meaning the correct WI under the assumptions stated for near-well radial flow). The well index in (6.5) is developed for the TPFA, but the lack of research on well indices for other numerical methods (see Section 4.3) can lead people to believe that (6.5) can be used for other numerical methods. In this chapter we will test MFEM and MFDM with Peaceman's well index and with the specially adapted well indices (6.6) and (6.7), to see how important the well index is for the accuracy of the result. We also include a test of TPFA with Peaceman's well index for comparison. All tests will be done for both homogeneous and heterogeneous reservoirs. The different cases will be denoted MFEM_p, MFDM_p, and TPFA_p for the methods with Peaceman's well index, and MFEM_c and MFDM_c for the methods using the well indices in (6.6) and (6.7).

6.2 Setup for Numerical Simulations

6.2.1 Grid and reservoir data

The simulations are done by solving the prototype flow problem (3.2)–(3.4) on a regular Cartesian grid with grid size 60×220 cells. The non-square grids are made by stretching the grid in the x-direction: $\Delta x = \beta$, $\beta \in \{1, 3, 5, 9, 17\}$, while $\Delta y = 1$ for all grids. For all simulations we assume that the reservoir is isotropic. In the homogeneous case, unit permeability is used, while in the heterogeneous case we use an isotropic permeability field with 85 different layers. This permeability field is Dataset 2 from the 10th SPE Comparative Solution Project [14], a project whose purpose was to compare upgridding and upscaling approaches on a million cell geological model. The model is described as a regular Cartesian grid with grid size $60 \times 220 \times 85$ cells. We will simulate in 2D, meaning that we have 85 different 2D isotropic permeability layers with 60×220 cells. The model consists of part of a Brent sequence from the North Sea. The top 35 layers represent the Tarbert formation and is a representation of a near shore environment, while the

Table 6.1: Simulation data

Property	#Cells	β	Δx	Δy	r_w	q(inj)	p_{wf}(prod)
Value	60×220	$\{1, 3, 5, 9, (17)\}$	β	1	0.01	-1	0

lower 50 layers represent the Upper Ness formation and is fluvial. We will look at Layers 1–35 and 36-85 separately since they exhibit very different properties. The latter is highly heterogeneous with channel structures, while the former has more smooth variations in the permeability. An example from each group of layers illustrating these properties can be seen in Figure 6.1. By using these 85 layers for simulation, we can test the performance of the new well models under different permeability conditions.

The reservoir will be equipped with one production- and one injection well. We put $q = -1$ for the injection well, and set the well pressure for the production well to $p_{wf} = 0$. Note that q is defined as the production rate of the well, and q is therefore negative for the injection well. Moreover, these parameters are chosen out of mathematical convenience and do not attempt to model a realistic reservoir. However, the choice of parameter values is not important as we will only look at the pressure drop in the reservoir and assume incompressible flow. Furthermore, with p_{wf} specified for one well, the pressure in the reservoir is also uniquely determined, as discussed in Section 3.2. Lastly, we specify the placement of the wells according to two requirements. First of all, the wells must be placed a certain distance away from the boundaries to avoid boundary effects. Secondly, there must be sufficient distance between the wells to allow the flow to develop and to avoid interference between the wells. We saw in Chapter 4 that both these requirements are important for the performance of the radial-flow well model (6.2). A well placement that satisfies these requirements is to place the injection well in cell 2430 and the production well in cell 10830. This placement will be used for all simulations. Thus, for the heterogeneous case, this setup gives many different cases: one or both wells might lie in a high permeable area for some layers, while for others layers one or both wells lie in a low permeable area. Further, for the fluvial layers, we will have high permeable channels connecting the wells for some layers and for other layers there will be no such connections. The degree of heterogeneity around the wells will also vary. The purpose of this setup is to generate a "random" set of different cases for simulation that will give a picture of the overall performance of the new well indices and identify problem cases. The resulting linear system for the flow and pressure in the reservoir, (3.91), is solved by the mimetic simulator described in Section 5.1, with the respective inner products of TPFA, MFEM and MFDM. An overview of the simulation data is presented in Table 6.1.

6.2.2 Reference solution

To test the results obtained with different well indices, we compare the results to a reference solution. The reference solution for grids with square cells is obtained

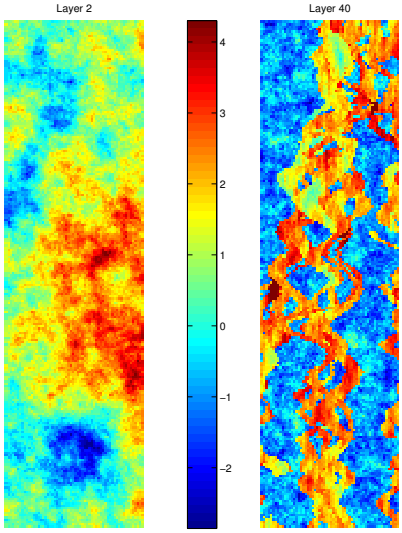

Figure 6.1: Example of permeability for Layer 2 and Layer 40, shown with a logarithmic color scale.

by solving the system on a grid that has double resolution compared to the original grid and is radial around the well, see Figure 6.2. This method allows us to compute the pressure at well radius, p_{wf}, directly. The numerical method used is the mimetic FDM defined by the inner product (3.80) with $\alpha = 2$. The resulting method is equal to mixed FEM with RT_0-basis-functions on Cartesian grids and is chosen because it converges on radial grids. We remark that this property is not shared by all the methods discussed in this thesis. For instance, the TPFA method will not converge on a radial grid unless it is specially implemented to handle this type of grid.

The reference solution for grids with non-square cells is computed by first refining the grid in the x-direction to obtain a grid with square grid cells. Then we use the same technique as described above to make a radial grid around the well. The result is a grid of approximate size $120\beta \times 440$ cells. This setup causes memory problems for $\beta > 9$ on heterogeneous permeability, thus limiting how high aspect ratios we can obtain reference solutions for. Another remark is that the grid refinement and the insertion of a radial grid requires the aspect ratio to be an odd number. This is because the well-block is refined to a row of β cells in the x-direction. The new well-block must be the middle cell of the row to maintain the coordinates of the well, meaning that the row must have an odd number of cells. Normally we would use $\beta = \{1, 2, 4, 8, \dots\}$, successively doubling Δx, but here we instead use $\beta = \{1, 3, 5, 9, \dots\}$ due to the requirement of odd numbered ratios .

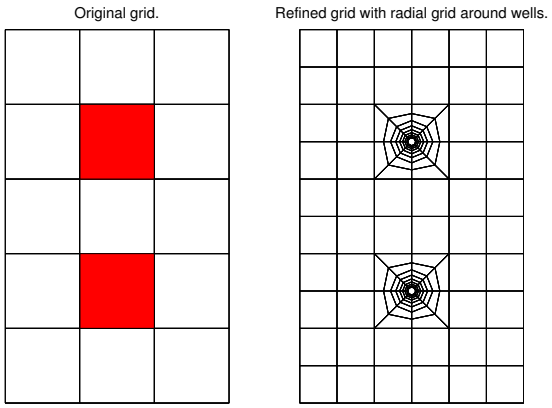

Figure 6.2: Original grid with colored well-blocks (right), and refined near-well radial grid (left).

6.2.3 Measurement of the error

Since the simulations are in 2D, the well indices (6.5)–(6.7) can be simplified by letting $h = 1$. In order to evaluate the results from the simulations, we must consider errors from the well index for both wells. Therefore we look at the pressure drop between the wells, defined as

$$\Delta p = |p_{wf,1} - p_{wf,2}|. \tag{6.8}$$

We now make a stepwise analysis of the linear system (3.91), focusing on the pressure, to explain how the well index influences the pressure drop of the system. Let $i = 1$ be the injection well and $i = 2$ be the production well. We begin by noticing that

$$\text{WI-MFEM} < \text{WI-MFDM} < \text{WI-P}. \tag{6.9}$$

In Section 3.6 we saw that the wells are implemented as boundary conditions in the linear system, and that the equation

$$\text{WI}^{-1} q_i - p_{0,i} + p_{wf,i} = 0 \tag{6.10}$$

is inserted in the linear system for each well i. We start by identifying the known quantities. As mentioned earlier $q_1 = -1$ and $p_{wf,2} = 0$. In addition, we know that $q_2 = -q_1 = 1$ since there are only two wells and the numerical methods are conservative for flux. Further, the pressure in the production well-block is computed from (6.10). Since $p_{wf,2} = 0$, we get that $p_{0,2}$ is inverse proportional to WI, meaning that a high WI gives a low $p_{0,2}$ and vice versa. For MFEM and MFDM,

Peaceman's WI is too high compared to the correct value and will therefore compute a too low pressure value for $p_{0,2}$. The global pressure field depends on the value of $p_{0,2}$, and $p_{0,1}$ will therefore also depend on $p_{0,2}$. If $p_{0,2}$ is too low, $p_{0,1}$ will also be too low compared to the correct value. An important remark is that the pressure drop between the well-blocks, $\Delta p_0 = p_{0,1} - p_{0,2}$, is constant for a numerical method on a given grid regardless of the well index. The pressure $p_{wf,1}$ in well 1 is computed from (6.10) using $p_{0,1}$ and q_1. Again we see that a high WI gives a low $p_{wf,1}$. This means that MFEM and MFDM with Peaceman's WI will compute a too low $p_{wf,1}$ using the already too low value of $p_{0,1}$, which magnifies the error. Lastly, observe that the pressure drop $\Delta p = p_{wf,1}$ since $p_{wf,2} = 0$. In conclusion, we have seen that using a WI that is too high compared to the correct value gives a pressure drop that is too low compared to the correct value. Consequently, using Peaceman's WI for MFEM and MFDM results in a too low pressure drop Δp.

It can be hard to isolate the error caused by the well index from the errors in the numerical method. We therefore give an analytical expression for the absolute error in Δp from using WI-P instead of the correct well index WI-C for a given method. From the discussion above, we have that q_1, q_2, and $p_{wf,2}$ are known and that Δp_0 is constant. First, observe that the error $E(p_{0,2})$ in the computation of the pressure $p_{0,2}$ in well-block 2 is given by

$$\begin{aligned} E(p_{0,2}) &= p_{0,2,c} - p_{0,2,p} && (6.11)\\ &= p_{wf,2} + \frac{q_2}{\text{WI-C}} - p_{wf,2} - \frac{q_2}{\text{WI-P}} && (6.12)\\ &= \frac{q_2}{2\pi k_2}\ln(\frac{r_{0,c}}{r_{0,p}}) && (6.13)\\ &= \frac{q_2}{2\pi k_2}\ln(\frac{\xi_c}{\xi_p}). && (6.14) \end{aligned}$$

Second, we have that the pressure in well-block 1 is given by

$$p_{0,1} = \Delta p_0 + p_{0,2}. \tag{6.15}$$

The absolute error in Δp from using using WI-P instead of the correct well index WI-C is now given by

$$\begin{aligned} E(\Delta p) &= |(p_{wf,1,c} - p_{wf,2,c}) - (p_{wf,1,p} - p_{wf,2,p})|\\ &= |(p_{0,1,c} - \frac{q_1}{\text{WI-C}}) - (p_{0,1,p} - \frac{q_1}{\text{WI-P}})|\\ &= |(p_{0,1,c} - p_{0,1,p}) - \frac{q_1}{2\pi k_1}\ln(\frac{r_{0,c}}{r_{0,p}})|\\ &= |(\Delta p_0 + p_{0,2,c} - \Delta p_0 - p_{0,2,p}) - \frac{q_1}{2\pi k_1}\ln(\frac{\xi_c}{\xi_p})|\\ &= |\frac{q_2}{2\pi k_2}\ln(\frac{\xi_c}{\xi_p}) - \frac{q_1}{2\pi k_1}\ln(\frac{\xi_c}{\xi_p})|\\ &= \frac{1}{2\pi}\big(\frac{1}{k_2} + \frac{1}{k_1}\big)|\ln(\frac{\xi_c}{\xi_p})|, && (6.16) \end{aligned}$$

Table 6.2: Relative errors in Δp for different ratios, $r_w = 0.01$.

	TPFA	MFEM		MFDM	
β	WI-P	WI-MFEM	WI-P	WI-MFDM	WI-P
1	0.0037	0.0036	0.0553	0.0037	0.0290
3	0.0050	0.0049	0.0645	0.0046	0.0337
5	0.0051	0.0050	0.0599	0.0047	0.0312
9	0.0051	0.0050	0.0540	0.0047	0.0281
17	0.0049	0.0051	0.0497	0.0047	0.0258

where we have used that $q_1 = -q_2 = -1$. Observe that the absolute error is independent of the well radius.

The absolute error in Δp is constant for a given numerical method on a given grid. Thus, it does not give us much information about how well the method and the well index perform together. To test the performance we must therefore compare the pressure drop from the simulations against the pressure drop of the reference solution, Δp_{ref}. We define the absolute error in Δp for a method B as

$$e_a(B) = |\Delta p_{\text{ref}} - \Delta p_B|. \tag{6.17}$$

In the heterogeneous case, we can get great variations in Δp for the different layers, and to be able to compare the errors in the different layers we must look at the relative error in the pressure drop. The relative error in Δp for a method B is defined as

$$e_r(B) = \frac{|\Delta p_{\text{ref}} - \Delta p_B|}{\Delta p_{\text{ref}}}. \tag{6.18}$$

We will henceforth refer to $e_r(B)$ as the relative error (in Δp) for method B. Note that the relative error depends on the well radius. Small r_w results in that a large amount of the pressure drop happens in the near-well areas where the assumption of radial flow is correct. The radial-flow well model is therefore more correct for a smaller r_w. We use $r_w = 0.01$ in the simulations, but we also show an example with $r_w = 0.1$ for homogeneous grids.

6.3 Results for Homogeneous Reservoir

We start with simulations on homogeneous reservoirs. In this case, all the assumptions for the radial-flow well model are satisfied. We show results for $r_w = 0.01$ and also include results for $r_w = 0.1$ for comparison. The relative errors in Δp for the different methods and the different ratios with $r_w = 0.01$ are shown in Table 6.2. The results show that it is a big improvement to use the correct well index for MFEM and MFDM instead of Peaceman's well index. Another observation is that the relative errors do not increase notably as the ratio increases, which means that we can expect results in the same range for higher ratios. However, we could not make reference solutions for higher ratios than 17 due to lack of memory.

Table 6.3: Relative errors in Δp for different ratios, $r_w = 0.1$.

	TPFA	MFEM		MFDM	
β	WI-P	WI-MFEM	WI-P	WI-MFDM	WI-P
1	0.0047	0.0047	0.0663	0.0047	0.0350
3	0.0069	0.0067	0.0831	0.0064	0.0436
5	0.0072	0.0070	0.0780	0.0067	0.0409
9	0.0072	0.0070	0.0706	0.0067	0.0370
17	0.0070	0.0072	0.0650	0.0066	0.0340

Moreover, the table shows that the relative errors for the methods with correct well index, in column 1, 2, and 4, are almost equal. This is not surprising as the correct well indices have been developed by the same procedure, and since TPFA, MFEM, and MFDM all converge to the same solution on a Cartesian $\mathbf{K}$-orthogonal grid with homogeneous permeability. The relative errors for the methods with correct WI can come from errors in the well model and errors from using a coarser grid in the simulations than in the reference solution.

The results for $r_w = 0.1$ in Table 6.3 give the same conclusions as stated above: the specially adapted well indices have the best performance. Moreover, we observe that the relative errors for $r_w = 0.1$ are smaller than the relative errors for $r_w = 0.01$, as expected.

We conclude that the new well indices (6.6) and (6.7) for MFEM and MFDM perform as well as Peaceman's well index for TPFA for homogeneous permeability.

6.4 Results for Heterogeneous Reservoir

One of the main assumptions for the radial-flow well model given in (6.2) is that the reservoir is homogeneous. We now consider heterogeneous reservoirs, but (6.2) is still valid (to a certain extent) if the flow in the near-well area is radial and k denotes the permeability of the well-block. A relevant factor in this assumption is the size of the near-well area. One possible definition of the near-well area is based on the reasoning that there must be radial flow within the equivalent radius if (6.2) is to be correct. In this case, the near-well area must at least include the cells within the equivalent radius. This definition is grid dependent since the equivalent radius increases for increasing Δx and Δy. Using a grid dependent definition is problematic since the near-well area is a physical area. Due to this problem we will not attempt to define the near-well area here. Instead we define the *dependence area* as the area where the assumption of radial flow must be satisfied in order for the well model in (6.2) to be correct. We remark that square cells are better suited for modeling radial flow than non-square cells, so non-square grids will have a larger dependence area than square grids.

We expect the relative error for a method with wrong WI to be larger if one or both wells lie in a highly heterogeneous area. This is because the assumption of

Table 6.4: Statistics for relative error for square grid cells.

(a) Layers 1–35 (Tarbert)

Method	mean	max	std
TPFA_p	0.019	0.045	0.012
MFEM_c	0.005	0.013	0.004
MFEM_p	0.080	0.150	0.038
MFDM_c	0.013	0.029	0.008
MFDM_p	0.034	0.091	0.024

(b) Layers 36–85 (Upper Ness)

Method	mean	max	std
TPFA_p	0.040	0.115	0.029
MFEM_c	0.014	0.038	0.009
MFEM_p	0.104	0.196	0.061
MFDM_c	0.028	0.080	0.020
MFDM_p	0.060	0.129	0.033

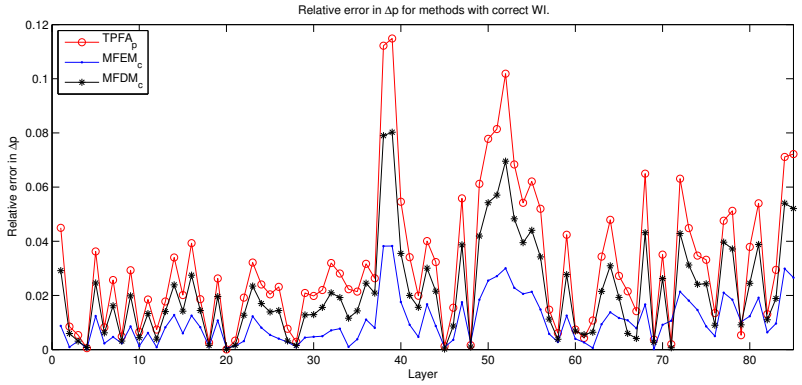

Figure 6.3: Relative error in Δp for the methods with "correct" well indices.

radial flow is less valid in such cases.

6.4.1 Results for square grids

Table 6.4 shows statistics of the relative error for square grids. The results for TPFA_p are included for comparison. We see that the mean relative errors for MFEM_c and MFDM_c are much smaller than the mean relative errors for MFEM_p and MFDM_p, for both Layers 1–35 and Layers 36–85. Moreover, MFDM_c and MFDM_p are closer than MFEM_c and MFEM_p. This is because

$$r_{0,p} < r_{0,c}(\text{MFDM}) < r_{0,c}(\text{MFEM}).$$

The error from using Peaceman's WI will therefore be smaller for MFDM than for MFEM. Furthermore, the relative errors are smaller for Layers 1–35 than for Layers 36–85 for all methods. This is not surprising as the permeability variations are higher in the fluvial layers. Therefore, the assumption of radial flow in the near-well area is more correct in Layers 1–35 than in Layers 36–85, resulting in larger errors in Layers 36–85. Figure 6.3 shows a plot of the relative error in Δp for the methods with correct well indices. It is easy to see that MFEM has the smallest

relative error and that TPFA has the largest relative error. This might be because the numerical method used in the reference solution is equivalent to MFEM on Cartesian grids and that it is closer to MFDM than to TPFA. We can also see in the Figure 6.3 that the graphs for the different methods follow each other for almost all layers. The exception is Layer 71 where the graphs for TPFA and MFDM do not follow the graph for MFEM. This is a layer where radial near-well flow is prevented because of large permeability variations in the near-well areas, which means that the assumptions for the radial-flow well model are not satisfied. If we ignore Layer 71, it should suffice to consider one of the numerical methods when we investigate why some layers give large relative errors while others give small relative errors. To eliminate possible errors from the choice of method in the reference solution, we chose MFEM for the analysis of the relative error for the different layers.

Analysis of results for MFEM

Figure 6.4(a) shows a scatter plot of Δp_{ref} against Δp_c and Δp_p. It is clear from the plot that WI-MFEM is better than Peaceman's WI-P for MFEM. Moreover, the absolute error from using Peaceman's well index increases with the pressure drop. If the pressure drop in the reservoir is high, then this implies a high pressure drop within the well-block. High pressure drop in the well-block in turn implies large error from using wrong well index, as seen in the figure. It is however more informative to look at the error relative to the pressure drop. Large relative errors for methods with wrong well index are found in cases where a high percentage of the pressure drop happens inside the well-block. Figure 6.4(b) shows a plot of the relative error for MFEM with WI-MFEM and for MFEM with WI-P. As before we see that it is a big improvement to use the specially adapted well index for MFEM instead of Peaceman's well index. The largest relative errors for MFEM$_p$ are found in Layers 40, 64, 72, and 73. The common feature of these layers is that the permeability in one of the well-blocks is low. Consequently, a high percentage of the pressure drop will happen in the well-block.

There are some outliers in the relative error for MFEM$_c$, the most dominant being Layers 38 and 39. It is hard to say whether the errors come from the difference in grid resolution between the simulation and the reference solution or from the well model. This is because the relative errors for MFEM with the correct well index are in overall small. We will consider this problem in the following section.

6.4.2 Results for square refined grid

To rule out errors from the reference solution, we computed a new reference solution on a grid of four times the resolution of the original simulation grid, thus twice the resolution of the original reference solution grid. The relative error between the two reference solutions is plotted in Figure 6.5. We see that the relative error between the reference solutions is of the same magnitude as the relative error in MFEM$_c$. This means that the relative error for MFEM$_c$ is mainly caused by the use

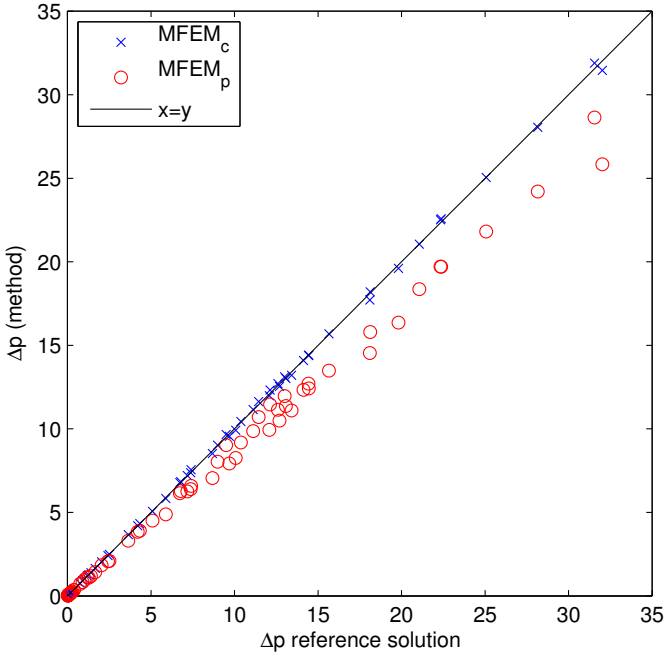

(a) Scatter plot of Δp with the two largest pressure drops removed

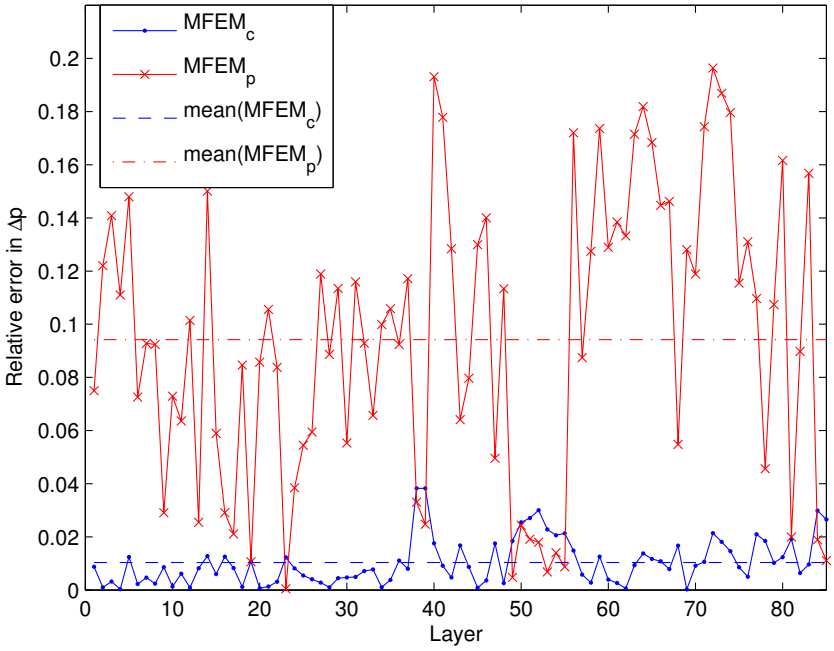

(b) Relative error in Δp for MFEM with correct WI and with Peaceman's well index. The mean values are taken over all layers.

Figure 6.4: Plots of relative error for MFEM.

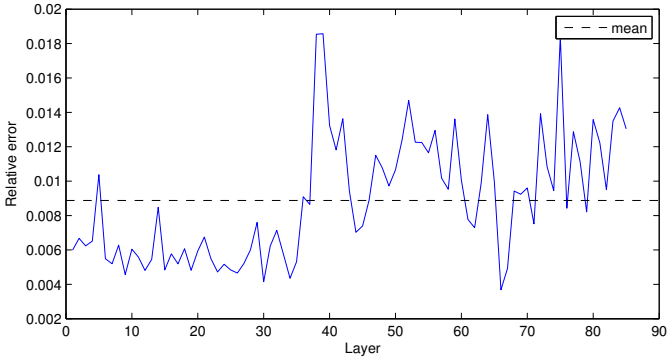

Figure 6.5: Relative error between the original reference solution and the refined reference solution.

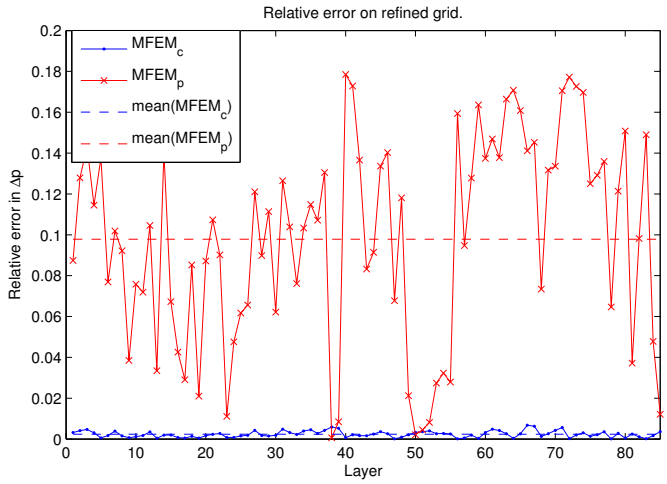

Figure 6.6: Relative error in Δp between the refined simulation and the refined reference solution.

Table 6.5: Statistics for relative error between the refined simulation and the refined reference solution.

(a) Layers 1–35 (Tarbert)

Method	mean	max	std
TPFA$_p$	0.003	0.011	0.002
MFEM$_c$	0.002	0.005	0.001
MFEM$_p$	0.085	0.143	0.035
MFDM$_c$	0.002	0.006	0.001
MFDM$_p$	0.041	0.074	0.019

(b) Layers 36–85 (Upper Ness)

Method	mean	max	std
TPFA$_p$	0.009	0.026	0.007
MFEM$_c$	0.003	0.007	0.002
MFEM$_p$	0.107	0.179	0.057
MFDM$_c$	0.006	0.017	0.004
MFDM$_p$	0.053	0.095	0.030

of a coarser grid in the simulation than in the reference solution. From the figure we may also conclude that the original reference solution is sufficiently converged. However, we observe that the relative errors for the already mentioned Layers 38 and 39 are large compared to the mean, which means that a grid-refinement causes large changes in the solution for these layers. This finding indicates that the large relative errors for MFEM$_c$ (and MFDM$_c$ and TPFA$_p$) for these layers stem from using a coarser grid in the simulation than in the reference solution. It is therefore interesting to examine the effect of refining the simulation grid as well. We repeated the simulation for square grids on a grid of three times the resolution of the original simulation grid. The results for the relative error between the refined case and the refined reference solution are shown in Figure 6.6 and in Table 6.5. We see that the relative errors for the correct well indices are smaller than on the original grid, and that the relative errors for the wrong well indices are roughly the same. There are no longer any outliers in the relative error for the methods with correct well indices. This is reflected in the large reduction of the standard deviations for the correct well indices in Table 6.5 compared to the results for the original grid in Table 6.4. The improved results are due to two factors. First, the part of the relative error coming from the difference in grid resolution is almost eliminated. Secondly, the assumption of near-well radial flow is more valid with higher resolution around the well.

One relevant question here is: why not use the refined reference solution for the tests in Section 6.4.1 instead of the original reference solution? The answer is that a finer reference solution would only increase the part of the error coming from the difference in grid resolution. Thus, it would be harder to recognize the part of the error coming from the well model, which is the part of the error that we want to measure. The results for the original simulations compared against the refined reference solution show that the relative error for the correct well models increases with approx. 0.005, while the relative error for the wrong well models decreases with approx. 0.005. This is due to the fact that the pressure drop is lower in the refined than in the original reference solution for all layers. Regardless of which reference solution is used: all conclusions in Section 6.4.1 remain the same.

6.4.3 Results for non-square grids

Table 6.6 displays statistics for Layers 1–35. We see that the relative error increases as β increases for all methods and well indices. Moreover, MFEM$_c$ is better than MFEM$_p$ for all β, while MFDM$_c$ is worse than MFDM$_p$ for $\beta = 9$. Table 6.7 displays statistics for Layers 36–85. Here we also see that the relative error increases as β increases. The methods with correct well indices are better than MFEM$_p$ and MFDM$_p$ for $\beta = 3$, but worse for $\beta = 5, 9$. Both tables indicate that a higher well index (remember WI-P $>$ WI-MFDM $>$ WI-MFEM) gives less mean relative error for high β. This is also seen in the scatter plots of the pressure drop for MFEM against the reference solution in Figure 6.7. We see that the results for WI-P is under the line $x = y$ for $\beta = 3$, closer to $x = y$ for $\beta = 5$, and on both sides

Table 6.6: Statistics for relative error for Layers 1–35, non-square grid cells.

(a) $\beta = 3$.

Method	mean	max	std
TPFA$_p$	0.014	0.036	0.010
MFEM$_c$	0.012	0.040	0.009
MFEM$_p$	0.066	0.112	0.027
MFDM$_c$	0.011	0.024	0.007
MFDM$_p$	0.029	0.059	0.017

(b) $\beta = 5$.

Method	mean	max	std
TPFA$_p$	0.022	0.042	0.012
MFEM$_c$	0.025	0.084	0.019
MFEM$_p$	0.055	0.113	0.030
MFDM$_c$	0.021	0.062	0.014
MFDM$_p$	0.026	0.073	0.021

(c) $\beta = 9$.

Method	mean	max	std
TPFA$_p$	0.036	0.097	0.025
MFEM$_c$	0.044	0.142	0.033
MFEM$_p$	0.050	0.131	0.036
MFDM$_c$	0.038	0.118	0.028
MFDM$_p$	0.037	0.102	0.026

of $x = y$ for $\beta = 9$. This means that WI-P consequently underestimates Δp for $\beta = 3$ and improves the estimation for $\beta = 5$ before it gets worse again for $\beta = 9$.

The plots of the relative error for MFEM$_c$ and MFEM$_p$ in Figure 6.7 show that the relative error varies a lot for the different layers. Some of the maxima for MFEM$_c$ can be characterized as outliers in the data because they are far away from the mean. Observe that the number of outliers and the magnitude of the outliers for MFEM$_c$ both increase with β. These outliers increase the mean relative error for MFEM$_c$ greatly, and the result is that for $\beta = 9$:

$$\text{mean}\big(e_r(\text{MFEM}_c)\big) > \text{mean}\big(e_r(\text{MFEM}_p)\big).$$

We also see that the relative error for MFEM$_p$ has local minima for some layers where MFEM$_c$ has local maxima. That is, the wrong well index has significantly better performance than the correct well index for some layers. This behavior is found in layers where the near-well radial flow assumption is violated and will be further explained below.

The relative error increases with β because the assumptions of radial flow in the heterogeneous near-well area becomes less valid as β increases. Note that the relative error is composed of two quantities:

$$e_r = |e_w + e_g|, \tag{6.19}$$

where e_w is the error in the well index and e_g is the error from the difference in grid resolution. In the simulation grid, the dependence area will include more cells as the aspect ratio of the well-block increases. For high aspect ratios, this means

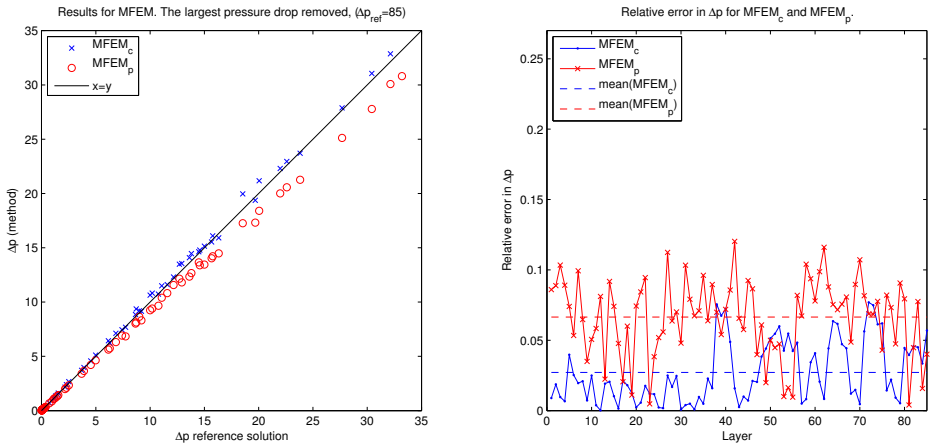

(a) Results for $\beta = 3$

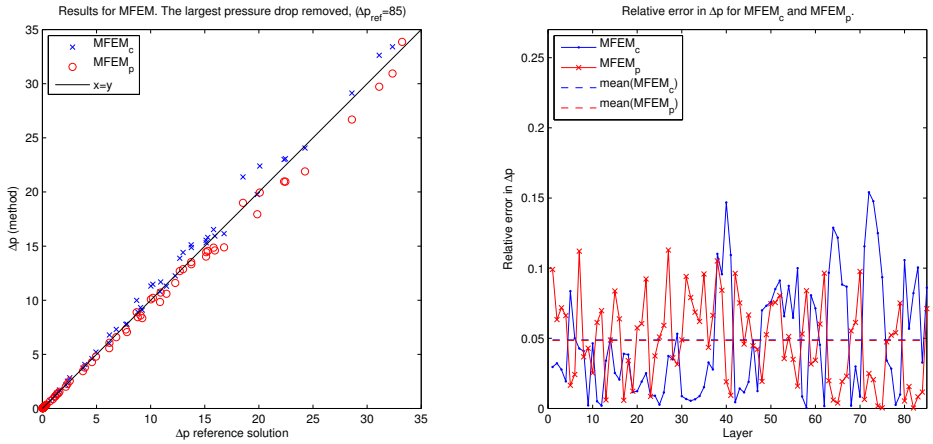

(b) Results for $\beta = 5$

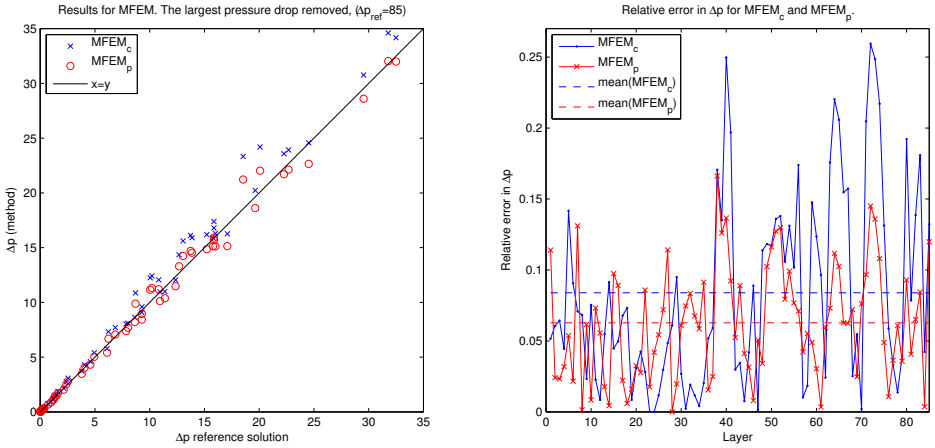

(c) Results for $\beta = 9$

Figure 6.7: Scatter plot of Δp and plot of relative error for MFEM, $\beta = 3, 5, 9$. The mean values in the figures are taken over all layers.

Table 6.7: Statistics for relative error for Layers 36–85, non-square grid cells.

(a) $\beta = 3$

Method	mean	max	std
TPFA$_p$	0.041	0.175	0.049
MFEM$_c$	0.037	0.077	0.022
MFEM$_p$	0.067	0.120	0.028
MFDM$_c$	0.038	0.130	0.033
MFDM$_p$	0.045	0.127	0.029

(b) $\beta = 5$.

Method	mean	max	std
TPFA$_p$	0.066	0.235	0.061
MFEM$_c$	0.066	0.154	0.044
MFEM$_p$	0.044	0.105	0.030
MFDM$_c$	0.066	0.178	0.046
MFDM$_p$	0.046	0.176	0.046

(c) $\beta = 9$.

Method	mean	max	std
TPFA$_p$	0.108	0.330	0.088
MFEM$_c$	0.112	0.259	0.074
MFEM$_p$	0.072	0.166	0.041
MFDM$_c$	0.110	0.258	0.075
MFDM$_p$	0.088	0.256	0.067

that we must assume radial flow not only in the well-block, but also in parts of the neighboring cells. Therefore, the validity of the well model will depend greatly on the permeability conditions in the increasing dependence area.

The grid in the reference solution, on the other hand, will not have an increasing dependence area because the grid cells here are square. As a result, e_g in (6.19) increases with β. When we compare the results for two different well indices for one numerical method, we get that e_g is the same in both. However, this does not guarantee that the relative errors are comparable, since e_w might have different signs for the two different well models that can contribute to either cancellation or amplification of the relative error. Thus, we get that the wrong well index in some cases performs better than the correct well index on layers with highly heterogeneous near-well areas.

This property is seen in Figure 6.8(a), which displays results for MFEM when $\beta = 9$. The figure shows the permeability in the cells near the wells for Layers 40, 64, and 72. In these layers, the relative error of the correct WI has local maxima, while the relative error for the wrong WI is small, so

$$\text{diff}(c, p) = e_r(\text{MFEM}_c) - e_r(\text{MFEM}_p)$$

is large. For all layers we see that the near-well area is highly heterogeneous for one or both wells. Peaceman's WI gives better results than WI-MFEM for these layers because the error from using the wrong WI partially cancels the error from violating the assumption of radial flow. Figure 6.8(b) shows Layers 31, 34, and 70, where the situation is the opposite of the above. In these layers, the relative error of the wrong WI has local maxima, while the relative error for the correct WI is

small, so

$$\text{diff}(p, c) = e_r(\text{MFEM}_p) - e_r(\text{MFEM}_c)$$

is large. We see that the near-well areas are more homogeneous in this case, so the radial flow assumption will be satisfied. As a result, the correct well index performs well. We notice that Layer 70 has some heterogeneity around well number 1, but the relative error is still small. This indicates that some heterogeneity near the well is tolerable as long as the neighboring cells of the well-block have little variation in the permeability. The permeability variations in Layers 1–35 are more smooth than in Layers 36–85, and this explains why the mean relative error is smaller for the former. When the near-well flow is not radially symmetric, MFEM_c will overestimate Δp, while MFEM_p, which usually underestimates Δp (see Figure 6.4(a)), might make a better estimate on Δp.

Summed up, we see that the results for $\beta = 3$ show a significant improvement for using the specially adapted well indices for MFEM and MFDM instead of Peaceman's well index. The corresponding results for $\beta = 5$ show improvement for Layers 1–35, where the near-well areas have less variation in the permeability. However, we have seen that Peaceman's well index performs better than WI-MFEM and WI-MFDM for MFEM and MFDM, respectively, for the highly heterogeneous permeability fields in Layer 36–85. For the highest aspect ratio tested, $\beta = 9$, there are large errors for all methods and all well indices, but Peaceman's well index has best the overall performance for all the methods. It is worth noticing that the relative error for all the correct well indices are approximately the same.

Peaceman's WI gives smaller mean relative errors than the specially adapted well indices for MFEM and MFDM on grids with high aspect ratios. Despite this, it would not be a good solution to use Peaceman's well index for MFEM and MFDM in these cases. This is because the mean relative errors for all methods are large, thus indicating that the assumptions for the radial-flow well model are not sufficiently satisfied for heterogeneous non-square grids with high aspect ratios. A solution to this problem could be to refine the grid near the wells. We will try this in the next section.

6.4.4 Results for non-square grids with refined well-block column

In the previous section, we saw that high aspect ratios and highly heterogeneous permeability around the wells gave large errors for the radial-flow well model. We will now test the well indices again on a grid that is refined around the well. The new grid is made by refining the cells in the column of the grid containing the well-blocks.

Local grid refinement is a common tool in well modeling and it is known to improve the accuracy under certain conditions. We therefore expect that a refinement will increase the performance of the new well indices for MFEM and MFDM. The increased grid resolution improves the accuracy of the numerical methods near the

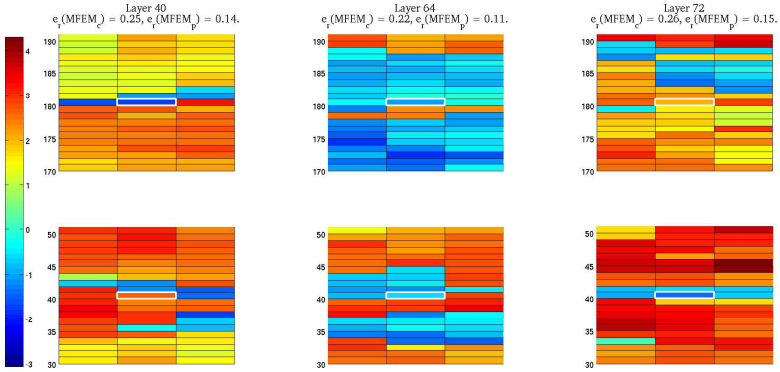

(a) $e_r(\text{MFEM}_c) >> e_r(\text{MFEM}_p)$

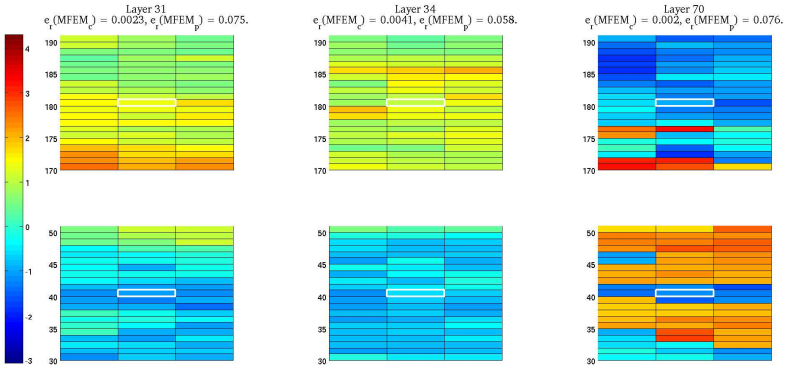

(b) $e_r(\text{MFEM}_c) << e_r(\text{MFEM}_p)$

Figure 6.8: Permeability in the near-well areas for layers where $e_r(\text{MFEM}_c)$ is large compared to $e_r(\text{MFEM}_p)$ (a), and where $e_r(\text{MFEM}_p)$ is large compared to $e_r(\text{MFEM}_c)$ (b). The color of a cell indicates the permeability, and the well-block is marked with white edges.

Figure 6.9: Refinement of the column of the grid containing a well-block. The well-block is colored.

Table 6.8: Mean value of the relative error for different grid refinements, $\beta = 9$.

(a) Layers 1–35.

Method	Unrefined	Refine$_1$	Refine$_2$
TPFA$_p$	0.036	0.083	0.015
MFEM$_c$	0.044	0.038	0.006
MFEM$_p$	0.050	0.051	0.085
MFDM$_c$	0.038	0.063	0.010
MFDM$_p$	0.037	0.022	0.036

(b) Layers 36–85.

Method	Unrefined	Refine$_1$	Refine$_2$
TPFA$_p$	0.108	0.122	0.065
MFEM$_c$	0.112	0.062	0.034
MFEM$_p$	0.072	0.087	0.115
MFDM$_c$	0.110	0.095	0.051
MFDM$_p$	0.088	0.068	0.081

well. Additionally, by refining all cells in the column of the grid containing the well-blocks, we increase the resolution of the grid between the wells, which also improves the accuracy of the numerical methods. This is however not an important factor, as the gain from refining is largest in the near-well area. The ideal setup would be to only increase the resolution of the grid near the wells, because this would improve the speed and separate the two sources of improved accuracy in the numerical methods. However, this setup requires a more difficult implementation than the one considered here and is beyond the scope of this thesis.

The tests are done for $\beta = 9$, because this is the first ratio where MFEM$_c$ and MFDM$_c$ performed worse than MFEM$_p$ and MFDM$_p$ for both Layers 1–35 and Layers 36–85. We will use two different grid refinements:

- **Refine**$_1$: split all cells in the column containing the well-blocks into three cells; two non-square cells of size 4×1 and one square cell in the middle of size 1×1.
- **Refine**$_2$: split all cells in the column of the grid containing the well-block into nine square cells of size 1×1.

An illustration of the refinements are shown on a section of the grid in Figure 6.9. Note that the permeability in a row of refined cells is the same as the permeability of the original cell. We expect that Refine$_2$ gives the best results, but it is interesting to have two cases for comparison. The new well-block will in both cases be square, which corresponds to using the well constant for $\beta = 1$. We remark that the radial-flow well model is derived under the assumption of a uniform grid. This assumption is probably sufficiently satisfied if the cells in the near-well area are of

uniform size. Refine$_1$ creates a non-uniform grid in the near-well area and might therefore lead to inaccurate results.

The results from the simulations are shown in Table 6.8, and plots for MFEM are shown in Figure 6.10. We see that Refine$_1$ increases the mean relative error for TPFA$_p$ for both groups of layers. Moreover, the results for MFDM$_c$ show increased relative error with Refine$_1$ for Layers 1–35, but the results are better than the original for Layers 36–85. The results for MFEM$_c$ with Refine$_1$ are better than the original for both groups of layers. Figure 6.10(a) displays the relative error for MFEM$_c$ on both the original grid and the Refine$_1$-grid. We see that almost all outliers are removed with Refine$_1$, but that the relative error is increased for some layers. Furthermore, Figure 6.11(a) shows that Refine$_1$ increases the relative error for TPFA$_p$ in almost all layers, so the mean relative error is increased even though the relative errors of a few large outliers are reduced.

The poor results are probably due to the fact that Refine$_1$ creates a non-uniform grid in the near-well area and therefore violates one assumption in the radial-flow well model. Overall, the performance of Refine$_1$ is far from satisfactory, even though the results for some layers are good. We cannot apply a refinement that in general gives worse performance than in the unrefined case. Thus, we conclude that a non-uniform refinement of the near-well area should not be used together with the radial-flow well model. In addition we remark that the results indicate that TPFA is more sensitive to this requirement than MFEM.

The results for Refine$_2$, which is a uniform refinement, are much better. Here we see big improvements for all the methods with correct well indices. The performance of the correct well indices are improved for almost all layers, and nearly all outliers in the relative error are removed, as seen for MFEM$_c$ in Figure 6.10(b) and TPFA$_p$ in Figure 6.11(b). Moreover, the results for Layers 1–35 with Refine$_2$ in Table 6.8(a) are as good as the results obtained for square grids in Table 6.4(a). The mean relative errors for MFEM$_c$ and MFDM$_c$ are less than half compared to the original results, hence a major improvement. We notice that there are some remaining outliers in Layers 36–85, but the results are overall very good.

We now analyze the layers that were outliers in the original simulation. The question is whether there are common features within the layers where the results are:

1. improved by Refine$_2$,

2. not improved by Refine$_2$.

The layers in question are the same for all methods with correct well indices, meaning that these outliers exhibit the same behavior under the refinement for all of TPFA$_p$, MFEM$_c$, and MFDM$_c$.

We start with the outliers that are improved by the refinement. The most significant improvements are found in Layers 40, 64, 72, 73, and 74. These layers are recognized by a high pressure drop and that one of the well-blocks lie in a low permeable area. Consequently, a high percentage of the pressure drop happens near

this well. It is in general hard for a numerical method to accurately approximate large variation when the resolution of the grid is low. A high pressure drop therefore increases the error in the pressure approximation in the numerical methods. When we increase the resolution around a well with Refine$_2$, we also increase the accuracy of the well-block pressure, which in turn reduces the relative error in Δp. To illustrate the improvements of the refinement, we show figures of the pressure and flux near the wells for Layer 64. The unrefined case is shown in Figure 6.12(a) and the case with the Refine$_2$-grid is shown in Figure 6.12(b). We see that the refined pressure solution in the near-well areas are notably different from the pressure in the unrefined grid, and that Δp decreases from 12.3 in the unrefined case to 9.9 in the refined case.

The largest outliers with no or little improvement are Layers 38, 39, 51, 52, and 85. Two common features of these layers are a low pressure drop and that both well-blocks lie in high permeable cells. For all layers, except Layer 51, we also find that one of the wells-blocks has one or several low permeable cells as neighbors, mainly in the y-direction. These low permeable neighbors prevent radial flow from the well, and so the assumption of radial flow in the well model is not satisfied. Increased resolution in the well-block column does not solve the problem because we only refine in the x-direction. Thus, there will still be a layer of fine low permeable cells in the refined grid preventing radial flow. This is seen in Figures 6.12(c) and 6.12(d), which show the solution for Layer 38 on the unrefined grid and the Refine$_2$-grid, respectively. We see that the pressure field hardly changes from the unrefined to the refined solution. Radial flow from Well 1 is prevented by a low-permeable block on the top of the well-block, as seen in the plot of the permeability. The plot of flux intensity for Well 1 in the refined grid shows that the flow is not radial but directed in the downward direction. The assumptions for the radial-flow well model are therefore not satisfied.

We saw in Section 6.4.1 that Layers 38, 39, 51, 52, and 85 also gave large relative errors for the methods with correct well index for square grids without refinement, but that the results were improved by increased grid resolution. The difference from the case considered here is that the refinement in Section 6.4.1 increased the resolution in both the x- and y- direction. The effect of a low permeable cell near the well will be greater for non-square cells than for square cells. The main flow direction in the simulation is perpendicular to the prolongation direction (x-direction), meaning that almost all flow will occur over the longest edge. When this edge is blocked by a low permeable cell, the flow pattern will be more affected than if the cell was square. We therefore see growth in the relative error for these layers on grids with non-square cells.

We conclude that a uniform refinement of the grid in the near-well area improves the performance of the radial-flow well model. Consequently, the performance of the new well indices for MFEM and MFDM are improved. The results indicate that the grid must be uniformly refined in order to get good results.

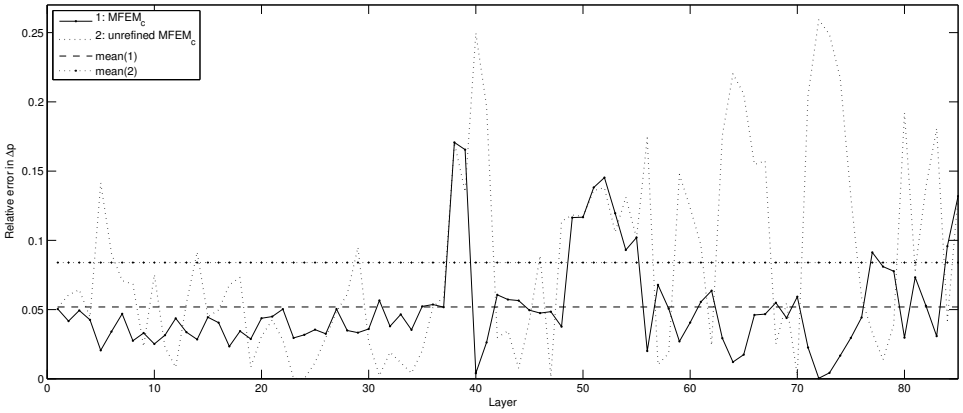

(a) Refine$_1$

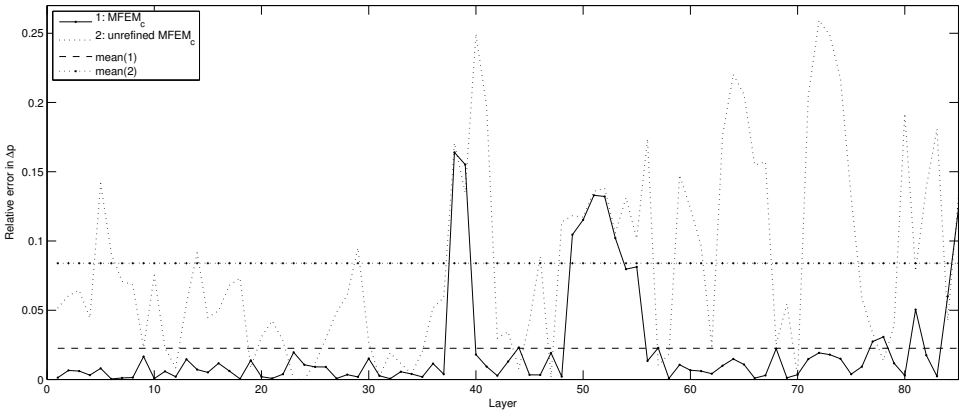

(b) Refine$_2$

Figure 6.10: Relative error for MFEM$_c$ for the two grid refinement methods.

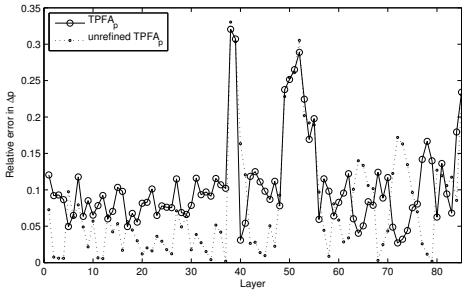

(a) Refine$_1$

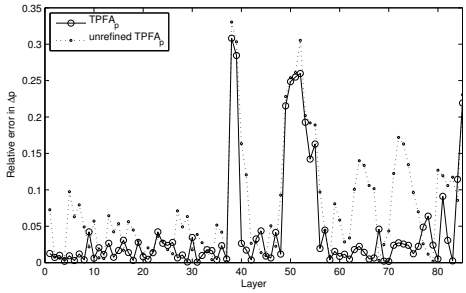

(b) Refine$_2$

Figure 6.11: Relative errors for TPFA$_p$ for the two grid refinement methods.

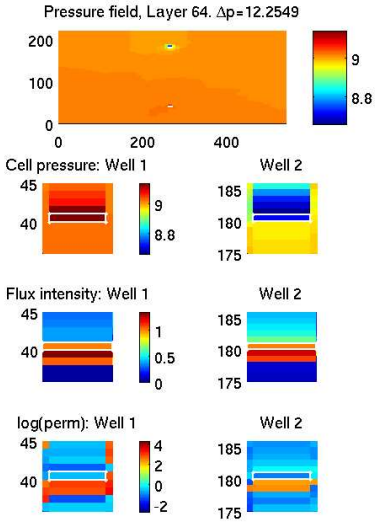

(a) Layer 64: unrefined.

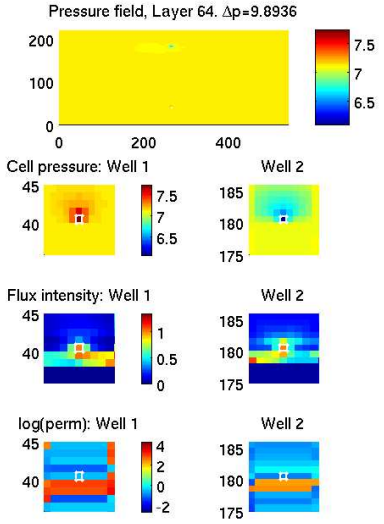

(b) Layer 64: Refine$_2$.

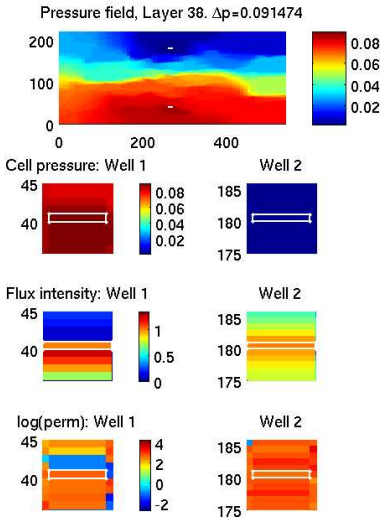

(c) Layer 38: unrefined.

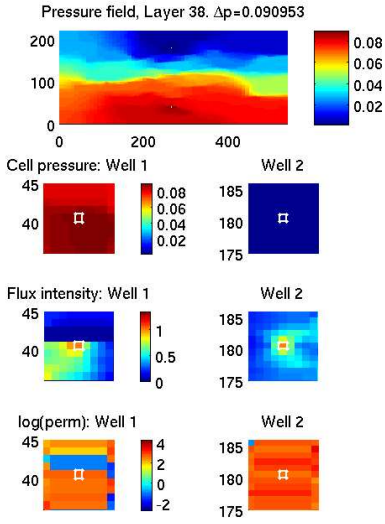

(d) Layer 38: Refine$_2$.

Figure 6.12: Plot of the pressure fields for Layers 64 and 38 with zoom in on pressure, flux, and permeability near the wells. The color scale for pressure varies in the different plots, while the color scale for flux and permeability is constant.

6.5 Chapter Conclusions

In the following we summarize the conclusions made in this chapter and propose guidelines for using the radial-flow well model.

We have seen that the relative error for MFEM$_c$, MFDM$_c$, and TPFA$_p$ lie in the same range for all the tested cases. This means that the new well indices for MFEM and MFDM presented in (6.6) and (6.7) perform as well as Peaceman's well index for TPFA. Moreover, the choice of well index has great effect on the relative error in cases where the assumptions for the radial-flow well model are sufficiently satisfied. In these cases, we have seen that the specially adapted well indices for MFEM and MFDM give better results than the same methods with Peaceman's well index. These cases include square and non-square grids with homogeneous permeability, square grids with heterogeneous permeability, and non-square grids with heterogeneous permeability and locally homogeneous near-well areas.

For non-square grids with aspect ratio $\beta > 3$ and heterogeneous permeability, the performance was not satisfactory for any of the tested methods. The relative error for the specially adapted well indices were in some cases larger than the relative error for the "wrong" well indices. This behavior was in particular found in layers where one of the well-blocks was low-permeable and had a highly heterogeneous near-well area. The choice of well index in these cases is not obvious. We conclude that the assumptions for the radial-flow well model weakens with increasing aspect ratio of the grid cells when heterogeneous permeability is used. Therefore one should try to avoid using the radial-flow well model alone in these cases. One solution to this problem is to refine the grid around the wells. Simulations on a grid where the cells in column of the grid containing the well-block was refined to square cells gave good results for almost all cases. The exception were layers with low pressure drop and violation of the near-well radial flow assumption. If a refinement is to be used in the near-well area, it is important that the refinement is uniform and includes enough cells to satisfy the assumption of a uniform near-well area. Further work should be done to test the performance when only the cells in the near-well areas are refined. Another possible solution to the problems could be to develop a well index for grids with high aspect ratios that takes into account the permeability in the near-well area.

The weaknesses found in the specially adapted well indices for MFEM and MFDM are due to violation of the assumptions for the radial-flow well model. In the identified problem cases, the use of the radial-flow well model should be avoided if possible. However, as we mentioned in Chapter 4, there are currently no alternatives to the radial-flow well model that are adapted for use with MFEM and MFDM. One possible approach could be to use one of the more complex well models (see Section 4.3) that are developed for TPFA. The effect of this approach is uncertain, but it can possibly result in large errors as we have seen for MFEM and MFDM with Peaceman's well index in this chapter. The remaining alternative is to use no well model at all, but this alternative would give even larger errors than the radial-flow well model. In conclusion, the radial-flow well model is the only

real alternative until more complex well models for MFEM and MFDM have been developed.

If the radial-flow well model is to be used, it is important to know what cases that might result in errors. Based on the tests in this chapter, we propose the following guidelines for the use of the model:

- The well model can be used for rectangular grids with homogeneous permeability.
- The well model can be used for square grids with heterogeneous permeability, but should be used with caution if the well-block has low permeable neighbor cells that prevent near-well radial flow.
- The well model can give large errors for grids with high aspect ratios on heterogeneous reservoirs if a large amount of the pressure drop happens near the well. If the well model is to be used in these cases, the grid should be uniformly refined in an area near the well.
- The well model can be used alone for non-square cells with high aspect ratios if the permeability in the dependence area, which is the cells near the well-block, is close to homogeneous. The dependence area in this case includes at least the neighbor cells of the well-block and possibly also the cells intersected by the equivalent radius.

Part III

Improved Representation of Wells in the Multiscale Mixed Finite Element Method

Chapter 7

Introduction to Multiscale Methods

7.1 Background

When solving a PDE numerically, accuracy and efficiency are often in conflict. New technology has made it possible to make very detailed, high-resolution geomodels of reservoirs, but it is not straight forward to use these geomodels in reservoir simulation. A direct approach with one of the methods described in Chapter 3 is not applicable for simulating a large and complex grid model of a heterogeneous reservoir repeatedly. The issues are the run time and the memory use of the simulation. As a consequence, a number of methods applying upscaling/downscaling and multiscale techniques have been developed. A commonality of these methods is the use of two different sets of grids: a fine subgrid that utilizes the detailed geomodel, and a coarse grid that is used for simulation. In this thesis we focus on the multiscale mixed FEM (MsMFEM) [4, 11]. This method is based on a multiscale finite element method (MsFEM) [19] that uses special finite element basis functions to account for the subscale variations in the differential operators. In [11] a mixed formulation was introduced to the framework of MsFEM to obtain a MsMFEM that is conservative on a coarse grid and locally mass conservative for coarse blocks not containing sources. The method presented here is a version of MsMFEM, developed by Aarnes et al. [4], that is conservative on the entire underlying subgrid. This method has been tested with good results for two-phase simulations on a typical geomodel arising from real-life reservoir engineering in [4].

7.2 The Multiscale Mixed Finite Element Method

In Section 3.4 we introduced the concept of basis functions for the mixed FEM. In multiscale mixed FEMs, the basis functions are used to describe variation on a subgrid scale when the pressure and flow system is solved on a coarse grid. For one-phase flow simulations, the basis functions from the fine grid need only to be

computed once as long as the underlying geomodel does not change. Furthermore, the solution of the coarse grid system is fast, and hence repeated simulations of a reservoir can be done efficiently. In a two-phase flow simulation, the pressure equation (2.4)–(2.5) and a saturation equation are solved repeatedly. It has been shown that the multiscale basis functions for two-phase flow simulation need only to be computed once or updated infrequently [20]. A simulation of two-phase flow can therefore be done very efficiently by a multiscale method. We will not go into details of two-phase flow simulations here, but to motivate the application areas for MsMFEM we sketch the steps of a two-phase flow simulation with MsMFEM:

1. Compute flux basis functions that incorporate subgrid variations for each interface in the coarse grid. Consider also the wells as interfaces.
2. **for n=1 to N**
   - Solve for flow and pressure on the coarse grid based on the current saturation by a mixed FEM with the basis functions for flux obtained in Step 1.
   - Use basis functions and coarse grid flux solution to compute fine scale flux field.
   - Advance fine-scale saturation by time step.

   end

In the following, we will focus on step 1 of this process, and the reader is referred to [2] for more details on two-phase flow simulation.

7.2.1 Basis functions

Let $\Omega_c = \{B\}$ be a coarse grid where each grid block is a connected union of grid cells from a fine grid Ω_h. We will refer to $E \in \Omega_h$ as a cell in the fine grid and $B \in \Omega_c$ as a block in the coarse grid. Further let $\Gamma = B_i \cup B_j$ be an interface in the coarse grid, and denote by $\partial\Omega_c$ the collection of interfaces in Ω_c. Moreover, define $U_{ij} = B_i \cup \Gamma_{ij} \cup B_j$. For each interface Γ in the coarse grid corresponding to a pair of blocks $B_i, B_j \in \Omega_c$, we define a basis function $\boldsymbol{\psi}_\Gamma$ as the discrete solution to the following problem

$$\begin{aligned} \vec{\psi}_\Gamma &= -\mathbf{K}\nabla\phi_{ij}, && \text{in } \Omega, \\ \nabla \cdot \vec{\psi}_\Gamma &= w, && \text{in } U_{ij}, \\ \vec{\psi}_\Gamma \cdot \vec{n}_\Gamma &= 0, && \text{on } \partial U_{ij}, \end{aligned} \tag{7.1}$$

where ϕ_{ij} has support in U_{ij}. Notice that this implies that $\vec{\psi}_\Gamma$ is defined on the entire set Ω, but that it only has support on U_{ij}. The source function for isotropic

permeability $\mathbf{K}(\vec{x}) = k(\vec{x})\mathbf{I}$ w is given by

$$w(\vec{x}) = \begin{cases} k(\vec{x})/(\int_{B_i} k(x)\, d\vec{x}), & \vec{x} \in B_i, \\ -k(\vec{x})/(\int_{B_j} k(x)\, d\vec{x}), & \vec{x} \in B_j. \end{cases} \tag{7.2}$$

This formulation of the source functions provides unit flux across Γ, see [4] for details. The system (7.1) is solved numerically on the underlying fine grid of U_{ij} by a *subgrid solver*. In principle, any conservative numerical method can be used as a subgrid solver, but the mimetic FDM is a particular versatile approach because of the easy implementation on general polyhedral grids. As before, we assume $\mathbf{K} = k(\vec{x})\mathbf{I}$ to be constant on each cell, so the discrete version of w on each cell is

$$w(E) = \begin{cases} k_E|E|/(\sum_{E_k \in B_i} k_{E_k}|E_k|), & E \in B_i, \\ -k_E|E|/(\sum_{E_k \in B_j} k_{E_k}|E_k|), & E \in B_j. \end{cases} \tag{7.3}$$

Notice that the system (7.1) is on the same form as the prototype flow problem (3.2)–(3.4). The linear hybrid system arising from a discretization of (7.1) with mixed FEM or mimetic FDM is therefore on the well-known form introduced in (3.42) or (3.81), respectively. In the solution, the variable of interest is the basis function $\boldsymbol{\psi}_\Gamma$. This is because the variations on a subscale are greater for a flux field than for a pressure field. The coarse pressure field is a sufficient representation of the pressure, but a fine scale flux field is needed to accurately represent the flow. We solve (7.1) for every interface $\Gamma \in (\partial\Omega_c \setminus \partial\Omega)$ to obtain a flux basis function $\boldsymbol{\psi}_\Gamma$ for each interface.

The method considered above includes all interfaces Γ except the well edges. Accurate modeling of the flow in the near-well area is critical in order to obtain a correct global flow pattern. In the current version of MsMFEM, the near-well flow is modeled by a well basis function. Assume now that there is a well in block i. To integrate the well in the multiscale system we introduce the well basis function $\boldsymbol{\psi}_w = (\boldsymbol{\psi}_{v,w}, \psi_{q,w})^T$. Here, $\boldsymbol{\psi}_{v,w}$ represents the flux over the edges on the fine subgrid, while $\psi_{q,w}$ represents the flux over the well edge. The well basis function is found by restricting the system (7.1) to B_i and by adding the equation for the well

$$\mathrm{WI}_i^{-1}\psi_{q,w} - p_i + p_{wf,i} = 0, \tag{7.4}$$

to the linear system as done in Section 3.6.2. Notice that MsMFEM utilizes the well index from the subgrid solver. In addition, we set $\psi_{q,w} = 1$ to force unit flux over the well edge. Unit flux in the basis function implies that for a well rate q, $\psi_{q,w} \cdot q = q$. The discrete version of w is now restricted to B_i,

$$w(E) = \frac{-k_E|E|}{\sum_{E_k \in B_i} k_{E_k}|E_k|}, \quad E \in B_i. \tag{7.5}$$

The resulting linear system is on the same form as the linear system described in Section 3.6.2. The solution of this system provides a well basis function $\boldsymbol{\psi}_w$ with

support on B_i. Two examples of well basis functions are shown in Figure 7.1. Notice that the well basis function depends on the placement of the well in the coarse block. The well basis function fails to describe the flow from the well accurately if the well lies in a corner of the coarse well-block. This is a major source of error in the coarse system. A solution to this problem is discussed in Section 7.3.

7.2.2 The Coarse System

The coarse system is a mixed FEM discretization of the prototype flow problem (3.2)-(3.4) on the coarse grid with basis functions given by $\Psi = (\boldsymbol{\psi}_1^T, \boldsymbol{\psi}_2^T, \ldots, \boldsymbol{\psi}_n^T)$. The result is a linear system on the form given in (3.34), where the mass matrix $\mathbf{A}$ is given by

$$\mathbf{A} = \Psi^T \mathbf{A}_{\text{fine}} \Psi. \tag{7.6}$$

Here, $\mathbf{A}_{\text{fine}}$ is the corresponding mass matrix in the fine system. As explained in Section 3.4.3, the linear system for mixed FEM can be hybridized to obtain a hybrid system. The mass matrix $\mathbf{A}_{\text{hybrid}}$ in the hybrid system will be block-diagonal because the hybrid basis functions are block-wise orthogonal. We can therefore employ two Schur-complement reductions to obtain a positive definite system, see Section 3.4.3 for details.

The solution of the coarse system provides the coarse flux field $\mathbf{F}_c$ and the coarse pressure fields $\mathbf{p}_c$. The fine scale flux field $\mathbf{F}_f$ is obtained by

$$\mathbf{F}_f = \sum \mathbf{F}_c(i) \boldsymbol{\psi}_i, \tag{7.7}$$

while the coarse pressure field is used directly to account for the pressure variations in the reservoir.

7.3 Improved Representation of Wells by Overlap

The setup described above can result in large errors for the flow and pressure solution if a well lies in a corner of the coarse well-block, since the well basis function only has support on the cells inside the coarse well-block. When a well lies in the corner of a coarse block, the well basis function will not contribute directly to the flow over the interfaces making up the corner, as illustrated in Figure 7.1(b). This setup fails to model radial near-well flow, and is therefore a source of inaccuracy. To remedy this weakness we can use a technique with overlap in the well basis functions, hereafter referred to as overlap. This approach is motivated by an over-sampling technique introduced in [19]. Overlap means that we extend the support area of the well basis functions to include cells outside the coarse well-block. The procedure for finding $\boldsymbol{\psi}_w$ is still the same, but the system is solved on a larger domain. Assume again that a well is in block B_i. The system (7.1) for finding $\boldsymbol{\psi}_w$ is

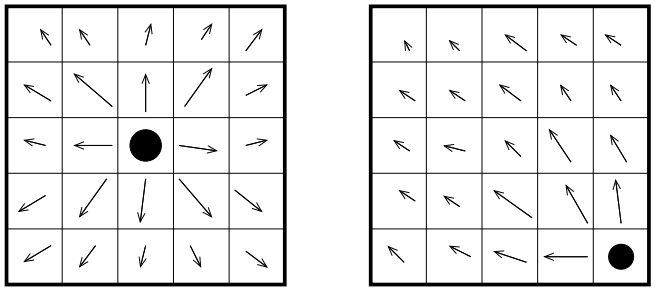

(a) Well in the center of the coarse well-block.

(b) Well in a corner of the coarse well-block.

Figure 7.1: Examples of well basis functions for different placements of the well in the coarse well block.

now solved on $V_i = B_i \cup O_{ex}$, where O_{ex} is a union of the cells in the extended support area. The discrete version of the function w on the extended domain is still

$$w(E) = \begin{cases} \frac{-k_E|E|}{\sum_{E_k \in B_i} k_{E_k}|E_k|}, & E \in B_i, \\ 0, & E \notin B_i, \end{cases} \tag{7.8}$$

and the no-flow boundary conditions now apply to V_i,

$$\vec{\psi}_w \cdot n = 0 \quad \text{on } \partial V_i. \tag{7.9}$$

We define overlap of degree 1, hereafter referred to as overlap 1, to be $O_{ex} = O_1$, where

$$O_1 = \{E \in (\Omega_h \setminus B_i) : E \cap \partial B_i \neq \emptyset\}.$$

Further, overlap 2 is defined as $O_{ex} = O_2$, where

$$O_2 = O_1 \cup \{E \in (\Omega_h \setminus (B_i \cup O_1) : E \cap \partial O_1 \neq \emptyset\}.$$

In other words, O_1 consists of the fine cells that are neighboring an interface of the coarse well-block B_i. Furthermore, O_2 is a union of O_1 and the cells that are neighboring O_1, but that are not in B_i. Higher degrees of overlap are defined accordingly. Figure 7.2 shows a well-block with O_1 and O_2 indicated.

As explained above, overlap increases the support of the well basis function $\boldsymbol{\psi}_w$ to include non-neighboring blocks of the well-block. The results is that the mass matrix $\mathbf{A}$ in the coarse hybrid system no longer is block-diagonal. The price of the increased accuracy is thus a more complex linear system. There is no longer any gain from using a hybrid mixed FEM formulation since the linear system can not be reduced to a positive definite system. We must therefore consider the increased accuracy relative to the increased complexity. We will test the effect of using overlap on the accuracy of MsMFEM in Chapter 8.

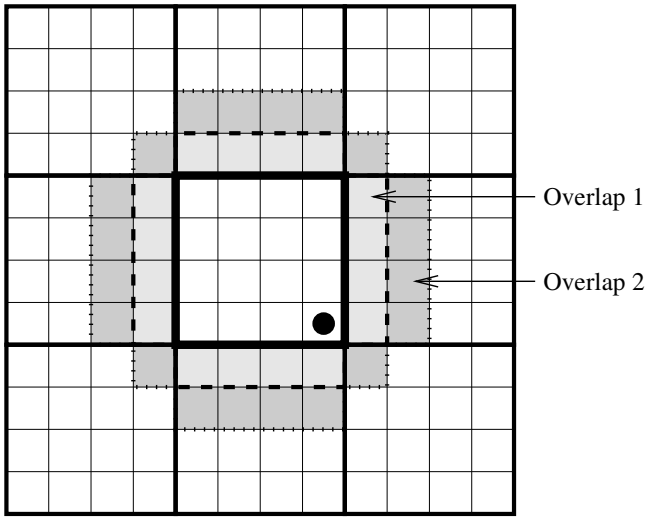

Figure 7.2: Coarse well-block where the well lies in a corner of the block. Overlap of degrees 1 and 2 are indicated on the figure.

Chapter 8

Test of Overlap in Well Basis Functions

The current representation of wells in MsMFEM, presented in the previous chapter, can give inaccurate results for certain well placements. This is because the well basis functions only have support within the coarse well-block. If a well lies in a corner of the coarse well-block, the well basis function will only directly contribute to flow inside the well-block. Thus, this setup fails to model the radial near-well flow correctly and therefore causes errors in the fine scale flux solution and in the coarse pressure solution. In this chapter, we test the effect of using the overlap technique, which was introduced in the previous chapter, on the well basis functions in MsMFEM. The tests are done by numerical simulations for different degrees of overlap on different well positions within the coarse well-block.

8.1 Setup for Numerical Simulations

8.1.1 Grid and reservoir data

The fine grid and the reservoir data are described in Section 6.2.1. We construct a coarse grid by partitioning the cells in the fine grid into coarse blocks of size 10×10 cells to obtain a uniform, square, coarse grid of size 6×22 blocks. For the later discussion we define the *diameter* of a coarse grid block to be the length of the longest edge. This definition applies to both 2D coarse blocks, which is considered here, and 3D grid coarse blocks. Furthermore, to test the effect of overlap in different situations, we use the following placements of the wells within the coarse well-blocks:

Corner: both wells lie in a corner of the coarse well-blocks. This is the well placement used in Chapter 6.

Edge: both wells lie next to an edge in the coarse well-blocks. This corresponds to moving the corner wells 5 cells in x-direction.

Center: both wells lie in the center of the coarse well-blocks. This corresponds to moving the corner wells 5 cells in both x- and y-direction.

For the heterogeneous case, this setup gives differences in the near-well areas for the different well-placements on a given permeability layer. To avoid effects from different permeability distributions in the near-well areas, we move the grid instead of moving the wells in the heterogeneous case. The resulting grid must then be reduced to become uniform in the corner and edge cases. Hence, the grid for the edge case is 5×22 coarse blocks, while the grid in the center case is 5×21 coarse blocks.

In the numerical simulations, we solve the prototype flow problem with no-flow boundary conditions (3.2)–(3.4). The numerical method used on the coarse grid is the multiscale mixed FEM, which is hereafter referred to as the multiscale method. The subgrid solver used in the multiscale method is the mimetic FDM defined by the α-inner product (3.80) with $\alpha = 2$. This method is also used to solve the system on the fine grid. Moreover, we denote by ω the degree of overlap used. Simulations with the multiscale method are carried out using overlap $\omega = \{0, 1, 3, 5, 10\}$.

8.1.2 Measurement of the error

The solution to the fine grid problem is used as a reference solution to measure the error. Recall from Chapter 6 that the pressure drop Δp is defined as the pressure difference between the injection and the production well. The error is measured by looking at the relative error between the pressure drop in the reference solution and the pressure drop in the multiscale solution. Let W be the placement of the wells in the coarse well-blocks, and let ω be the degree of overlap. We define the relative error as

$$e_r(W, \omega) = \frac{|\Delta p_{\text{ref}} - \Delta p_{W,\omega}|}{\Delta p_{\text{ref}}}. \tag{8.1}$$

Since we look at the relative error, it does not matter which well index is used as long as we use the same well index for both the reference solution and the multiscale solution. The relative error in a simulation can be split in two: the first part is the error in the multiscale method, while the second part comes from the representation of the wells, in this case whether we use overlap or not.

8.2 Results for Homogeneous Reservoir

The results from the simulations with homogeneous permeability are shown in Table 8.1. For the corner well we see that overlap gives a great increase in the performance of the multiscale method. This is also the case for the edge well, though the initial error without overlap is smaller in this case so the potential improvement is also smaller. Despite the improvements, the results for overlap 10 for the corner and edge wells are not as good as the results for the center well without overlap. Thus, if possible, it is better to make a coarse grid partition that gives a center well

Table 8.1: Relative errors for different overlap and well placements for a homogeneous reservoir.

ω	**Corner**	**Edge**	**Center**
0	0.2926	0.0813	0.0080
1	0.1277	0.0287	0.0065
3	0.0520	0.0149	0.0061
5	0.0279	0.0123	0.0061
10	0.0095	0.0082	0.0061

Table 8.2: Statistics for relative errors for **Corner** well placement.

(a) Layers 1–35 (Tarbert)

ω	mean	max	std
0	0.717	2.400	0.572
1	0.293	1.270	0.245
3	0.123	0.452	0.095
5	0.069	0.236	0.044
10	0.035	0.102	0.023

(b) Layers 36–85 (Upper Ness)

ω	mean	max	std
0	1.674	7.008	1.569
1	0.945	8.872	1.811
3	0.515	5.249	1.183
5	0.313	3.681	0.734
10	0.121	0.913	0.175

placement than to use overlap 10 for corner or edge wells. For the corner placement, there is significant difference between the relative error with overlap 5 and 10. Thus, for this case it pays off to use overlap 10. In the case of the edge well, on the other hand, there are not much differences between the relative errors for overlap 3, 5, and 10. In conclusion, there is not much to gain from using a higher overlap than 3 for the edge case. Finally, for the center case, overlap does not give much effect in terms of error reduction. The difference is small between the relative error for no overlap and overlap 1. Overlap 1 does give some improvement, but higher overlap than 1 is clearly superfluous.

The effect of using overlap on the coarse pressure and fine flux field is shown in Figure 8.1. The figure compares the multiscale solutions up to overlap 5 to the reference solution. The conclusions stated above are confirmed in the figure. We see that overlap gives great improvement in both the corner and edge cases, but not in the center case.

8.3 Results for Heterogeneous Reservoir

The results from the simulations with heterogeneous permeability are shown in Tables 8.2, 8.3, and 8.4. The tables show that the relative errors are much larger for the heterogeneous case than for the homogeneous case. Moreover, the relative errors are larger for the fluvial Layers 36–85 than for the more smooth permeability fields in Layers 1–35. This tendency was expected since the current implementa-

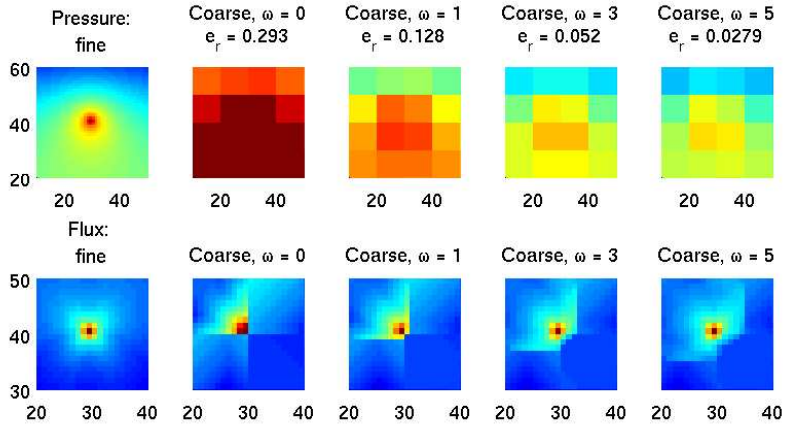

(a) Corner

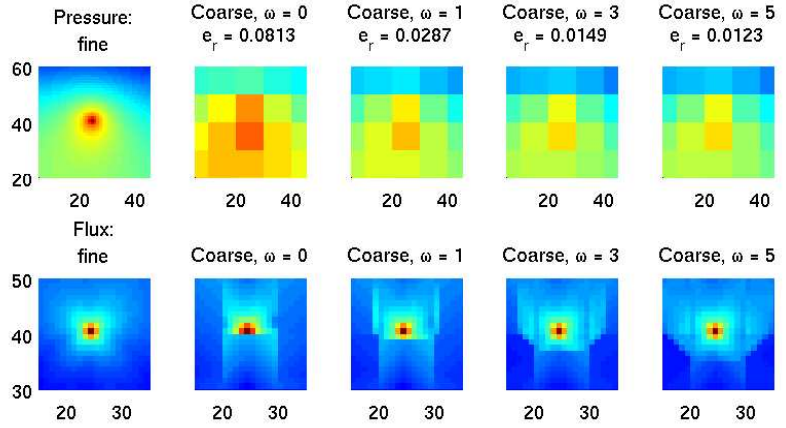

(b) Edge

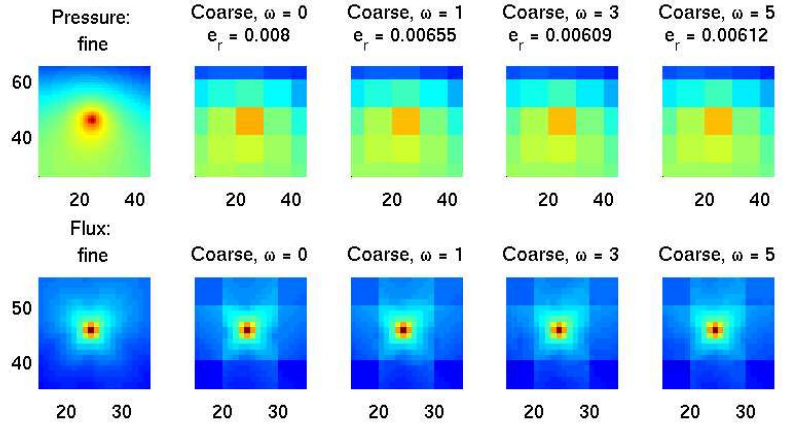

(c) Center

Figure 8.1: Multiscale solution of pressure and flux for a homogeneous reservoir model with different degrees of overlap. The color scales for both the pressure plots and the flux plots are constant.

Table 8.3: Statistics for relative error for **Edge** well placement.

(a) Layers 1–35 (Tarbert)

ω	mean	max	std
0	0.194	0.596	0.126
1	0.073	0.235	0.038
3	0.043	0.105	0.017
5	0.037	0.100	0.017
10	0.029	0.065	0.015

(b) Layers 36–85 (Upper Ness)

ω	mean	max	std
0	0.590	3.888	0.776
1	0.172	0.931	0.172
3	0.127	1.128	0.173
5	0.107	0.717	0.122
10	0.082	0.402	0.081

Table 8.4: Statistics for relative error for **Center** well placement.

(a) Layers 1–35 (Tarbert)

ω	mean	max	std
0	0.030	0.055	0.012
1	0.026	0.054	0.011
3	0.024	0.054	0.011
5	0.023	0.054	0.012
10	0.023	0.054	0.012

(b) Layers 36–85 (Upper Ness)

ω	mean	max	std
0	0.073	0.338	0.078
1	0.076	0.403	0.090
3	0.069	0.330	0.080
5	0.067	0.329	0.078
10	0.061	0.316	0.074

tion of MsMFEM is known to have limitations [3] on layers with high permeable channels and low permeable barriers as in Layers 36–85. Furthermore, as in the homogeneous case, we observe that overlap reduces the relative error significantly in the corner and edge cases, while the effect of overlap is small in the center case. The results without overlap in the center case are in the same range or better than the results for overlap 10 in the corner and edge cases. In addition, the tables show that overlap in some cases increases the relative error. The max relative error for Layers 36–85 is smaller without overlap than with overlap 1 for the corner and center cases. Small overlap can increase the relative error in cases where the multiscale solution without overlap is far from the correct flow pattern. Even though a more correct flow pattern is achieved through the use of overlap, this may not be reflected in the coarse pressure solution.

Plots of the relative error for the different cases are shown in Figure 8.2. The y-axes in the plots for the corner and edge cases are scaled to ignore the largest outliers. For the corner case, shown in Figure 8.2(a), there is little difference between overlap 3 and 5 for most layers, and the difference is even less between overlap 5 and 10. The term little difference is here interpreted as little relative to the initial error. Thus, in most cases it would be sufficient to use overlap 3 or 5, but some problem cases, for instance Layer 66, requires overlap 10 to give good results. These problem cases are discussed later in this chapter. Further, we observe that overlap 10 gives a robust method for Layers 1–35 with max relative error of 10%. For Layers 36–85, on the other hand, the max relative error is over 90% even

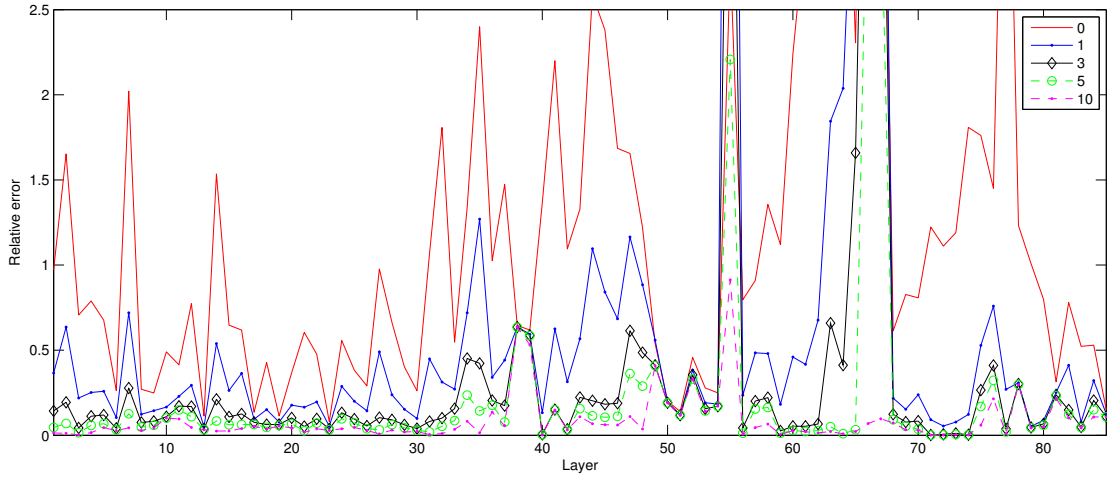

(a) Corner

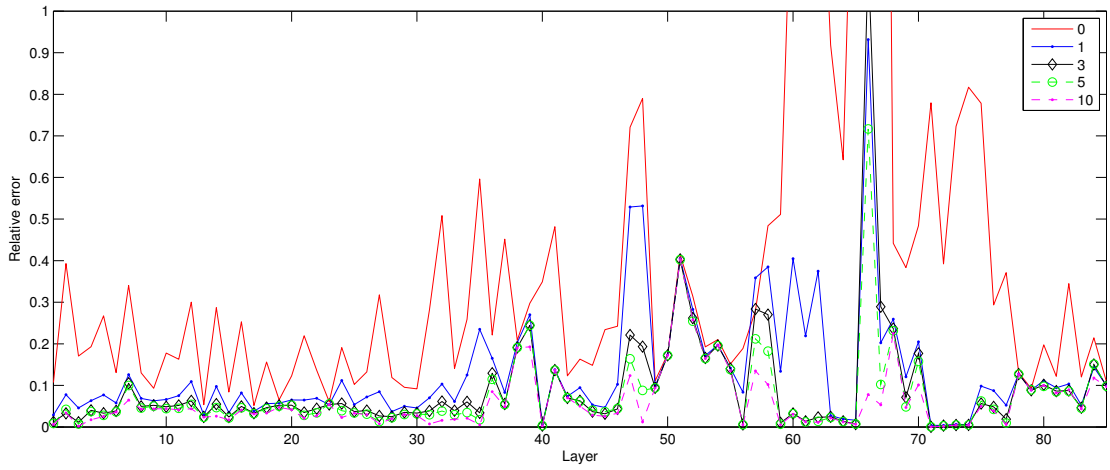

(b) Edge

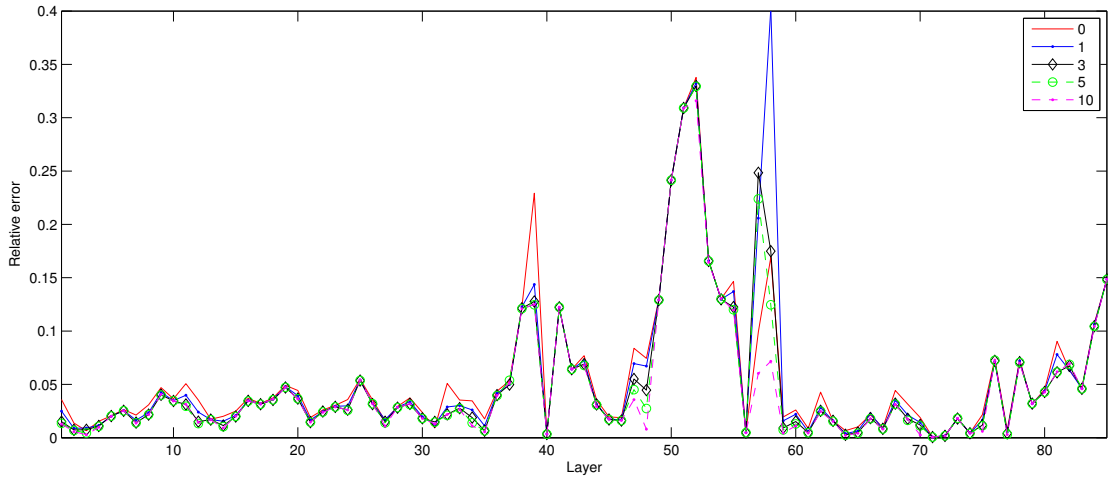

(c) Center

Figure 8.2: Plots of relative error for different overlap. Note that the scaling of the y-axis differs in the plots, and that the largest outliers are removed in the corner and edge cases.

when overlap 10 is applied. This is because some layers, such as Layer 55, have large initial errors that are not sufficiently reduced by overlap. The problem here is not directly the representation of the wells, but that the the current version of the multiscale method fails to give an accurate representation of the flow pattern in the reservoir. Possible solutions to this problem is discussed in the conclusion at the end of the chapter. Another finding is that the relative errors for the Layers 38, 39, 51, 52, and 53 are not improved by overlap. We recall from Chapter 6 that these layers gave problems with convergence even for the fine grid system, which partly explains the lack of convergence on the coarse grid.

For the edge case, the differences between overlap 3, 5, and 10 are small for most cases. Here it would suffice to use overlap 3 for Layers 1–35, but some layers in Layers 36–85 still have large relative errors for overlap 5 or 10. The plot for the center case confirms the conclusion that overlap does not improve the performance significantly. With exception of Layer 39, using overlap gives approximately the same or worse results than with no overlap. However, as argued above, the flow pattern might be improved by the overlap even if the relative error in the pressure increases.

We now take a closer look at the worst problem case in the corner simulation, Layer 66. The relative error for no overlap in this case was 7.6, while overlap 5 and 10 gave 3.7 and 0.1 in relative error, respectively. Figure 8.3 shows the permeability and the flux near the production well in the cases: reference solution, no overlap, and overlap 10. This figure illustrates a worst case scenario with respect to corner well placement. The permeability in the coarse well block is low, but there is a thin, high permeable channel neighboring the well, going through the three coarse blocks making up the corner. In addition, there is a small high permeable area in the uppermost right corner of the coarse well block. The figure shows that the flux field for the multiscale solution without overlap deviates greatly from the reference solution. The solution for overlap 10 is better because much of the error coming from the representation of the well is gone. Nevertheless, there is still a significant difference between the flux field in the reference solution and the solution with overlap 10. The remaining error is partly due to weaknesses in modeling flow in high permeable channel structures in the current version of MsMFEM. Layer 66 also gave large relative error in the edge case, but not in the center case. The reason is, in part, that the different well placements give different coarse partitions of the grid. The characteristics of the well-blocks will therefore vary in the different cases.

Equivalent simulations on the full coarse grid (6×22 coarse grid blocks) were also done by moving the wells in the edge and center cases instead of moving the grid. The resulting mean relative error for the different cases were in the same range as the results in Tables 8.2, 8.3, and 8.4. This means that we did not lose any accuracy when the simulation area was reduced in the edge and center cases. We remark that the setup with moving the grid, as done herein, is more relevant as a real-life reservoir simulation case because wells normally have specific placements in a real-life case.

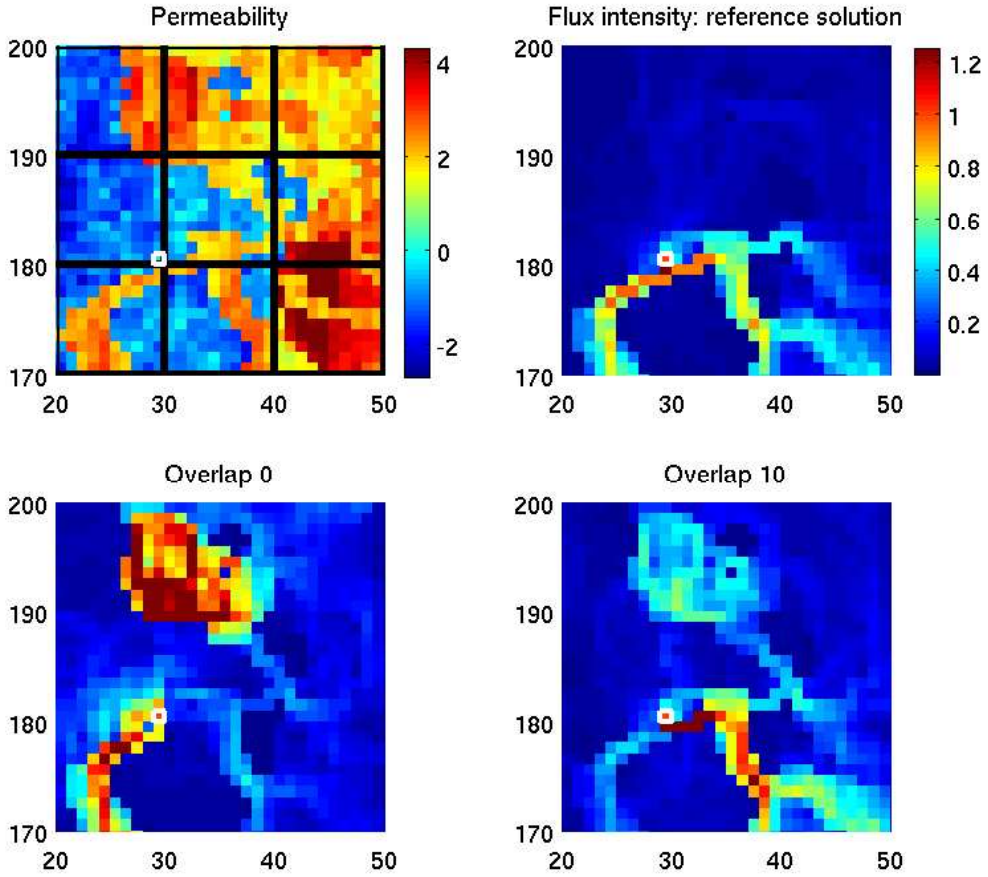

Figure 8.3: Permeability and flux near the production well in Layer 66. The fine well-block is marked with white edges. Note that the multiscale method fails to model the flow correctly.

Table 8.5: Refine5: Statistics for relative errors for **Corner** well.

(a) Layers 1–35 (Tarbert)

ω	mean	max	std
0	0.386	1.110	0.279
1	0.124	0.347	0.090
3	0.053	0.135	0.027
5	0.034	0.063	0.012
10	0.027	0.048	0.010

(b) Layers 36–85 (Upper Ness)

ω	mean	max	std
0	1.025	4.428	1.018
1	0.245	1.835	0.285
3	0.096	0.521	0.100
5	0.071	0.343	0.067
10	0.061	0.269	0.055

8.4 Generalization of Results

In order to establish results for a general coarse partition of the grid, several coarse grid partitions must be considered. To generalize the results, we introduce two additional coarse grid partitions. The first, Refine5, is finer than the original, while the second, Coarse15, is coarser than the original. These grid partitions give square coarse grid blocks of 5×5 and 15×15 fine cells, respectively.

New simulations were done for the corner well placement where we found the largest errors in the original simulations. The results are displayed in Table 8.5 for Refine5 and in Table 8.6 for Coarse15. The results for Refine5 are better than for the original case, which could be expected since the coarse grid is finer. Moreover, overlap of degree equal to the diameter of the coarse well-block gives relative error of less than 10% for all layers in Layers 1–35, as we also saw in the original case. Furthermore, for Coarse15 the relative errors are smaller than in the original case for $\omega = \{0, 1\}$, but in the same range or larger for higher ω. The smaller relative errors might be due to that the well basis function without overlap covers a larger part of the reservoir when the size of the well-block is increased.

Once again, we observe that overlap of degree equal to the diameter of the coarse well-block gives relative error of less or equal to 10% for all layers in Layers 1–35. However, the results indicate that there is less to gain from increasing the overlap from 10 to 15 in Coarse15 than for an increase of overlap from 5 to 10 in the original case. One possible explanation is that the support of the well basis function in the near-well area is the most critical for accurate well representation. Thus, if the well basis function already has support in the critical near-well area, the effect of additional overlap is small. This is precisely what we saw in the center well case.

8.5 Chapter Conclusions

The representation of a well in MsMFEM without use of overlap is good when the well is placed in the center of the coarse well-block. Adding overlap in this case does not improve the results significantly. On the other hand, if a well lies in a

Table 8.6: Coarse15: Statistics for relative errors for **Corner** well.

(a) Layers 1–35 (Tarbert)

ω	mean	max	std
0	0.579	2.453	0.488
1	0.289	1.045	0.254
3	0.145	0.539	0.124
5	0.092	0.360	0.075
10	0.050	0.134	0.033
15	0.036	0.103	0.023

(b) Layers 36–85 (Upper Ness)

ω	mean	max	std
0	1.406	8.654	1.641
1	0.880	7.575	1.384
3	0.576	5.178	1.056
5	0.422	4.023	0.862
10	0.189	1.168	0.264
15	0.146	1.024	0.217

corner or close to an interface of the coarse well-block, a representation of the well without overlap is poor. The representation in these cases is improved by increasing overlap. Nevertheless, even if we use overlap equal to the diameter of the coarse well-blocks, the results are still not as good as the center well case without overlap. We therefore conclude that the best way to represent a well in MsMFEM, for the cases tested here, is to make a coarse grid partition that places the well in the center of the well-block. For a complex geomodel, this is not necessary straight forward due to additional requirements [4] posed on the coarse grid partition to avoid inaccuracy in the MsMFEM solution.

If center well placement is not possible, overlap is a good remedy for the problems. Let n denote the diameter of a coarse well-block in a uniform, square, coarse grid partition. For most of the cases tested it is sufficient to use overlap equal to $n/2$ in order to get good results. The gain from using overlap higher than $n/2$ is in general small and a higher overlap is only necessary for difficult layers. However, to obtain a method that is robust for different well placements and near-well permeabilities we recommend to use overlap n. For the majority of the tested cases, overlap n gives a robust method with relative error less that 10% for all well placements. These cases include Layers 1–35 and the majority of the layers in Layer 36–85. We remark that the results for Coarse15 indicate that the effect of overlap is reduced after a certain limit, and that this limit is lower than the well-block diameter for very coarse blocks. The results shown here are obtained on square uniform grid partitions, but could also be applied to uniform non-square grid partitions. In this case, the recommendation of using overlap of degree n might be too strict for blocks with high aspect ratios. The results do not, however, immediately extend to non-uniform grid partitions, even though n is defined to only depend on the size of the coarse well-block. More testing is necessary in order to conclude for non-uniform grids.

The current version of overlap extends the support area of the well basis function in all directions, but the effect is greatest near the well. If the well lies in a corner, the gain from extending the support area over the opposite corner is small. It would therefore be interesting to investigate a "local" overlap that only extends the support over the interfaces that are close to the well. This might complicate the

implementation, and the approach is only interesting if it reduces the simulation time and/or the memory use compared to the original approach.

As already mentioned, the tests have shown that some layers give large relative errors even with overlap n or center well placement. This behavior is found in highly heterogeneous layers with channel structures in Layers 35–85. In the worst case, the relative error was still over 100% when overlap n was applied. The remaining error is not directly caused by the representation of the wells, but is due to weaknesses in the version of the multiscale method used. One approach that can reduce this error is to use *global boundary conditions* [1] when computing the basis functions. These boundary conditions are robust, but requires a computation of an initial flux field F^0 on the fine grid. With this approach, the basis function for an interface in the coarse grid is computed using the fine flux from F^0 as a boundary condition on the interface. However, it is not always desirable to compute an initial flux field. Another possible solution for reducing the error is to use the overlap technique on all the basis functions, named here *global overlap*. Considering the results obtained in this chapter, global overlap is an interesting direction for further investigations.

In this study we have not considered the increased computational time and memory consumption from using overlap. If the increase is relatively small compared to the time and memory use of the original simulation, overlap could be applied as a precaution in all cases. One of the downsides of using overlap is that a hybrid discretization with Schur-complement reduction is not possible. The linear system will thus be indefinite and therefore harder to solve. This can be considered as the *initial cost* of using overlap. If the initial cost turns out to be the main problem with using overlap, it would not matter much whether we use overlap 1 or 10 if overlap is to be used anyway. Thus, under the hypothesis that the initial cost is the largest, we would recommend to use high overlap if overlap is to be used. Additionally, we remark that if this hypothesis is true, the gain from using local overlap would be small. Further work is necessary in order to conclude on this hypothesis.

Part IV

Conclusions and Further Work

Chapter 9

Conclusions and Further Work

In this chapter we summarize the conclusions made in the previous chapters of the thesis and recommend further work. Part II and Part III of the thesis are treated separately.

9.1 Well Models for Mimetic Finite Difference Methods

The principal objective of Part II of this thesis was to develop well models for mimetic finite difference methods (FDMs).

9.1.1 Conclusions

The well models considered here relate the numerically calculated well-block pressure to the well pressure and the well rate through a well index (WI). The well index is distinct for a numerical method because different numerical methods calculate different well-block pressures. In this thesis we have considered Peaceman's radial-flow well model, which calculates the well index by the use of an equivalent radius r_0.

A numerical extension of Peaceman's well model to mimetic FDMs was treated in Chapter 4. The results indicate that there is a connection between the eigenvalues of the mimetic inner product matrix $\mathbf{T}_E$ and the equivalent radius r_0. Attempts on finding a general expression for the well index for a family of mimetic FDMs based on this relationship were not successful. Until this problem is investigated further, r_0 must be calculated by the numerical procedure in Section 5.3 for each mimetic inner product. We have used this numerical procedure to develop numerical well indices, based on Peaceman's radial-flow well model, for the RT_0-mixed FEM and a mimetic FDM. These new well indices have been shown to perform as well as Peaceman's WI for TPFA, when compared to a reference solution obtained on a near-well radial grid. Moreover, the choice of well index has been shown to have great effect on the accuracy in cases where the assumptions of the well model are sufficiently satisfied. In these cases, over-prediction of the production rate is the

result if Peaceman's WI is used with either the RT_0-mixed FEM or the mimetic FDM.

Furthermore, we have discovered that violations in the assumptions of the radial-flow well model, such as heterogeneous permeability and non-uniform grid in the near-well areas, can give large relative errors in the pressure drop between wells. However, there are few analytical well models, even for TPFA, that are developed to handle highly heterogeneous permeability in the near-well area. For mimetic FDMs, there currently exist no alternative well models. Thus, the radial-flow well model must be used until more complex well models for mimetic FDMs have been developed. Therefore it is important to be aware of the weaknesses in the model. The tests in Chapter 6 showed that the model has satisfactory performance in the following cases:

- rectangular grids with homogeneous permeability,
- rectangular grids with heterogeneous permeability and locally low aspect ratios near the wells.

We remark that these results were obtained following already known requirements, discussed in Chapter 4, on distance between wells and well placement away from boundaries.

This study has been restricted to 2D and to vertical wells placed in the center of the well-block. The new well indices can be used in 3D if the flow is horizontal near a vertical wellbore. Furthermore, it is possible to extend the approach to horizontal wells, but grid cells in reservoir simulations usually have high horizontal to vertical aspect ratios. Thus, satisfactory performance is not guaranteed for heterogeneous permeability. Moreover, the extension to diagonal, anisotropic permeability tensors follows directly from Peaceman's derivation in [25], but the tests considered herein have been limited to isotropic permeability.

9.1.2 Further work

There are many possibilities for further development of well models for mimetic FDMs. The extension of Peaceman's well model done in this thesis facilitates a foundation upon which more complex well models can be built. The most interesting directions of further investigation, considered by the author, are stated in the following.

This study has only considered numerical extension of Peaceman's radial-flow well model. In order to find a general expression for the well index for a given mimetic inner product, analytical results are probably necessary. It would therefore be interesting to do a further investigation on the relationship between the inner product in mimetic FDMs and the well index. Since mimetic FDMs are a relatively recent class of methods, there is not much analytical machinery to rely on. To find analytical connections might therefore be difficult.

In many cases, the low performance of the radial-flow well model can be predicted from the permeability in the near-well area. We have in particular identified two situations that can lead to errors: low-permeable near-well area inside larger high-permeable area, and high-permeable well-block with low-permeable neighbor cells that prevent near-well radial flow. If these observations were systematized further, one could possibly develop a well index that takes into account the permeability in the near-well area. Such a well index could potentially solve some of the problems in the radial-flow well model.

However, given the weaknesses discovered in the radial-flow well model, the perhaps most interesting direction for further work is to extend a more robust existing well model to mimetic FDMs. In particular, the semi-analytical well model [31] is an interesting candidate for further extensions. While Peaceman's well model is only suitable for conventional wells, the semi-analytical well model is developed to handle the challenges posed by todays increasingly complex well configurations. The semi-analytical well model has been shown to be superior to Peaceman's well model for both conventional and non-conventional wells in [29].

9.2 Representation of Wells in Multiscale Methods

The principal objective of Part III of this thesis was to improve the representation of wells in the multiscale mixed finite element method (MsMFEM).

9.2.1 Conclusions

The representation of wells in the version of MsMFEM [4] presented in Chapter 7 can result in large errors if a well lies in a corner or near an interface of the coarse well-block. We therefore introduced the overlap technique as a possible solution to the problems. Tests were done for MsMFEM with the overlap technique on both homogeneous and heterogeneous reservoirs and the results were compared to the solution of the fine-grid problem. The results show that overlap can remedy the problems in the original well representation. However, we have seen that overlap of degree equal to the diameter of the coarse well-block could not match the performance of a case with the well placed in the center of the coarse well-block. In conclusion, the best way to represent a well in MsMFEM is to make a coarse grid partition that places the well in the center of the coarse well-block.

If a center well placement is not possible, use of overlap is a good remedy to the problems. Let n denote the diameter of a coarse well-block in a uniform, square, coarse grid partition. For cases with relatively smooth near-well permeability, overlap n gives a robust method for all well placements. However, the tests have shown that highly heterogeneous permeability fields with channel structures can result in large errors even with overlap n or center well placement. In order to reduce this error, improvements in the current version of MsMFEM must be considered.

9.2.2 Further work

Future studies of overlap should include extensions and tests for non-square and non-uniform coarse grid partitions. Moreover, a study should address optimization aspects, such as time and memory consumption of using overlap relative to the gain. In addition, the effect of center well placement should be studied further. One possible setup is to adapt existing non-uniform coarse grid partitions to obtain center wells, and compare results for the adapted grid and the original grid to a reference solution. Moreover, use of overlap could also be included in the setup. If such a study confirms the results obtained here, the guidelines for coarse grid generation [4] could be updated to include center well placement and overlap.

The tests of MsMFEM with overlap have revealed weaknesses in the current version of MsMFEM on highly heterogeneous permeability layers with channel structures. These weaknesses have also previously been reported in e.g. [3]. Possible approaches for reducing these errors are the use of global boundary conditions [1] and the use of overlap in the computation of all the basis functions. Both of these approaches require increased computational effort. Future studies could include a comparison of the two methods where accuracy, simulation time, and memory use are considered.

Appendix A

Notation

- The symbol $\mathbb{R}$ is used to denote the real numbers.
- If a is a discrete set, then $\#a$ denotes the number of elements in a.
- A spatial vector, e.g. $\vec{x} \in \mathbb{R}^2$, is marked with an arrow.
- Tensors and matrices are denoted by uppercase letters, while vectors are denoted by lowercase letters with exception of the flux $\mathbf{F}$.
- Tensors, matrices, and discrete vectors, such as in the linear system $\mathbf{A}\mathbf{u} = \mathbf{b}$, are marked with bold font lock.
- We write $\mathbf{A} = [a_{ij}]$ to mean that the $(i, j)^{\text{th}}$ entry of $\mathbf{A}$ is a_{ij}.
- $\operatorname{tr} \mathbf{A}$ = trace of the matrix $\mathbf{A}$.
- $\ker \mathbf{A}$ = the kernel, or null-space, of the matrix $\mathbf{A}$.
- The matrix $\mathbf{I}$ denotes the identity matrix of appropriate size.

Appendix B

Eigenvalues of the QR-inner product

In the following we show that the eigenvalues of the QR-inner product matrix $\mathbf{T}_E$ is $\{2, 3\alpha\}$. Consider a unit cell ($|E| = 1$) as displayed in Figure B.1. Using the same notation as in Section 5.4, the QR-inner product is given by

$$\mathbf{T}_E = \frac{1}{|E|}\mathbf{N}\mathbf{N}^T + 3\alpha(\mathbf{I} - \mathbf{Q}\mathbf{Q}^T). \tag{B.1}$$

Since $\mathbf{T}_E$ is a symmetric positive definite matrix it has an eigenvalue decomposition. Given the grid cell in Figure B.1, the normal vector matrix $\mathbf{N}$ and the matrix $\mathbf{R}$ is given by

$$\mathbf{N} = \begin{pmatrix} -1 & 0 \\ 1 & 0 \\ 0 & -1 \\ 0 & 1 \end{pmatrix}, \quad \mathbf{R} = \frac{1}{2}\mathbf{N}. \tag{B.2}$$

Further, $\mathbf{Q} = \frac{1}{\sqrt{2}}\mathbf{N}$ is an orthogonal basis for $\mathbf{R}$, and $\mathbf{Z}$ given by

$$\mathbf{Z} = \frac{1}{\sqrt{2}} \begin{pmatrix} 1 & 0 \\ 1 & 0 \\ 0 & 1 \\ 0 & 1 \end{pmatrix}, \tag{B.3}$$

is an orthogonal basis for $\ker(\mathbf{R}^T)$. We have

$$\mathbf{I} - \mathbf{Q}\mathbf{Q}^T = \mathbf{Z}\mathbf{Z}^T. \tag{B.4}$$

The eigenvalue decomposition of $\mathbf{T}_E$ is given by

$$\mathbf{T}_E = \mathbf{N}\mathbf{N}^T + 3\alpha\mathbf{Z}\mathbf{Z}^T = 2\mathbf{Q}\mathbf{Q}^T + 3\alpha\mathbf{Z}\mathbf{Z}^T = \begin{pmatrix} \mathbf{Q} & \mathbf{Z} \end{pmatrix} \begin{pmatrix} 2 & 0 & 0 & 0 \\ 0 & 2 & 0 & 0 \\ 0 & 0 & 3\alpha & 0 \\ 0 & 0 & 0 & 3\alpha \end{pmatrix} \begin{pmatrix} \mathbf{Q}^T \\ \mathbf{Z}^T \end{pmatrix}. \tag{B.5}$$

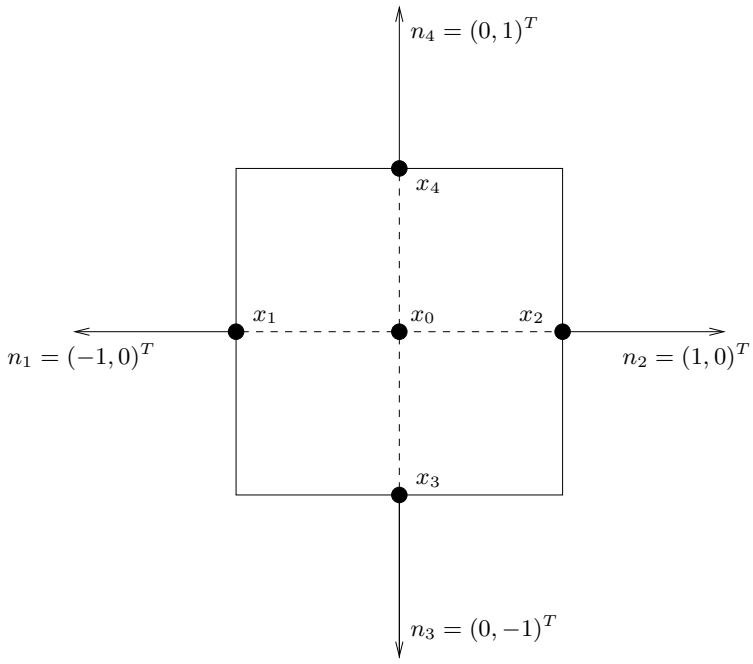

Figure B.1: Square cell.

We conclude that $\mathbf{T}_E$ has the eigenvalues $\{2, 3\alpha\}$.

Bibliography

[1] J. E. Aarnes. On the use of a mixed multiscale finite element method for greater flexibility and increased speed or improved accuracy in reservoir simulation. *Multiscale Model. Simul.*, 2(3):421–439, 2004.

[2] J. E. Aarnes, T. Gimse, and K.-A. Lie. An introduction to the numerics of flow in porous media using Matlab. In G. Hasle, K.-A. Lie, and E. Quak, editors, *Geometrical Modeling, Numerical Simulation and Optimization: Industrial Mathematics at SINTEF*, pages 265–306. Springer-Verlag, 2007. DOI: 10.1007/978-3-540-68783-2_9.

[3] J. E. Aarnes, S. Krogstad, and K.-A. Lie. A hierarchical multiscale method for two-phase flow based upon mixed finite elements and nonuniform coarse grids. *Multiscale Model. Simul.*, 5(2):337–363, 2006.

[4] J. E. Aarnes, S. Krogstad, and K.-A. Lie. Multiscale mixed/mimetic methods on corner-point grids. *Comput. Geosci., Special issue on multiscale methods*, 2008. DOI:10.1007/s10596-007-9072-8.

[5] I. Aavatsmark. Bevarelsesmetoder for elliptiske differensialligninger. Lecture notes, University of Bergen, 2005.

[6] I. Aavatsmark and R. A. Klausen. Well index in reservoir simulation for slanted and slightly curved wells in 3D grids. *SPE J*, 8(1):41–48, 2003.

[7] K. Aziz and A. Settari. *Petroleum reservoir simulation*. Applied Science Publishers, New York, 1979.

[8] F. Brezzi and M. Fortin. *Mixed and hybrid finite element methods*, volume 15 of *Springer Series in Computational Mathematics*. Springer-Verlag, New York, 1991.

[9] F. Brezzi, K. Lipnikov, and M. Shashkov. Convergence of the mimetic finite difference method for diffusion problems on polyhedral meshes. *SIAM J. Numer. Anal.*, 43(5):1872–1896 (electronic), 2005.

[10] F. Brezzi, K. Lipnikov, and V. Simoncini. A family of mimetic finite difference methods on polygonal and polyhedral meshes. *Math. Models Methods Appl. Sci.*, 15(10):1533–1551, 2005.

[11] Z. Chen and T. Y. Hou. A mixed multiscale finite element method for elliptic problems with oscillating coefficients. *Math. Comput.*, 72:541–576, 2003.

[12] Z. Chen, G. Huan, and Y. Ma. *Computational Methods for Multiphase Flows in Porous Media*. SIAM, 2006.

[13] M. A. Christie. Upscaling for reservoir simulation. *J. Pet. Tech*, 48:1004–1010, 1996.

[14] M. A. Christie and M. J. Blunt. Tenth SPE comparative solution project: A comparison of upscaling techniques. *SPE Reserv. Eval. Eng*, 4(4):308–317, 2001.

[15] S. R. de Groot and P. Mazur. *Non-equilibrium thermodynamics*. Dover, 1984.

[16] L. C. Evans. *Partial differential equations*, volume 19 of *Graduate Studies in Mathematics*. AMS, Providence, RI, 1998.

[17] R. E. Ewing, R. D. Lazarov, S. L. Lyons, D. V. Papavassiliou, J. Pasciak, and G. Qin. Numerical well model for non-darcy flow through isotropic porous media. *Comput. Geosci.*, 3:185–204, 1999.

[18] M. Golan and C. H. Whitson. *Well Performance*. Prentice-Hall, Inc, New Jersey, 1991.

[19] T. Hou and X. H. Wu. A multiscale finite element method for elliptic problems in composite materials and porous media. *J. Comput. Phys.*, 134(1):169–189, 1997.

[20] V. Kippe, J. E. Aarnes, and K.-A. Lie. A comparison of multiscale methods for elliptic problems in porous media flow. *Comput. Geosci.*, 2008. DOI:10.1007/s10596-007-9074-6.

[21] R. A. Klausen. *On locally conservative numerical methods for elliptic problems; application to reservoir simulation*. PhD thesis, University of Oslo, 2003.

[22] S. Krogstad and L. J. Durlofsky. Multiscale mixed finite element modeling of coupled wellbore/near-well flow. In *SPE Reservoir Simulation Symposium*, 2007.

[23] M. Muskat. *The flow of homogeneous fluid through porous media*. McGraw Hill Book Co., Inc, New York, 1937.

[24] D. W. Peaceman. Interpretation of well-block pressures in numerical reservoir simulation. *SPE, Trans. AIME*, 253:183–194, 1978.

[25] D. W. Peaceman. Interpretation of well-block pressures in numerical reservoir simulation with nonsquare grid blocks and anisotropic permeability. *SPE, Trans. AIME*, 275:10–22, 1983.

[26] D. K. Ponting. Corner point geometry in reservoir simulation. In *The Mathematics of Oil Recovery*, pages 45–65. Claredon, 1992.

[27] P.-A. Raviart and J. M. Thomas. A mixed finite element method for 2nd order elliptic problems. In *Mathematical aspects of finite element methods (Proc. Conf., Consiglio Naz. delle Ricerche (C.N.R.), Rome, 1975)*, pages 292–315. Lecture Notes in Math., Vol. 606. Springer-Verlag, Berlin, 1977.

[28] Schlumberger. Eclipse: Schedule user guide 2004a, 2004.

[29] J. Shu. Comparison of various techniques for computing well index. Master's thesis, Stanford University, 2005.

[30] C. Wolfsteiner, K. Aziz, and L. J. Durlofsky. Modeling conventional and non-conventional wells. *Sixth International Forum on Reservoir Simulation, Hof/Salzburg, Austria, Sept*, pages 3–7, 2001.

[31] C. Wolfsteiner, L. J. Durlofsky, and K. Aziz. Calculation of well index for nonconventional wells on arbitrary grids. *Comput. Geosci.*, 7(1):61–82, 2003.